

Université du Québec  
Institut national de la recherche scientifique  
Centre Énergie Matériaux Télécommunications

**MODULATION SPECTRUM ANALYSIS FOR NOISY  
ELECTROCARDIOGRAM SIGNAL PROCESSING AND APPLICATIONS**

By

Diana Patricia Tobón Vallejo

A thesis submitted in fulfillment of the requirements for the degree of  
*Doctor of Philosophy, Ph.D.*  
in Telecommunications

**Evaluation committee**

Internal evaluator and committee president:	Prof. José Azaña INRS-ÉMT
External evaluator:	Prof. Harinath Garudadri University of California
External evaluator:	Prof. Sri Krishnan Ryerson University
Research advisor:	Prof. Tiago H. Falk INRS-ÉMT
Research co-supervisor:	Prof. Martin Maier INRS-ÉMT



# Acknowledgements

I want to express my gratitude to my supervisor, Dr. Tiago H. Falk, who always gave me an excellent guidance on my research project with brilliant ideas, and great advice in my learning process. Without his excellent supervision, this project would not have been possible. I also want to thank to my co-supervisor, Dr. Martin Maier, for his contribution in my PhD studies as well as for his valuable advice in my formation.

I would like to extend my gratitude to the members of the evaluation committee, Prof. José Azaña, Prof. Harinath Garudadri, and Prof. Sri Krishnan to be part of my thesis examination and for their helpful observations.

I also feel grateful to be part of the Multimedia/Multimodal Signal Analysis and Enhancement (MuSAE) and Optical Zeitgeist Laboratories, which have excellent people as well as many resources that allow innovative research development. I also acknowledge the financial support from Natural Sciences and Engineering Research Council of Canada (NSERC).

The last great thanks is for my lovely mother, who has been the motor of my life and has always believed in me. I dedicate this thesis to you.



# Abstract

Advances in wearable electrocardiogram (ECG) monitoring devices have allowed for new cardiovascular applications to emerge beyond diagnostics, such as stress and fatigue detection, athletic performance assessment, sleep disorder characterization, mood recognition, activity surveillance, biometrics, and fitness tracking, to name a few. Such devices, however, are prone to artifacts, particularly due to movement, thus hampering heart rate and heart rate variability measurement and posing a serious threat to cardiac monitoring applications. To address these issues, this thesis proposes the use of a spectro-temporal signal representation called “modulation spectrum”, which is shown to accurately separate cardiac and noise components from the ECG signals, thus opening doors for noise-robust ECG signal processing tools and applications.

First, an innovative ECG quality index based on the modulation spectral signal representation is proposed. The representation quantifies the rate-of-change of ECG spectral components, which are shown to be different from the rate-of-change of typical ECG noise sources. As such, a signal-to-noise ratio (SNR) like metric is proposed, termed modulation spectral based quality index (MS-QI). Unlike existing quality metrics, MS-QI does not rely on machine learning algorithms, can be performed on single-lead ECGs, and was shown to perform accurately with synthetic ECGs, as well as ECGs recorded in real-world environments.

Based on insights obtained from the MS-QI metric, a new adaptive ECG enhancement algorithm is then proposed based on the principle of bandpass filtering in the modulation spectral domain. The algorithm was tested on synthetic and recorded (extremely noisy) ECG databases. Experimental results show the proposed algorithm outperforming a state-of-the-art wavelet-based enhancement algorithm in terms of heart rate (HR) error percentage measurement, signal-to-noise ratio (SNR) improvement, and ECG kurtosis; the latter is a widely-used ECG quality metric. These findings suggest that the proposed algorithm can be used to enhance the quality of wearable ECG monitors even in extreme conditions, thus it can play a key role in athletic peak performance training/monitoring.

Moreover, wearable ECG monitoring applications are burgeoning and typically rely on estimates of heart rate variability (HRV). Such applications require small computational footprint and cannot rely on enhancement and HRV analysis, thus a stand-alone HRV metric is needed. HRV indices have been proposed based on time- and frequency-domain analyses of the ECG, as well as via non-linear approaches. These methods, however, are very sensitive to ECG artefacts, thus limiting the number of applications involving noisy ECGs (e.g., ath-

letic peak performance training). Typically, ECG enhancement is performed prior to HRV computation to overcome this limitation. Existing enhancement algorithms, however, are not accurate in very noisy scenarios. Hence, an alternate approach is proposed based on the modulation spectrum. By quantifying the rate-of-change of ECG spectral components over time, we show that heart rate estimates can be reliably obtained even in extremely noisy signals, thus bypassing the need for ECG enhancement. The so-called MD-HRV (modulation domain HRV) is tested on synthetic and recorded noisy ECG signals and shown to outperform several benchmark HRV metrics computed post-enhancement. These findings suggest that the proposed MD-HRV metric is well-suited for ambulant cardiac monitoring applications, particularly those involving intense movement.

Finally, a quality-aware ECG monitoring application is presented based on the proposed MS-QI. Wearable ECG devices are increasingly being used in telehealth applications, particularly for patient monitoring applications. Representative devices include watches, chest straps, and even smart clothing via textile ECG sensors. Such lower-cost sensors, however, are extremely sensitive to movement, thus pose a serious threat to such ECG streaming applications. For example, transmission bandwidth, battery life, and/or storage space can be spent with ECG segments that convey little cardiac information due to the high levels of noise present. Moreover, noisy signals may cause false alarms in automated patient monitoring systems, thus increasing the burden on medical personnel. Here, by employing the MS-QI to discriminate usable from non-usable ECG segments, a quality-aware storage protocol was implemented where storage of cardiac parameters was only performed on the usable segments. When tested with a smart shirt under three conditions, namely sitting, walking and running, the proposed quality-aware application resulted in storage savings of 65%.

**Keywords** Denoising, Electrocardiogram, Heart Rate, Heart Rate Variability, Modulation Spectrum, Quality Index, Telehealth, Wearables.

# Statement of Originality

I hereby certify that this thesis contains original work of the author. Some techniques employed from other authors are properly referenced herein.

Diana P. Tobón

Montréal, QC, December, 2016



# Contents

<b>Acknowledgements</b>	<b>iii</b>
<b>Abstract</b>	<b>v</b>
<b>Contents</b>	<b>ix</b>
<b>List of Figures</b>	<b>xiii</b>
<b>List of Tables</b>	<b>xv</b>
<b>List of Acronyms</b>	<b>xvii</b>
<b>Sommaire récapitulatif</b>	<b>xxi</b>
0.1 Introduction . . . . .	xxi
0.2 Le signal d'électrocardiogramme . . . . .	xxiii
0.2.1 Forme des vagues de l'ECG . . . . .	xxiv
0.3 Analyse spectrale de modulation d'ECG proposée . . . . .	xxiv
0.4 Index de qualité de base pour la gamme de modulation . . . . .	xxvi
0.4.1 Ensemble de données 1: Données synthétiques d'ECG . . . . .	xxvii
0.4.2 Ensemble de données 2: Données d'ECG enregistrées pour le vêtement Hexoskin . . . . .	xxvii
0.4.3 Ensemble de données 3: Base de données Physionet du défi de qualité de signal . . . . .	xxviii
0.4.4 Ensemble de données 4: Données d'ECG ambulatoires enregistrées . .	xxviii
0.4.5 Mesures de qualité de la référence . . . . .	xxix
0.4.6 Bilan de performance . . . . .	xxix
0.4.7 Résultats . . . . .	xxx
0.4.8 Discussion . . . . .	xxxii
0.5 Filtre spectro-temporel pour la détection de pic . . . . .	xxxii
0.5.1 Base de données 1: ECG synthétique . . . . .	xxxiv
0.5.2 Base de données 2: Défi de données de Physionet 2014 . . . . .	xxxiv
0.5.3 Algorithme de référence et bilan de performances des indicateurs . . .	xxxiv
0.5.4 Résultats expérimentaux et discussion . . . . .	xxxv
0.6 Modulation de la mesure du domaine de variabilité de fréquence cardiaque .	xxxvii
0.6.1 Base de données 1: ECG synthétique . . . . .	xxxviii
0.6.2 Base de données 2: Base de données Arythmie MIT-BIH . . . . .	xxxviii
0.6.3 Référence et figures de mérite . . . . .	xxxviii

0.6.4	Résultats . . . . .	xxxix
0.6.5	Discussion . . . . .	xl
0.7	Vers des applications de télésanté sensibles à la qualité . . . . .	xli
0.7.1	Stratégies de classification . . . . .	xlii
0.7.2	Traits caractéristiques de référence et fusion de traits caractéristiques . . . . .	xlii
0.7.3	Ensemble de données d’entraînement: ECG synthétique . . . . .	xliii
0.7.4	Ensembles de données de test 1 et 2 . . . . .	xliii
0.7.5	Évaluation de la performance . . . . .	xliii
0.7.6	Résultats et discussion . . . . .	xliii
0.8	Conclusions . . . . .	xliv
<b>1</b>	<b>Introduction</b>	<b>1</b>
1.1	Challenges with Noisy ECG Signals . . . . .	5
1.2	Thesis Contributions . . . . .	7
1.3	Publications and Patents . . . . .	9
1.4	Thesis Organization . . . . .	10
<b>2</b>	<b>Electrocardiogram Signal Processing</b>	<b>11</b>
2.1	The Electrocardiogram Signal . . . . .	11
2.1.1	ECG Waveform . . . . .	13
2.1.2	Recorded ECG Signal . . . . .	13
2.1.3	Synthesized ECG Signal . . . . .	16
2.2	Conventional ECG Signal Analysis Methods . . . . .	19
2.2.1	Heart Rate Variability . . . . .	19
2.2.2	QRS Detection Algorithm . . . . .	23
2.2.3	Heart Rate Variability Analysis Software (HRVAS) . . . . .	24
2.3	ECG Signal Enhancement . . . . .	26
2.4	Benchmark ECG Quality Metrics . . . . .	33
2.5	Proposed ECG Modulation Spectral Analysis . . . . .	34
<b>3</b>	<b>MS-QI: A Modulation Spectrum-Based ECG Quality Index for Telehealth Applications</b>	<b>39</b>
3.1	Preamble . . . . .	39
3.2	Introduction . . . . .	40
3.3	Modulation Spectrum Based Quality Index . . . . .	40
3.3.1	Dataset 1: Synthetic ECG Data . . . . .	42
3.3.2	Dataset 2: Recorded Hexoskin Garment ECG Data . . . . .	43
3.3.3	Dataset 3: Physionet Challenge Signal Quality Database . . . . .	44
3.3.4	Dataset 4: Recorded Ambulatory ECG Data . . . . .	45
3.3.5	Benchmark Quality Measures . . . . .	46
3.3.6	Performance Assessment . . . . .	46
3.4	Results . . . . .	47
3.5	Discussion . . . . .	51
3.6	Conclusion . . . . .	53
<b>4</b>	<b>Adaptive Spectro-Temporal Filtering for Electrocardiogram Signal Enhancement</b>	<b>55</b>

4.1	Preamble . . . . .	55
4.2	Introduction . . . . .	56
4.3	Modulation Domain Filtering for Improved Peak Detection . . . . .	56
4.3.1	Database 1: Synthetic ECG . . . . .	60
4.3.2	Database 2: Physionet 2014 Challenge Data . . . . .	60
4.3.3	Benchmark Algorithm and Performance Assessment Metrics . . . . .	61
4.4	Experimental Results and Discussion . . . . .	63
4.5	Conclusion . . . . .	67
<b>5</b>	<b>Spectro-Temporal ECG Analysis for Noise-Robust HRV Measurement</b>	<b>69</b>
5.1	Preamble . . . . .	69
5.2	Introduction . . . . .	69
5.3	Modulation Domain HRV Measurement . . . . .	71
5.3.1	Dataset 1: Synthetic ECG . . . . .	72
5.3.2	Dataset 2: MIT-BIH Arrhythmia Dataset . . . . .	72
5.3.3	Benchmarks and Figures-of-Merit . . . . .	73
5.4	Results . . . . .	74
5.5	Discussion . . . . .	77
5.6	Conclusion . . . . .	82
<b>6</b>	<b>Towards Quality-Aware Telehealth Applications</b>	<b>83</b>
6.1	Preamble . . . . .	83
6.2	Introduction . . . . .	83
6.3	Classification Strategies . . . . .	85
6.3.1	Benchmark Features and Feature Fusion . . . . .	85
6.3.2	Training Dataset: Synthetic ECG . . . . .	86
6.3.3	Test Dataset 1: Physionet Challenge Signal Quality Database . . . . .	86
6.3.4	Test Dataset 2: Recorded Ambulatory ECG Data . . . . .	87
6.3.5	Test Dataset 3: Textile ECG Data from Hexoskin Garment . . . . .	87
6.3.6	Performance Assessment . . . . .	88
6.4	Results and Discussion . . . . .	89
6.5	Conclusion . . . . .	93
<b>7</b>	<b>Conclusions and Future Research Directions</b>	<b>95</b>
7.1	Conclusions . . . . .	95
7.2	Future Research Directions . . . . .	98
	<b>Bibliography</b>	<b>101</b>



# List of Figures

2.1	Electrical conduction system of the heart. Two main pumps are illustrated with their atria and ventricles. SA corresponds to sinus node and AV to atrio-ventricular node. . . . .	12
2.2	Normal ECG waveform that shows one cardiac cycle or heartbeat and the polarization and repolarization waves. . . . .	14
2.3	Ten-electrode location for the 12-lead standard ECG configuration. . . . .	14
2.4	Tridimensional trajectory generated by the dynamic model proposed in [67]. The dashed lines represent the unit circle and the small blue points the positions of P, Q, R, S, and T events. . . . .	17
2.5	Ten-second excerpts from the noisy synthetic ECG signals. . . . .	19
2.6	Block diagram of the Pan-Tompkins algorithm steps to detect QRS complexes [88]. . . . .	24
2.7	Flowchart of the HRV analysis employed in the HRVAS software [30]. LSP: Lomb-Scargle periodogram, Welch: Welch periodogram, Burg: Burg periodogram, and CWT: continuous wavelet transform. . . . .	26
2.8	Processing steps to calculate the modulation spectral signal representation. Base transform (e.g., short-time Fourier transform) is applied to the sampled ECG signal $x(n)$ to obtain a time-frequency representation. Spectral magnitudes $ X(f, m) $ are windowed across time and a second transform (modulation transform) is applied to obtain the frequency-frequency modulation frequency representation $\mathcal{X}(f, f_{m,k})$ . . . . .	36
2.9	Modulation spectrograms of synthesized clean ECGs with (a) 60 and (b) 150 bpm, (c) noisy ECG with an $SNR = 5$ dB (150 bpm), and (d) noise signal with recorded muscle contraction and electrode movement. . . . .	38
3.1	Hexoskin garment used to collect ECG data during three different activity levels: sitting, walking and running. . . . .	43
3.2	Plots of (a) actimetry profile for ECG recording with the Hexoskin garment, (b) 10-second excerpts of the collected signals during (top to bottom) sitting, walking, and running, and (c) modulation spectrograms for the collected signals. . . . .	44
3.3	Scatterplots and errorbars of (a) MS-QI, (b) $\kappa$ , and (c) IOR as a function of SNR for Dataset 1. . . . .	48
3.4	Scatterplots of (a) MS-QI, (b) $\kappa$ , and (c) IOR as a function of activity level (actimetry) for Dataset 2. . . . .	49
3.5	Kernel fit of MS-QI probability distributions for good (black) and bad (gray) quality ECG for Datasets 1 (solid), 3 (dash), and 4 (dash-dot). . . . .	50

3.6	Kernel fit of $\kappa$ probability distributions for good (black) and bad (gray) quality ECG for (a) Dataset 1, (b) Datasets 3 (dash) and 4 (dash-dot). . . . .	50
3.7	Scatterplot of $\kappa$ as a function of log(actimetry) for Dataset 2. . . . .	52
4.1	Block diagram of the general signal processing steps involved in the proposed modulation filtering scheme. . . . .	58
4.2	Plots of (a) time domain ECG signals with 60 bpm for a noisy ECG signal with SNR of -5 dB, and modulation filtering and wavelet enhanced signals, (b) modulation spectrograms for the noisy and enhanced signals. . . . .	60
4.3	(a) Inter-beat interval (ibi) and (b) pNN50 error percentage for noisy, proposed, and benchmark-enhanced algorithms for Database 1. . . . .	63
4.4	Kernel fit of probability distributions of HR error percentage for noisy (dash), proposed (line), and benchmark (dash-dot) algorithms for Database 2. . . . .	64
5.1	Modulation spectrogram of synthesized ECG with 120 bpm and at SNR = -10 dB. The color bar shows the range values in dB. . . . .	72
5.2	Scatterplots for noisy ECG signals with 100 bpm and SNR = -10 dB between (a) ‘true’ sdHR and noisy sdHR, (b) ‘true’ sdHR and wavelet enhanced sdHR, and (c) ‘true’ sdHR and proposed MD-HRV. . . . .	77
5.3	Bland-Altman plots for noisy ECG signals with 100 bpm and SNR = -10 dB between (a) ‘true’ sdHR and noisy sdHR, (b) ‘true’ sdHR and wavelet enhanced sdHR, and (c) ‘true’ sdHR and proposed MD-HRV. . . . .	78
5.4	Scatterplots for Group 2 in Dataset 2 for (a) Noisy sdHR and ‘true’ sdHR, (b) Wavelet enhanced sdHR and ‘true’ sdHR, and (c) Proposed MD-HRV and ‘true’ sdHR. . . . .	79
5.5	Bland-Altman plots for Group 2 in Dataset 2 for (a) Noisy sdHR and ‘true’ sdHR, (b) Wavelet enhanced sdHR and ‘true’ sdHR, and (c) Proposed MD-HRV and ‘true’ sdHR. . . . .	80
6.1	Actimetry profile for one participant of test Dataset 3. LDA classifier decisions are labelled 1 for usable and 0 for unusable using the (a) MS-QI and (b) $\kappa$ features. . . . .	90
6.2	Ten-second excerpt from the ECG signal during running. . . . .	91
6.3	Actimetry profile for one participant of test Dataset 3. Manual thresholding decisions are labelled ‘Good’ for usable and ‘Bad’ for unusable using the (a) MS-QI and (b) $\kappa$ features. . . . .	92
7.1	Modulation spectrograms for (a) a healthy person and (b) a patient with neuropathy. . . . .	100

# List of Tables

2.1	ECG model parameters for the ECG dynamic model. . . . .	16
3.1	Performance comparison between proposed MS-QI measure and the two benchmark metrics for Datasets 1 and 2. . . . .	48
4.1	Percentage HR estimation error for wavelet benchmark algorithm for different thresholding selection rules. . . . .	62
4.2	Performance comparison (HR error, post-SNR, and $\kappa$ ) before and after enhancement with proposed and benchmark algorithms for Database 1. . . . .	63
5.1	Performance comparison ( $\rho$ and $\rho_S$ ) of HRV metrics for noisy signals, wavelet enhanced signals, and the proposed MD-HRV metric for Dataset 1 at different SNR level. . . . .	75
5.2	Performance comparison ( $\rho$ and $\rho_S$ ) of HRV metrics for noisy signals, wavelet enhanced signals, and the proposed MD-HRV metric for Dataset 2. . . . .	76
6.1	Performance comparison of LDA and SVM classifiers trained on MS-QI and $\kappa$ features, as well as a fusion of both feature sets. Results for the synthetic ECG dataset correspond to training the classifiers with 50% of the data and testing with the remaining 50%. The MT classification strategy was tested in all the datasets as well. Results correspond to accuracy/sensitivity/specificity. . . . .	90



# List of Acronyms

<b>ABI</b>	Allied Business Intelligence
<b>ACC</b>	Accuracy
<b>AV</b>	Atrioventricular
<b>BPM</b>	Beats Per Minute
<b>DFT</b>	Discrete Fourier Transform
<b>DWPT</b>	Discrete Wavelet Packet Transform
<b>DWT</b>	Discrete Wavelet Transform
<b>ECG</b>	Electrocardiogram
<b>EEMD</b>	Ensemble Empirical Mode Decomposition
<b>EMD</b>	Empirical Mode Decomposition
<b>EME</b>	Electrocardiogram Modulation Energy
<b>EMG</b>	Electromyography
<b>FAST</b>	Future Attribute Screening Technology
<b>FFT</b>	Fast Fourier Transform
<b>FIR</b>	Finite Impulse Response
<b>FN</b>	False Negatives
<b>FP</b>	False Positives
<b>GUI</b>	Graphical User Interface
<b>HF</b>	High Frequency
<b>HR</b>	Heart Rate
<b>HRV</b>	Heart Rate Variability
<b>HRVAS</b>	Heart Rate Variability Analysis Software
<b>HWR</b>	Half-Wave Rectification

<b>IBI</b>	Inter-Beat Interval
<b>ICU</b>	Intensive Care Units
<b>IIR</b>	Infinite Impulse Response
<b>IMF</b>	Intrinsic Mode Function
<b>IOR</b>	In-Band to Out-of-Band Spectral Power Ratio
<b>MABWT</b>	Multi-Adaptive Bionic Wavelet Transform
<b>MSE</b>	Mean Square Error
<b>MS-QI</b>	Modulation Spectral Based Quality Index
<b>MT</b>	Manual Thresholding
<b>NN</b>	Normal-to-Normal
<b>LA</b>	Left Arm
<b>LDA</b>	Linear Discriminant Analysis
<b>LF</b>	Low Frequency
<b>LF/HF</b>	Low Frequency to High Frequency ratio
<b>LL</b>	Left leg
<b>PRD</b>	Percent Root Mean Square Difference
<b>PSD</b>	Power Spectral Density
<b>QS</b>	Quantified Self
<b>RA</b>	Right Arm
<b>RME</b>	Remaining Modulation Energy
<b>RMS</b>	Root Mean Square
<b>RSA</b>	Respiratory Sinus Arrhythmia
<b>SA</b>	Sinoatrial
<b>SE</b>	Sensitivity
<b>SNR</b>	Signal-to-Noise Ratio
<b>SP</b>	Specificity
<b>SVM</b>	Support Vector Machine
<b>SWT</b>	Stationary Wavelet Transform
<b>TN</b>	True Negatives

<b>TP</b>	True Positives
<b>ULF</b>	Ultra Low Frequency
<b>VLF</b>	Very Low Frequency



# Sommaire récapitulatif

## 0.1 Introduction

Des statistiques récentes ont déterminé les maladies cardiaques comme étant la première cause de décès aux États-Unis, représentant un quart des décès [1]. Au niveau mondial, les statistiques sont similaires et 30% des décès sont relatifs aux maladies cardiovasculaires [2]. Selon la fondation Heart and Stroke, l'électrocardiogramme (ECG) est un outil disponible et performant, capable d'aider les cliniciens à détecter, diagnostiquer et contrôler certaines maladies cardiaques. Les applications représentatives peuvent inclure: la détection des rythmes cardiaques anormaux (arythmie), les attaques cardiaques en cours, le blocage de l'artère coronarienne, les zones musculaires du cœur endommagées depuis une attaque cardiaque, le grossissement du cœur, l'inflammation du sac entourant le cœur (péricardite), les dérèglements d'électrolytes, les maladies pulmonaires, ainsi que le contrôle de l'efficacité de certains traitements du cœur ou du simulateur cardiaque (ou pacemaker), ou même exclure toute maladie du cœur cachée chez les patients qui vont se faire opérer [3]. Les applications de monitoring sont en pleine essor, là où l'ECG est le signal mesuré le plus utilisé pour détecter non seulement les maladies cardiovasculaires, mais aussi les activités, les niveaux de stress [4], les émotions et l'endurance de l'athlète [5]. Les prévisions des marchés récents ont annoncé que celui du contrôle de l'ECG et de la gestion du rythme cardiaque croîtrait d'environ 27 milliards de dollars pour 2020 [6], dû par exemple à la hausse du nombre des cas de maladies cardiovasculaires [7], les nouvelles applications de gestion de santé [8] et de gestion des maladies [9].

En ce moment, il y a un fort intérêt dans les applications de quantification. Les gens sont encore plus intéressés dans l'amélioration de leur qualité de vie en s'équipant de capteurs (ex. capteurs portables) qui peuvent donner des informations sur leurs états de santé. Ainsi, avec l'émergence de ces applications, les contrôleurs ECG sans-fil se sont répandus, non seulement dans le domaine clinique (ex. [10]), mais aussi dans le monde commercial du sport et du consommateur (ex. [5, 11, 12]). Cette croissance témoignée des applications de "quantification indépendante" a été majoritairement dirigée par des avancées récentes en innovation, telles que les contrôleurs d'ECG sans-fil abordables (ex. [13]), des t-shirts et soutien-gorge intelligents (ex. OMSignal), des réseaux de capteurs de mesure pour le corps

humain (Wireless Body Area Network - WBAN) et les montres intelligentes. Certains appareils ont pénétré le marché, tels que le vêtement Hexoskin (Carre Technologies, Canada), nECG (Nuubo, Espagne), BioHarness (Zephyr, États-Unis), Fitbit (États-Unis), le brassard UP de Jawbone (États-Unis), la ceinture cardio Biofusion de Biopeak (Canada) et Corbelt (Corscience, Allemagne).

Cependant, l'utilisation des capteurs portables pour les applications de télémédecine a augmenté très fortement ces dernières années. Des experts ont considéré l'année 2014 comme "l'année des portables", due à l'industrie florissante des appareils de santé portatifs étant évaluée à 700 millions de dollars cette année [6]. En outre, d'après "Statista", le marché des appareils portables atteindra 19 milliards de dollars en 2018 [14]. Cependant, depuis que certains appareils ont permis aux applications de télémédecine de se développer, plusieurs défis ont été créés et ayant toujours besoin d'être surmontés, le plus important étant celui de la qualité des signaux d'ECG. Les capteurs portables abordables d'ECG sont extrêmement sensibles à différents types d'artéfacts comme la respiration, le mouvement du corps et les contractions des muscles, ralentissant ainsi le rythme cardiaque (HR), l'analyse de la variation du rythme cardiaque (HRV) [15] et les techniques d'exigences de résistance au bruit.

Cette thèse est divisée en quatre buts à atteindre: (1) Analyser les signaux bruyants d'ECG pour les applications développées de télémédecine en utilisant la représentation de spectre de modulation pour le bilan de qualités, (2) L'amélioration de l'ECG, (3) L'analyse précise de la variation du rythme cardiaque dans des scénarios de bruit extrême, (4) L'incorporation de ces résultats dans une application résistante au bruit. Les idées clés sont:

1. La proposition d'un nouvel index de qualité d'ECG appelé "Index de Qualité du Spectre de Modulation" (MS-QI). A cet effet, la représentation spectrale de la modulation qui permet de séparer les composants du spectre de l'ECG aux artéfacts a été utilisée. L'index est similaire au ratio "rapport signal sur bruit" (RSB) depuis qu'il identifie l'énergie des composants spectraux d'ECG aux composants spectraux du bruit. Les valeurs MS-QI sont normalement entre 0 et 1,5 avec des valeurs plus hautes correspondant à la qualité améliorée. L'index peut être utilisé à la fois en tant qu'indicateur qualité comme détecteur de type d'activité (ex. assis, marche ou course) pas seulement pour les applications de télémédecine mais aussi pour la forme physique/l'entraînement où l'ECG est très contaminé par des artéfacts de mouvement. Les résultats de cet article ont été publiés en #2 et #3 .
2. La proposition d'un nouvel algorithme d'amélioration de l'ECG basé sur le filtrage spectro-temporel. Cet algorithme améliore la détection des pics (ex. détection du rythme cardiaque), l'analyse du HRV, la qualité (ex. kurtosis) et le ratio RSB sur les composants spectraux de l'ECG peuvent être séparés du bruit dans le domaine de spectre de modulation. Dans ce cas, une banque de filtres de modulation de bande passante de phase linéaire "Finite Impulse Response" (FIR) a été utilisée pour extraire les composants

de modulation spectrale. L'utilisation des transformations calculant la représentation spectrale de modulation permettra le bon filtrage dans ce domaine et reconstruira le signal ECG amélioré dans le domaine de temps. Cette méthode est faite pour les appareils d'ECG portables abordables qui peuvent être contaminés par des artefacts en mouvement. Les publications résultant de ces articles incluent #3, #4, et #5.

3. Un nouvel index de variabilité du rythme cardiaque résistant au bruit, nommé "domaine de modulation HRV" (MD-HRV) est présenté. Le rythme cardiaque peut être estimé dans le domaine de modulation en quantifiant le rythme de variation des composants spectraux de l'ECG, d'où le rythme cardiaque peut être extrait même dans des scénarios très bruyants, dépassant ainsi le besoin d'utilisation de l'algorithme d'amélioration d'ECG. Par conséquent, l'index MD-HRV est calculé en tant que déviation standard des fréquences de modulation centrales par image, correspondant au rythme cardiaque. L'index proposé peut être fait pour les applications portables de contrôle cardiaque où le mouvement peut amoindrir la qualité des enregistrements d'ECG. Cette contribution est publiée en #6 et #7.
4. La présentation d'un bilan de qualité en ligne d'ECG utilisant le MS-QI proposé pour la bonne qualité des applications. Les signaux d'ECG utilisables et non-utilisables ont été classés pour obtenir des économies d'espace de stockage pour les applications de télémédecine. De plus, les résultats de classification peuvent être utilisés pour les applications de bonne qualité afin de distinguer différents niveaux (ex. assis, marche et course). Cet article est publié en #8.

## 0.2 Le signal d'électrocardiogramme

Le signal d'ECG est créé par une série de variations électriques dans le cœur d'un être humain. A l'intérieur du muscle cardiaque, aussi appelé myocarde, des décharges électriques se déroulent dans les nœuds étant répartis dans le myocarde. Ainsi, les contractions simultanées sont stimulées pour pomper le sang vers les poumons pour l'oxygénation et renvoyer le sang oxygéné dans tout le corps et aux organes. La figure 2.1 illustre les deux pompes principales dans le cœur. Chaque pompe possède un atrium et un ventricule. Le sang désoxygéné part du corps pour aller dans l'atrium droit qui pompe le sang jusqu'au ventricule droit. Ainsi, ce ventricule envoie le sang désoxygéné aux poumons pour être oxygéné. Le sang, maintenant oxygéné, revient dans le cœur dans l'atrium gauche jusqu'aux veines pulmonaires. Ensuite, l'atrium gauche pompe le sang au ventricule gauche pour le renvoyer dans tout le corps. Tout ce processus est une séquence du cycle cardiaque. Le cycle est composé de deux phases principales appelées diastole et systole. La diastole est la phase de remplissage du sang là où les ventricules se remplissent et se vident pendant que l'atrium se détend. La systole, quant

à elle, correspond aux contractions du cœur dans le but de pomper le sang, soit dans le corps, soit dans les poumons. De ce fait, le cycle possède deux phases appelées dépolarisation (activation) et polarisation (récupération).

Le cycle cardiaque commence grâce à la stimulation électrique (propre excitation) du nœud du sinus (SA). Ce nœud génère spontanément une impulsion électrique qui est envoyée au nœud atrioventriculaire (AV). Le nœud AV connecte l'impulsion électrique de l'atrium aux ventricules (cette conduction dure environ 100 ms). Après ceci, il se passe une période réfractaire d'une durée d'au moins 100 ms puis le cœur revient à son potentiel électrique de base. Par conséquent, le cycle cardiaque est prêt à recommencer [16].

### 0.2.1 Forme des vagues de l'ECG

L'ECG est un signal qui mesure l'activité cardiaque du cœur générée par l'impulsion électrique du nœud SA, se propageant dans le cœur à travers les cellules cardiaques. D'où l'impulsion électrique peut être détectée sur la surface de la peau résultant dans la mesure de l'ECG. Un segment normal d'ECG montre les effets de la repolarisation et de la polarisation dans les différentes parties du cœur.

La figure 2.2 illustre un segment normal d'ECG. Le segment correspond à un des cycles cardiaques du cœur. Le cycle débute par une impulsion électrique générée par le nœud SA se propageant dans l'atrium. Par conséquence, la contraction et la dépolarisation de l'atrium résultent dans la 'vague P'. Le segment 'PQ' ou 'PR' (segment iso-électrique) est le résultat d'un retard de moins de 100 ms après l'instant où l'impulsion électrique atteint le nœud AV. Ce retard laisse le temps à l'atrium de se contracter avant la dépolarisation des ventricules. Ensuite, une contraction générée est représentée dans le 'complexe QRS' lorsque l'impulsion atteint les ventricules (dépolarisation ventriculaire), où la repolarisation de l'atrium est dissimulée. Puis le 'segment ST' apparaît lorsque les ventricules entiers sont dépolarisés, cette dernière pouvant durer jusqu'à 350 ms. Enfin, une vague de repolarisation appelée 'Vague T' apparaît quand les ventricules se détendent.

## 0.3 Analyse spectrale de modulation d'ECG proposée

L'analyse du signal de modulation spectrale consiste en une décomposition de la fréquence des trajectoires temporelles sur des composants spectraux de signaux courts, d'où nous pouvons voir ceci comme une représentation d'un signal fréquence-fréquence. L'analyse spectrale de modulation fut utilisée par le passé pour séparer les sons du cœur et des poumons depuis les enregistrements d'auscultation digitaux [17], tout comme les paroles et bruits ambiants dans un enregistrement au microphone [18]. Cela le rend utile pour des applications de "séparation de source", comme des signaux différents connus pour avoir des composants

modulés à différents taux. Pour les ECG, un outil est proposé pour séparer les composants cardiaques et bruitages depuis un signal bruyant enregistré.

La figure 2.8 illustre les étapes de processus de signal impliqués dans le calcul de la représentation spectrale de modulation d’ECG. Dans les expériences décrites ci-inclus, l’ensemble d’outils de modulation de Matlab pour l’université de Washington a été utilisé [19]. Tout d’abord, le signal d’ECG  $x(n)$  (cadencé ici à 256 Hz) est segmenté en parties chevauchées utilisant une fonction de 32 points avec un chevauchement de 75%, qui sont ensuite transformées selon le domaine de fréquence utilisant une représentation de Fourier de 512 points (FFT), résultant ainsi dans un spectrogramme conventionnel. Les composants de magnitude spectrale  $|X(f, m)|$  (pour un index de bordure  $m$ ) sont également segmentés au-dessus de l’axe du temps en morceaux superposés utilisant des fenêtres de 128 points de “modulation” avec 75% de chevauchement, qui sont traitées plus tard dans une transformation de Fourier de 512 points dans la représentation fréquence-fréquence  $\mathcal{X}(f, f_{m,k})$  appelée “spectrogramme de modulation”, où  $f$  correspond à la fréquence conventionnelle,  $f_m$  à la modulation de fréquence et  $k$  l’index de bordure pour la seconde transformation.

Il est important d’insister sur le fait que ces options pour les tailles de fenêtres de base et de modulation, tout comme les taux de chevauchement, furent optimisés en utilisant les données d’ECG synthétisé et propre et qu’ils imposent une limitation pour la durée minimale d’un test d’ECG de quatre secondes. Lors de nos expériences pilotes, nous avons remarqué que le fait de réduire la fenêtre de modulation de 64 points (réduisant ainsi la limitation de durée de l’ECG à 2 secondes) par exemple, cause une légère baisse dans la performance de la mesure de qualité (environ 2%). De ce fait, la mesure peut être réglée plus finement par la suite pour des applications alternatives nécessitant des réponses rapides, telles que les unités de soins intensifs.

Dans le but de convaincre de l’utilisation du domaine de modulation pour l’analyse d’ECG résistant au bruit, les figures 2.9 (a) et (b) décrivent les spectrogrammes de modulation moyenne par bordure montrés en figure 2.8 (côté droit) des signaux propres synthétiques d’ECG avec 60 et 150 battements par minute (bpm), respectivement (en moyenne un peu plus de 2 minutes de données d’ECG enregistrées). Comme il peut être vu dans les deux sous-figures, la majorité de l’énergie du signal est en dessous d’une fréquence de  $f < 40$  Hz. Pour le premier scénario par exemple, pour 60 bpm, nous pouvons voir que les composants spectraux de l’ECG changent avec un taux de  $f_m = 1$  Hz, tout comme plusieurs autres harmoniques. Dans le cas de 150 bpm, les composants spectraux changent avec un taux de  $f_m = 2.5$  Hz, tout comme ses harmoniques. La figure 2.9 (c), quant à elle, montre un signal d’ECG synthétique bruyant (avec un  $RSB = 5$  dB et de 150 bpm) qui a été corrompu par plusieurs composants de bruit pris depuis la base de données de test stress de bruit MIT-BIH [20]. Comme nous pouvons le voir, les composants de fréquence autour de  $f_m = 0$  Hz (ex. composants stationnaires) sont d’une plus grande bande passante ( $f > 40$  Hz) que leurs homologues

nets, les “lobes” de fréquence de modulation sont d’une énergie diminuée et les énergies de fréquence de modulation entre les lobes sont amplifiées. Néanmoins, malgré le faible RSB, les composants d’ECG peuvent toujours être clairement identifiables dans le spectrogramme de modulation avec des lobes nets toujours détectables jusqu’à  $f_m = 8$  Hz, contrairement aux 10 – 12 Hz dans le scénario propre. Ces découvertes nous ont motivé pour développer un index de qualité d’ECG, un algorithme d’optimisation pour la détection de pic amélioré et un index HRV qui sera présenté au cours dans les sections suivants.

## 0.4 Index de qualité de base pour la gamme de modulation

Dans les figures 2.9 (a) – (c), nous pouvons voir que l’ECG et les composants du bruit se comportent différemment dans le pseudo-domaine du spectre de modulation. Les composants d’ECG apparaissent dans les “lobes de fréquence de modulation” centrés dans les modulations de fréquence relatives au rythme cardiaque et ses harmoniques et sont limités entre  $0 \leq f \leq 40$  Hz. D’autre part, les composants du bruit ne suivent pas les modèles et peuvent affecter plusieurs fréquences de modulation, particulièrement pour  $f_m = 0$  Hz due aux propriétés stationnaires des sources de bruits. En utilisant ces idées, nous développons un index de qualité d’ECG à base spectrale de modulation qui est semblable à une mesure de ratio “rapport signal sur bruit”.

Pour calculer cette mesure, le premier “lobe” a besoin d’être détecté dans chaque spectrogramme de modulation par bordure  $\mathcal{X}(f, f_{m,k})$ , correspondant ainsi au rythme cardiaque instantané de l’utilisateur. A cet effet, l’énergie pour chaque groupe de fréquence de modulation est calculée entre  $0.8 \leq f_m \leq 3.3$  Hz (couvrant ainsi les rythmes cardiaques entre 48 et 198 bpm) et en moyenne au-dessus de la fourchette  $0 \leq f \leq 40$  Hz. Le groupe de fréquence de modulation  $f_m^*$  avec l’énergie la plus élevée est sélectionnée comme centre du premier lobe. Nous avons découvert expérimentalement qu’une bande passante d’un lobe de 0.625 Hz (ex. un groupe de fréquence de modulation sur la droite et un groupe de fréquence de modulation sur la gauche de  $f^*(2B)$ , comme montré sur la partie droite de la figure 2.8 (cadre  $k$ )), résulte dans des résultats fiables et précis.

Ensuite, l’énergie totale de modulation de l’ECG (EME) pour le cadre  $k$  nécessite le calcul d’une somme d’énergies de modulation présentes dans le lobe principal avec ses harmoniques. Dans l’intérêt d’un bilan de qualité, nous avons testé le calcul d’un paramètre EME utilisant entre 1 – 4 harmoniques et avons trouvé que trois harmoniques (ex. un total de 4 lobes) conduit à la meilleure performance. De ce fait, l’énergie de modulation d’ECG est calculée ainsi :

$$EME(k) = \sum_{j=1}^4 \mathcal{X}(f|_0^{40}, jf_{m,k}^* - B \leq jf_{m,k}^* \leq jf_{m,k}^* + B), \quad (1)$$

où  $f|_0^{40} = 0 \leq f \leq 40$  et  $B = 0.3125$  Hz.

L'hypothèse est que le paramètre EME représente l'information disponible depuis les composants actuels d'ECG et que tous les éléments à l'extérieur des quatre premiers lobes correspondent aux bruits/artéfacts. De ce fait, l'index de qualité de modulation spectrale de base par bordure (RME) est:

$$MS - QI(k) = \frac{EME(k)}{RME(k)}, \quad (2)$$

où RME est calculé comme étant la différence entre l'énergie totale dans le spectrogramme de modulation et l'EME. L'index final de qualité  $MS - QI$  est donné comme  $MS - QI(k)$  moyen au-dessus de tous les cadres dans le signal d'ECG enregistré. Pendant que l'indicateur n'est pas automatiquement calé entre 0 et 1, nous avons observé expérimentalement que les valeurs MS-QI sont typiquement entre 0 – 1.5, avec les plus hautes valeurs correspondant à la qualité améliorée.

#### 0.4.1 Ensemble de données 1: Données synthétiques d'ECG

Nous avons utilisé la fonction Matlab *ecgsyn* disponible dans Physionet pour générer des signaux d'ECG synthétiques [21]. Pour les expériences décrites ci-inclus, 200 signaux de 120 secondes furent générés avec deux paramètres d'entrées testés aléatoirement: le rythme cardiaque (testé uniformément entre 50 et 80 battements par minute) et le ratio LF/HF (testé uniformément entre 0.5 et 8.9). La gamme de rythmes cardiaques a été choisie pour couvrir certaines maladies du cœur (ex. tachycardie), tout comme pour différents niveaux d'activités (ex. au repos, marche et course). La gamme de ratio LF/HF, quant à elle, couvre l'éveil, le mouvement rapide de l'œil, le sommeil léger puis profond et l'infarctus du myocarde [15]. Les signaux bruyants ont été générés avec des RSB de -5 dB, 0 dB, 5 dB, 15 dB et 30 dB, d'après les étapes décrites en [9]. Au total, plus de 40 heures de données d'ECG (propres et bruyants) sont disponibles pour les tests.

#### 0.4.2 Ensemble de données 2: Données d'ECG enregistrées pour le vêtement Hexoskin

Pour tester l'indicateur de qualité développé dans des données réelles enregistrées, nous utilisons le vêtement intelligent Hexoskin qui est équipé d'un textile ECG respirant et d'accéléromètres 3D (voir figure 3.1). Les signaux ECG single-channel sont recueillis avec un taux de 256 Hz et une résolution de 12 bits. L'Hexoskin transmet les données aux appareils intelligents via une connexion Bluetooth, étant ainsi un candidat idéal pour les applications de télémédecine qui peuvent vraiment bénéficier d'un index de qualité objectif. Dans cette configuration, les données sont recueillies depuis trois utilisateurs portant le vêtement Hexoskin durant trois activités différentes: assis, marche et course. La figure 3.2 (a) décrit un profil

d’actimétrie mesuré via les accéléromètres de l’appareil et montre le protocole expérimental utilisé: approximativement 1 minute en position assise (niveau d’actimétrie: 0-50 unités arbitraires), suivies par 15 minutes de course (niveau d’actimétrie: 250-350 unités arbitraires) et enfin 3 minutes de marche (niveau d’actimétrie: 50-150). Les niveaux d’actimétrie sont données chaque seconde. Les figures 3.2 (b) et (c) décrivent quant à elles un extrait de 10 secondes de données d’ECG collectées lors des trois niveaux d’activités, tout comme leurs spectrogrammes de modulation respectifs. Comme nous pouvons le voir dans les deux sous-races, les valeurs d’actimétrie sont inversement proportionnelles à la qualité (ex. haut niveau d’activité, faible qualité d’ECG), comme décrit en [22]. En général, environ une heure de données est disponible pour les tests.

### **0.4.3 Ensemble de données 3: Base de données Physionet du défi de qualité de signal**

Afin de tester plus tard l’algorithme proposé, nous avons utilisé un sous-ensemble de l’ensemble de données Physionet/Computing in Cardiology 2011 Challenge disponible publiquement [23]. Les données sont composées des douze meilleurs ECG collectés à un cadencement de 500 Hz utilisant les machines d’ECG. La qualité globale sur les 12 meilleurs a été annotée manuellement par un groupe de 23 volontaires, étant peu, voire nullement expérimentés concernant la lecture des ECG, qui seront par la suite classés comme “acceptable” ou “inacceptable”. Ici, 100 enregistrements acceptables et inacceptables d’une durée de 10 secondes ont été sélectionnées aléatoirement puis cadencés plus faiblement à 256 Hz. Depuis qu’un taux global acceptable a été donné sur les 12 meilleurs (ex. à la majorité des votes, si la majorité des meilleurs sont acceptables, les 12 signaux seront jugés acceptables), nous avons découvert que certains signaux “acceptables” sélectionnés aléatoirement ont été en réalité inacceptables et inversement. De ce fait, deux évaluateurs ont inspecté visuellement les 200 signaux “single-lead” et les ont ré-étiquetés. Plus globalement, les évaluateurs ont été d’accord sur 142 des 200 signaux, les expériences décrites ci-inclus sont ainsi basées sur 71 signaux “acceptable” et 71 signaux “inacceptable”, totalisant 24 minutes de données d’ECG disponibles pour les tests.

### **0.4.4 Ensemble de données 4: Données d’ECG ambulatoires enregistrées**

Dernièrement, nous sommes intéressés lors de nos tests si le MS-QI pourrait convenir à des enregistrements d’ECG pathologiques, validant ainsi son utilisation pour des opérations de télémédecine isolées. Nous avons utilisé la célèbre base de données d’arythmie Physionet MIT-BIH prévue à cet effet [24]. Les données sont composées d’enregistrements d’ECG ambulatoire two-channel collectés sur 47 patients en cardiologie (cadencés à 360 Hz). Les données ont été analysées indépendamment par deux cardiologues qui ont annoté les interprétations avec des étiquettes de battement, de rythme et de qualité de signal. Concernant

ce dernier, les segments des enregistrements qui ont été jugés bruyants par les évaluateurs ont été étiquetés “bruyants”, tandis que les segments restants sont jugés pour être propres. D’après nos expériences, 62 segments propres et 65 segments bruyants d’ECG d’une durée de deux minutes ont été utilisés après une baisse de la cadence à 256 Hz, totalisant ainsi 4 heures et 14 minutes de données disponibles pour les tests.

#### 0.4.5 Mesures de qualité de la référence

Pour des raisons de performance de comparaison, deux mesures de références très exploitées ont été utilisées [25]. La première est le kurtosis d’échantillon d’ECG ( $\kappa$ ) [26] ou le moment de quatrième ordre. Le second indicateur est le ratio de puissance spectrale (IOR) dans le complexe QRS [15]. Notons que l’indicateur MS-QI proposé peut être vu comme une extension de l’indicateur IOR, dans le sens où il ressemble aussi aux ratios des composants ECG et “non-ECG”, mais ayant l’avantage d’avoir accès à une plage d’informations plus large via le contenu de fréquence de modulation.

#### 0.4.6 Bilan de performance

Pour évaluer l’efficacité des mesures proposées et de référence dans les deux premiers ensembles de données, deux figures de mérite de performance ont été utilisées, à savoir les corrélations de rang de Pearson et de Spearman. La corrélation de Pearson ( $\rho$ ) mesure la relation linéaire entre deux variables  $q(n)$  et  $t(n)$  et est donnée par:

$$\rho = \frac{\sum_{i=1}^N (q(i) - \bar{q})(t(i) - \bar{t})}{\sqrt{\sum_{i=1}^N (q(i) - \bar{q})^2 \sum_{i=1}^N (t(i) - \bar{t})^2}}, \quad (3)$$

où  $\bar{q}$  et  $\bar{t}$  sont respectivement des échantillons moyens de  $q$  et  $t$ .

Ici,  $q(n)$  représente les indices de qualité estimée donnés soit par l’indicateur proposé, soit par les mesures des deux références. La variable  $t(n)$  représente quant à elle la valeur de qualité réelle et est donnée ici, soit la valeur d’ECG dans le niveau de cas d’ECG synthétique dans l’ensemble de données 2. Dans ce dernier cas, depuis que seulement trois niveaux d’activités sont présents, les valeurs de qualité estimées sont calculées pour des séries d’extraits de 5 secondes de données enregistrées lors de chaque type d’activité. Tous les indicateurs contrôlés sont liés positivement avec le RSB et négativement liés avec les niveaux d’actimétrie. Le second indicateur, la corrélation de rang de Spearman ( $\rho_S$ ), mesure le rang des indices de qualité contre les “vrais” indicateurs de qualité (ex. RSB et niveau d’activité). L’indicateur  $\rho_S$  est calculé en utilisant (3.3) mais avec les valeurs de données originales remplacées par les rangs des valeurs de données. Un indicateur de qualité fiable aura un  $\rho$  et un  $\rho_S$  proche de l’unité. Pour les troisième et quatrième ensembles de données, depuis que les étiquettes “acceptable” et “inacceptable” (ou “bruyant” et “propre”) sont disponibles, nous utilisons

le chevauchement dans les distributions entre les deux classes comme figure de mérite. Un chevauchement plus petit indique une plus grande séparabilité des classes, donnant ainsi un meilleur index de qualité. Un test de deux échantillons de Kolmogorov-Smirnov est utilisé pour quantifier statistiquement la séparabilité des deux distributions. Plus généralement, 45 heures et 38 minutes de données d’ECG sont utilisés pour nos analyses.

#### 0.4.7 Résultats

Le tableau 3.1 montre une performance obtenue avec les indicateurs proposé et de référence pour les ensembles de données 1 et 2. Pour l’ensemble de données 1, les corrélations sont entre les indicateurs obtenus et les valeurs RSB pour les 1000 signaux (200 signaux  $\times$  5 niveaux de RSB). Pour l’ensemble de données 2, les corrélations sont entre les indicateurs obtenus et les niveaux d’actimétrie. Les diagrammes de dispersion décrits dans les figures 3.3 (a)-(c) montrent le comportement du MS-QI,  $\kappa$ , et des indicateurs IOR, respectivement comme une fonction du RSB pour les signaux d’ECG synthétiques. Pour éviter le désordre, seules les valeurs d’indicateurs moyennes par RSB sont montrées, avec leurs déviations standard. De plus, les figures 3.4 (a)-(c) montrent le comportement du MS-QI,  $\kappa$ , et les indicateurs IOR en tant que fonction du niveau d’actimétrie pour l’ensemble de données 2. Pour éviter toute confusion, seulement 5 secondes d’extraits par niveau d’activité sont présentées. Comme nous pouvons le voir, un comportement logarithmique est présent, les performances dans le tableau 3.1 étant ainsi listées sans une cartographie logarithmique.

Enfin, pour les ensembles de données 3 et 4, nous utilisons le chevauchement dans les distributions entre les signaux d’ECG propres (acceptables et de bonne qualité) et les signaux bruyants (inacceptables et de mauvaise qualité) comme figure de mérite. Pour l’indicateur MS-QI, le noyau convient pour les distributions de probabilité comme décrit en figure 3.5, où les courbes noires foncées correspondent aux enregistrements propres et les courbes gris clair aux enregistrements bruyants. Les lignes discontinues sont pour la base de données 3 et les lignes pointillées pour la base de données 4. Dans le but de comparaisons, les données synthétiques d’ECG sont représentées par des lignes continues noires et les données synthétiques bruyantes (ex.  $\text{RSB} \leq 15$  dB) par des lignes continues grises. Pour des raisons de simplification, les comparaisons se font seulement pour l’indicateur de référence, comme il est utilisé plus régulièrement dans les ensembles de données 1 et 2, celui-ci étant relatif à la référence IOR (voir tableau 3.1). Les figures 3.6 (a) et (b) montrent que le noyau convient aux distributions de probabilité pour les ensembles de données 1, 3 et 4. Comme précisé précédemment, les lignes noires correspondent à la bonne qualité de l’ECG et les lignes grises aux enregistrements de mauvaise qualité.

#### 0.4.8 Discussion

Nous pouvons voir dans la table 3.1 que l'indicateur MS-QI proposé est plus performant que les deux algorithmes de référence dans les ensembles de données 1 et 2 en termes d'indicateur de performance  $\rho$ . Par rapport à l'indicateur  $\rho_S$ , les résultats sont égaux à  $\kappa$  dans les deux ensembles de données et surpassent l'indicateur IOR dans l'ensemble de données 2. D'autre part, l'indicateur IOR possède le plus haut  $\rho_S$  dans l'ensemble de données 1. Globalement, la cohérence de l'indicateur MS-QI dans les deux ensembles de données montre qu'il peut être plus convenable pas seulement pour les applications de télémédecine, mais aussi pour les applications d'entraînement où les données d'ECG sont hautement contaminées par les mouvements d'artéfacts. En réalité, si nous comparons le nuage de points pour l'indicateur MS-QI en figure 3.4 (a) à celui de référence  $\kappa$  par rapport au log de l'actimétrie en figure 3.7, nous pouvons observer que la discrimination entre les trois niveaux d'activités, particulièrement entre les conditions de marche et de course, reste élevé pour l'index de qualité proposé, suggérant ainsi des applications potentielles comme un détecteur de type d'activité. Il est intéressant de souligner que dans les trois conditions d'activité explorées dans l'ensemble de données 2, la position assise est l'une des activités montrant la plus haute variabilité, particulièrement pour les indicateurs de référence. Ceci peut être un artéfact dans le protocole de collecte de données, la position assise étant la première activité réalisée pour la collecte de données et le couplage d'ECG de textiles peut avoir été plus faible, dû au manque d'humidité et de sueur [27]. De plus, les gains de performance relatifs à l'indicateur IOR dans les deux ensembles de données montrent l'importance de l'information spectrale de modulation pour le développement d'une mesure de RSB aveugle pour les signaux d'ECG.

Comme mentionné précédemment, la mesure MS-QI proposée conclut des résultats comparables avec la référence  $\kappa$ , particulièrement pour l'indicateur  $\rho_S$ . Les bénéfices de l'indicateur MS-QI proposé deviennent cependant plus apparents pour la collecte de données dans de vraies conditions, comme dans les ensembles de données 3 et 4. Dans la figure 3.5, nous pouvons voir que le chevauchement dans les distributions de probabilité entre le bon et le mauvais signal ECG est minime pour l'indicateur MS-QI, avec une limite claire entre les deux conditions pour un MS-QI = 0.5. Cette découverte reste vraie non seulement pour l'ECG synthétique, montrant ainsi la résistance de l'indicateur proposé pour le type d'ECG (enregistré/synthétique) comme pour les conditions du patient (en bonne santé/pathologique). D'autre part, l'indicateur  $\kappa$  montre qu'il est plus sensible aux ECG avec des différences visibles dans les distributions de probabilité entre les ECG enregistrés (figure 3.6a) et synthétiques (figure 3.6b). Même si la limite  $\kappa = 5$  entre les deux conditions, comme montré en [28], peut être vu avec les ECG synthétiques, il augmente de presque 10 avec les données enregistrées. Ce comportement peut être dû à la sensibilité dans le moment du quatrième ordre aux valeurs aberrantes dans les signaux bruyants, pouvant être mal interprété comme battements dans les enregistrements propres d'ECG [28]. De plus, l'indicateur  $\kappa$  montre un

chevauchement très élevé dans les distributions de probabilité dans l'ensemble de données 4, limitant ainsi son utilisation pour le contrôle de qualité pour les ECG pathologiques. Afin de quantifier statistiquement cette séparabilité, un test de Kolmogorov-Smirnov a été utilisé. Pour le paramètre  $\kappa$ , la différence entre les deux distributions a été jugée négligeable ( $p = 0.11$ ), tandis que la séparabilité fut plus évidente pour la mesure du MS-QI proposé ( $p < 10^{-30}$ ).

D'autre part, le temps de calcul pour un signal d'ECG de 2 minutes a été autour de 0.2 secondes pour l'indicateur MS-QI proposé, 0.04 secondes pour l'IOR et 0.02 secondes pour le  $\kappa$ . Même si l'index de qualité proposé était à peu près 10 fois celui de  $\kappa$  et 5 fois celui de l'IOR, ces découvertes démontrent, dans de vraies conditions, que l'indicateur proposé surpasse les références ayant plus d'importance que la limitation dans la complexité du calcul. Cependant, il est important de préciser que les codes Matlab développés ici peuvent être optimisés pour un travail à l'avenir afin de réduire le temps de processus.

## 0.5 Filtre spectro-temporel pour la détection de pic

Typiquement, le taux de changement pour les signaux biologiques diffère radicalement de ceux du bruit, le filtrage pouvant ainsi être utilisé pour des raisons de suppression de bruit. Ici, une approche de filtrage de domaine de modulation pour la suppression de bruit des ECG aveugles et single-channel a été proposé. La figure 2.8 illustre les étapes de processus du signal concernées dans le calcul de la représentation spectrale de modulation d'ECG. Depuis que les transformations inversées sont utilisées pour trouver la représentation du signal spectro-temporel, le filtrage peut être effectué dans le domaine spectral de modulation et le signal résultant peut être reconstruit dans un ECG sans bruit.

Comme vu dans la figure 2.8, les signaux propres d'ECG sont composés de 'lobes' clairs dans le domaine de modulation correspondant aux composants stationnaires et non-stationnaires. L'information du rythme cardiaque est clairement encodée dans le premier lobe et ses harmoniques. Cependant, ces lobes ne sont pas aussi clairs avec les ECG bruyants, dus aux composants spectraux de modulation bruyants répandus entre les lobes. De ce fait, nous proposons d'utiliser une série de filtres de bande passante dans le domaine de modulation pour filtrer et supprimer les composants du bruit. La fréquence de modulation centrale des filtres de bande passante sont capables de s'adapter au signal et de faire confiance à la découverte du  $f_m$  correspondant à l'énergie de modulation en pic entre  $0 \leq f \leq 40$ . Afin d'accélérer le processus, nous avons limité la recherche à un  $f_m$  entre  $0.8 \leq f_m \leq 3.3$ , correspondant ainsi approximativement à un HR entre  $48 \leq HR \leq 198$  bpm. De plus, dans le but de supprimer les composants du bruit stationnaires, les composants des filtres passe-bas proches de  $f_m = 0$  Hz ont été aussi supprimés. La suppression de ces composants affecte la reconstruction du signal d'ECG pour les applications non-cliniques (ex. contrôle de performance d'athlète) ayant

ainsi un impact moindre. Cependant, il est important de noter que pour les applications nécessitant la reconstruction des complexes PQRS, de futures recherches seront nécessaires pour mettre en place des stratégies de filtrage alterné pour les composants autour de  $f_m = 0$  Hz.

La figure 4.1 illustre le diagramme fonctionnel des étapes du processus du signal impliqué dans le schéma de filtrage de modulation et les étapes effectuées dans chaque module de processus de modulation. Pour des besoins de notation, laissons  $s(f, m)$ ,  $f = 1, \dots, N$  et  $m = 1, \dots, T$ , désigner le composant spectral à court terme au groupe de fréquence  $f^{th}$  et le pas de temps  $m^{th}$  pour l'analyse à court terme.  $T$  et  $N$  signifient respectivement le nombre total de pas de temps et les bandes de fréquence. Pour une bande de fréquence  $f = F$ ,  $s(F, m)$ ,  $m = 1, \dots, T$  représente la trajectoire temporelle de bande  $F^{th}$ . Ici, les bandes de fréquence en-dessous de  $f = 40$  Hz sont traitées. Pour simplifier la description de l'algorithme, les transformations de Fourier (DFT) sont montrées dans la figure et le texte; mais en pratique, une transformation rapide de Fourier a été implémentée.

Pour le traitement, le signal d'ECG est affiché dans une fenêtre de sinus complémentaire de puissance de 32 points avec 75% de dépassement. Une DFT de 32 points (pas de zero-padding) est donc prise et la magnitude ( $|s(f, m)|$ ) et les composants de la phase ( $\angle s(f, m)$ ) de chaque groupe de fréquence (jusqu'à 40 Hz) sont saisis dans un module de "processus de modulation" où le filtre de modulation et la compensation de retard de phase sont effectués. Les résultats des modules  $N$  correspondent à la magnitude produite ( $|\hat{s}(f, m)|$ ) et les composants de la phase ( $\angle \hat{s}(f, m)$ ), sont saisis dans une DFT inversée pour créer  $\hat{s}(m)$ . Le résultat est affiché avec la fenêtre complémentaire de puissance et la méthode "d'overlap-and-add" est utilisée pour reconstruire le signal avec le bruit supprimé.

En substance, la trajectoire de magnitude "par groupe de fréquence"  $|s(f, m)|$ ,  $m = 1, \dots, T$  est filtrée en utilisant une banque de filtres de modulation de bande passante de réponse imputée finie (FIR) de phase linéaire adaptative  $B$  (appelée  $BP_b$ ) pour générer des signaux  $|\hat{s}_b(f, m)|$ , où 'b' signifie l'index de filtre de bande passante. Les expériences ont démontré que le débit de lobe dans le domaine de modulation est approximativement de 0,625 Hz. En utilisant l'algorithme présenté en [29], les filtres de bande passante de ce débit ont été élaborés, correspondant ainsi à une longueur de 101 coups. Pour chaque signal d'ECG,  $B$  est trouvé dans la fréquence de modulation centrale du lobe principal (se basant ainsi sur le rythme cardiaque) et la fréquence de modulation maximale possible basée sur le choix de la fenêtre et des durées de déplacement dans la première transformation. Dans nos expériences, cela correspondait à 16 Hz,  $B$  variant ainsi entre 5 et 10, couvrant le lobe principal, plus entre 4 et 9 harmoniques.

Les signaux  $|\hat{s}_b(f, m)|$  sont ainsi ajoutés au résultat final  $|\hat{s}(f, m)|$ . Cependant, après le filtrage de la bande passante, la suppression du contenu spectral de modulation de la bande passante peut résulter dans des valeurs spectrales de puissance négative. De ce fait, la recti-

fication à semi-vague (HWR) est effectuée pour autoriser la reconstruction du signal. Enfin, l'étape restante de processus de modulation consiste à décaler la phase sur 50 échantillons, correspondant au retard de groupe des filtres de phase linéaire implémentés, résultant ainsi dans  $\angle\hat{s}(f, m)$ . La figure 4.2 montre un signal d'ECG avec 60 bpm et un RSB de  $RSB = -5$  dB avant et après filtrage de modulation. Pour des raisons de comparaison, le résultat de l'algorithme de suppression de bruit des vaguelettes est aussi montré, ainsi que les spectrogrammes de modulation des signaux bruyants et des deux signaux améliorés. Une fois que l'ECG bruyant est amélioré, l'algorithme de Pan Tompkins est appliqué pour extraire les pics R et les séries de temps RR, qui sont donc ajoutés au logiciel open-source HRVAS pour calculer les indicateurs HR et HRV [30].

### 0.5.1 Base de données 1: ECG synthétique

Les données des ECG synthétiques ont été créées en utilisant la fonction Matlab 'ecgsyn' inclut dans Physionet [21]. Ici, 700 séquences de deux minutes de signaux cadencés à 256 Hz ont été générés avec des valeurs de rythmes cardiaques comprises entre 50 bpm et 180 bpm. Les signaux clairs d'ECG synthétiques ont été contaminés à des niveaux connus, dans le but de générer des signaux sur 5 différents niveaux de RSB, à savoir -10, -8, -5, 0 et 5 dB. En général, 3500 séquences de signaux bruyants de deux minutes ont été disponibles pour l'étude, totalisant plus de 116 heures de données d'ECG pour les tests.

### 0.5.2 Base de données 2: Défi de données de Physionet 2014

Dans le but de tester l'algorithme dans les conditions les plus réalistes, l'ensemble de données Physionet/Computing in Cardiology 2014 a été utilisé. Le challenge a exploré des méthodes pour localiser les rythmes cardiaques lors d'enregistrements à long terme, continus et sur plusieurs chaînes depuis des moniteurs situés sur les lits de patients possédant de nombreux problèmes et des patients en bonne santé. Comme précisé en [31], la qualité du signal de l'ECG a varié considérablement au fil du temps, rendant difficile la détection de la fréquence cardiaque moyenne. Nous avons utilisé ici les signaux d'ECG depuis les phases d'entraînement et d'entraînement étendu, contenant des fichiers d'annotation de rythmes cardiaques de référence trouvés par des experts volontaires. Les données combinées des deux phases contenaient 200 signaux de dix minutes (ou assez court) et une fréquence d'échantillonnage de 250 Hz (dans certains cas dans la phase étendue, un taux d'échantillonnage de 360 fut utilisé).

### 0.5.3 Algorithme de référence et bilan de performances des indicateurs

Deux algorithmes de référence ont été étudiés, un basé sur l'EMD [32] et l'autre sur la suppression de bruit des vaguelettes [33]. Lors des d'expériences d'essai, il a été découvert

que la vaguelette de référence fut plus performante que celle de l'EMD, ces derniers résultats étant ainsi rapportés dans le premier. La performance de l'algorithme de suppression de bruit des vaguelettes dépend du choix de plusieurs paramètres, tels que la fonction mère, la méthode de seuil, le nombre de niveaux de décomposition et les règles de sélection de seuil; typiquement, ceux-ci sont sélectionnés empiriquement [33]. Lors de nos expériences, nous avons exploré les seuils élevé et faible, ainsi que plusieurs différentes règles de rétrécissement, à savoir: universelle, Stein's Unbiased Risk Estimate – SURE (Estimation Impartiale des Risques de Stein), la règle SURE heuristique et minimax.

Dans le but d'optimiser les paramètres d'algorithmes de référence pour la tâche manuelle, 100 fichiers de la base de données 1 ont été utilisés. Le tableau 4.1 liste les erreurs terminées (en pourcentage) des estimations des rythmes cardiaques entre celui estimé depuis le signal relatif amélioré et le vrai battement pour différents niveaux de RSB. Comme nous pouvons le voir, l'algorithme de référence a supprimé les artefacts nécessaires pour atteindre la parfaite estimation du meilleur rythme cardiaque pour les niveaux de RSB plus grands que 0 dB. Cependant, pour des conditions extrêmes de bruit, la méthode universelle de rétrécissement donne lieu à la meilleure performance, ainsi utilisée lors de nos expériences. De plus, les vaguelettes mères Daubechies 6, décomposées sous 8 niveaux, furent utilisées selon nos connaissances [34] et les expériences pilotes.

Concernant la performance, plusieurs indicateurs sont utilisés pour mesurer les bénéfices que peut apporter l'algorithme proposé. Pour les signaux synthétiques ECG (base de données 1), depuis que nous avons accès au signal pur original, les indicateurs suivants ont été utilisés: (1) pourcentage d'erreur du rythme cardiaque; (2) post-amélioration RSB; (3) kurtosis ( $\kappa$ ) mesuré dans une fenêtre autour des pics R dans les complexes QRS; (4) pourcentage d'erreur dans l'intervalle inter-battement et (5) pourcentage d'erreur statistique entre le signal pur et le signal amélioré. L'indicateur pNN50 fait partie du domaine de temps de la famille pNNx [35] et correspond à la fraction des intervalles de sinus consécutifs normaux (NN) qui diffèrent de plus de 50 ms. Dans le cas de la base de données 2, depuis que les fichiers d'annotation des battements de référence sont disponibles, le pourcentage d'erreur du rythme cardiaque a été utilisé.

#### 0.5.4 Résultats expérimentaux et discussion

Le tableau 4.2 rapporte le pourcentage d'erreur du rythme cardiaque,  $\kappa$ , et le RSB pour les signaux bruyants dans la base de données 1, ainsi que les indicateurs de performance post-amélioration pour les algorithmes de référence et améliorés. Les points dans la figure 4.3 (a) et (b) représentent un à un les erreurs d'intervalle inter-battement et les erreurs pNN50, pour le signal bruyant, ainsi que les algorithmes proposés et de référence (suppression de bruit) pour la base de données 1. Enfin, la figure 4.4 illustre en fonction de la base de données 2 les

adéquations du noyau pour les distributions probables des pourcentages d’erreurs de rythme cardiaque pour les sous-données d’entraînement et d’entraînement étendu combinés.

Dans le tableau 4.2, nous pouvons voir que le pourcentage d’erreur du rythme cardiaque moyen sur différents rythmes cardiaques et rapports basse fréquence/haute fréquence était proche d’un tiers de la valeur de référence trouvée. Aussi, l’amélioration du RSB moyen pour les signaux bruyants (RSB = -10, -8, -5 et 0 dB) avec l’algorithme proposé était de 9 dB comparé aux 4 dB de référence. Les améliorations du RSB se sont améliorées avec les signaux bruyants. Un  $\kappa$  moyen augmente au-dessus du signal bruyant où 4 a été obtenu avec l’algorithme proposé, rendant ainsi plus performant la légère amélioration de 0.1 avec la référence. En utilisant le seuil de  $\kappa$  à 5, comme suggéré en [25, 28] pour indiquer une bonne qualité de l’ECG, cela sera atteint avec la solution proposée, même dans des cas extrêmement bruyants (RSB = -10 dB), étant ainsi comparé favorablement par rapport à la référence ce qui a été atteint avec un RSB de 0 dB. En général, la solution proposée à un meilleur facteur  $\kappa$  de déviation standard, d’environ 1.6, quel que soit le RSB testé. Malgré la haute déviation, les augmentations de  $\kappa$  avec l’algorithme proposé furent significativement plus hautes que celles atteintes avec la référence à travers tous les niveaux de RSB. En explorant une large gamme de rythmes cardiaques et de rapports basse fréquence/haute fréquence, ces résultats démontrent que l’algorithme proposé est beaucoup plus performant dans une large gamme de rythmes cardiaques et dans des conditions d’ECG normales et anormales. De plus, comme montré dans le tableau 4.2 pour un RSB d’entrée de -10 dB, la déviation standard du pourcentage d’erreur du rythme cardiaque est plus haute que la moyenne. Une analyse plus poussée a montré que cette large variation était due aux grandes erreurs obtenues avec un rythme cardiaque faible ( $50 \leq \text{bpm} \leq 80$ ), probablement dû aux limitations dans l’algorithme de détection des pics de Pan Tompkins [36]. En général, les résultats obtenus démontrent que l’algorithme proposé peut être plus approprié pour une amélioration de la qualité de l’ECG, plus particulièrement dans des cas de bruits extrêmement forts mais montre une limite quant à la mesure de la variabilité de la fréquence cardiaque dans des cas de bruits forts, même avec l’aide d’un algorithme d’amélioration.

Malgré cela, grâce aux tracés en figure 4.3, nous pouvons également voir que l’algorithme proposé résulte dans les analyses d’amélioration de la variabilité de la fréquence cardiaque, réduisant l’intervalle inter-battement et les erreurs pNN50 relatives au signal bruyant. Par rapport à la référence, des hausses de 2.6% et de 15% ont respectivement été atteintes. De plus, les hausses les plus importantes ont été observées lors de valeurs faibles de RSB, montrant ainsi les avantages de l’algorithme proposé, comme lors d’études récentes démontrant l’importance de tels indicateurs de HRV lors de surveillances sur des performances d’athlètes [37] [38], pilotes [39], astronautes [40] et joueurs de basketball [41] par exemple. Enfin, d’après la base de données 2, la figure 4.4 montre les avantages de l’algorithme proposé avec un ECG de faible qualité enregistré dans des cas de figure réalistes. Le pourcentage d’erreur

du rythme cardiaque obtenu avec l’algorithme proposé était autour de 0 avec une déviation standard d’environ 1%. Les méthodes bruyantes et d’amélioration des vaguelettes d’un autre côté présentent une variabilité avec une déviation standard d’environ 8%.

Globalement, il a été démontré que le temps informatique de l’algorithme proposé était à peu près deux fois celui de référence dans les ‘pires des cas’, impliquant de faibles valeurs de battements, ainsi que plus de filtres de bande passante que nécessaire. Cependant, il a été également prouvé que les hausses d’amélioration d’ECG obtenues avec l’algorithme proposé sur la référence pèsent beaucoup sur cette limitation, plus particulièrement depuis que cet intervalle de complexité statistique diminue à la plus haute représentation des battements des fonctions ciblées. Néanmoins, Il est important de souligner le fait que les codes Matlab appliqués ci-inclus n’ont pas été optimisés pour le temps de traitement, c’est pour cela que des réductions supplémentaires peuvent toujours être atteintes.

## 0.6 Modulation de la mesure du domaine de variabilité de fréquence cardiaque

Comme défini dans la section 0.3, la représentation spectro-temporelle de l’ECG permet de distinguer la modulation des composants spectraux, même dans des cas de bruits extrêmement forts, comme décrit dans la figure 5.1 pour un signal d’ECG avec 120 bpm et un RSB de -10 dB. Nous proposons ici un indicateur HRV de domaine de nouvelle modulation, appelé ‘MD-HRV’. Afin de calculer l’indicateur, la fréquence centrale (c’est-à-dire le premier lobe) à l’intérieur de chaque spectrogramme de modulation par bordure  $\mathcal{X}(f, f_{m,k})$  doit être détectée; celle-ci est représentée par les lobes colorés dans les spectrogrammes de modulation dans la figure 2.8. Pour cette raison, l’énergie pour chaque groupe de modulation de fréquence est calculée avec  $f$  entre 0 et 40, là où la plus grande énergie d’ECG est concentrée. La fourchette de modulation de fréquence avec la plus grande énergie entre 0.8 et 3.3 est sélectionnée en tant que centre du premier lobe. La série des valeurs  $f_m$  a été choisie pour couvrir les rythmes cardiaques entre 48 et 198 bpm, cernant ainsi les différentes maladies cardiaques et niveaux d’activités. Pour la notation, laissons  $\mathcal{X}_k = \mathcal{X}(f, f_{m,k})$ , calculant ainsi le MD-HRV pour tous les spectrogrammes de modulation en utilisant:

$$MD - HRV = \sqrt{\frac{1}{N-1} \sum_{k=1}^N (\mathcal{X}_k - \bar{\mathcal{X}})^2}, \quad (4)$$

Où  $N$  est le nombre total de ‘bordures de modulation’,  $\mathcal{X}_k$  la fréquence centrale à la modulation de fréquence  $k^{th}$  et  $\bar{\mathcal{X}}$  la fréquence centrale simple calculée pour tous les spectrogrammes de modulation de fréquence par bordure. Ici, les spectrogrammes de modulation sont estimés toutes les 5 secondes avec 75% de chevauchement.

### 0.6.1 Base de données 1: ECG synthétique

Les signaux synthétiques d’ECG ont été générés en utilisant la fonction ‘ecgsyn’ dans Matlab<sup>TM</sup>, disponible dans Physionet [21]. Ici, 700 signaux d’une durée de 10 minutes cadencés à 256 Hz ont été créés en testant aléatoirement la déviation standard du rythme cardiaque entre 1 et 10 bpm pour les rythmes cardiaques allant entre 50 et 180 bpm. Les signaux synthétiques purs ont été corrompus par plusieurs artéfacts à différents niveaux de RSB connus. Les signaux bruyants ont été générés à 6 niveaux de RSB (-10 dB, -8 dB, -5 dB, 0 dB, 5 dB et 10 dB). Plus généralement, 4200 signaux bruyants de 10 minutes (700 heures) ont été générés par le bilan d’indicateurs HRV.

### 0.6.2 Base de données 2: Base de données Arythmie MIT-BIH

Dans l’optique de tester les indicateurs HRV proposés dans des signaux pathologiques réalistes, la base de données Arythmie MIT-BIH a été également utilisée [42]. Pour les expériences ci-incluses, les signaux dual-channel ont été segmentés pour créer des séquences de 10 minutes baissées à une cadence de 256 Hz. Ainsi, 288 séquences de 10 minutes ont été créées au total, fournissant 48 heures de tests. Ces séquences ont été groupées en accord avec le rythme cardiaque (HR) et la déviation standard du rythme cardiaque (sdHR), similaire aux signaux synthétiques d’ECG, permettant ainsi une meilleure comparaison entre les deux bases de données, d’où 4 groupes ont été déterminés: Groupe 1 ( $60 \pm 10$ bpm), Groupe 2 ( $80 \pm 10$  bpm), Groupe 3 ( $100 \pm 10$  bpm) et Groupe 4 ( $120 \pm 10$  bpm).

### 0.6.3 Référence et figures de mérite

Dans l’optique de comparer l’indicateur MD-HRV proposé avec les références “gold standard”, plusieurs domaines de temps, domaines de fréquence et les indicateurs HRV non linéaires. Les indicateurs du domaine de temps HRV comprennent i) SDNN, ii) SDANN et iii) stdHR. L’indicateur de domaine de fréquence mesure à tour de rôle la puissance spectrale totale contenue dans toutes les sous-bandes de fréquence telle que VLF (Très Basse Fréquence), LF (Fréquence Basse) et HF (Haute Fréquence). Enfin, les tracés non-linéaires de Poincaré sont utilisés avec les paramètres dénommés SD1 et SD2 [43].

De plus, un algorithme d’amélioration d’ECG en vaguelettes [44] fut utilisée pour la suppression des anciens éléments avant la mesure des références HRV. Ce genre de configuration illustre le processus utilisé dans les applications de pointe de contrôle d’HRV existantes [45]. Ici, des comparaisons seront faites entre l’indicateur MD-HRV proposé, calculé depuis le signal bruyant, et les indicateurs de référence HRV calculés depuis les signaux bruyants et améliorés. Basés sur les connaissances en [34], les vaguelettes mères Daubechies-6 décomposées sous 8 niveaux, combinées avec un seuil faible et un rétrécissement universel, ont été

utilisés [46]; comme les paramètres trouvés dans la meilleure performance d'amélioration dans les deux ensembles de données utilisés ci-joint.

Comme pour les figures de mérite, les corrélations de Pearson ( $\rho$ ) et Spearman ( $\rho_s$ ) ont été utilisées pour mesurer les avantages de l'indicateur MD-HRV proposé. Dû à la disponibilité du signal synthétique original pur et des fichiers d'annotation pour l'ensemble de données d'arythmie, l'indicateur proposé pourrait être comparé avec les valeurs d'HRV de référence 'de terrain'. La corrélation de Pearson montre la relation linéaire entre les indicateurs MD-HRV et 'vrai' HRV. La corrélation de Spearman mesure comment le MD-HRV se classe parmi les 'vrais' indicateurs. Les valeurs de plus haute corrélation correspondent aux indicateurs améliorés. En outre, pour évaluer la préférence ainsi que l'estimation d'un intervalle de concordance entre les indicateurs, les tracés de Bland-Altman ont été aussi utilisés [47]. Un tracé de Bland-Altman décrit les différences (axe des ordonnées), contre les moyennes (axe des abscisses), d'où ceux-ci sont utilisés pour vérifier le niveau de concordance entre les indicateurs 'vrais' et les MD-HRV proposés [48]. Typiquement, les tracés de Bland-Altman ayant un point de distribution compact autour de 0 (axe des ordonnées) représentent les indicateurs dans une meilleure concordance. Finalement, l'analyse de régression linéaire est également produite pour montrer l'ajustement linéaire avec des intervalles de confiance de 95%; les intervalles de confiance plus petits représentant les indicateurs les plus fiables.

#### 0.6.4 Résultats

Les tableaux 5.1 et 5.2 montrent la comparaison de performance pour les différents indicateurs HRV calculés depuis les signaux bruyants, leurs mêmes vaguelettes améliorées et l'indicateur proposé MD-HRV pour les ensembles de données 1 et 2 respectifs. Les corrélations de Pearson ( $\rho$ ) et de Spearman ( $\rho_s$ ) ont été obtenues entre les 'vrais' indicateurs de référence HRV pour les signaux purs (c'est-à-dire SDNN, SDANN, sdHR, puissance totale, SD1 et SD2) et les indicateurs HRV pour les signaux bruyants et avancés, tout comme entre les 'vrais' indicateurs et le MD-HRV proposé.

Les figures 5.2 (a)-(c) présentes plus loin illustrent les nuages de points (et les courbes de régression linéaire) de l'indicateur sdHR calculés depuis les signaux bruyants (sous-tracé a) et améliorés (sous-tracé b), ainsi que l'indicateur MD-HRV calculé depuis les signaux bruyants (sous-tracé c). Pour éviter l'encombrement du graphique, seuls 100 signaux bruyants à 100 bpm et d'un RSB de -10 dB seront tracés, représentant ainsi des scénarios similaires aux hauts niveaux d'exercice et de mouvement. De plus, les figures 5.3 (a)-(c) montrent les tracés de Bland-Altman pour le Groupe 2 ( $80 \pm 10$  bpm) dans l'ensemble de données 2. L'indicateur de référence sdHR, ci-dessus, calculé depuis le signal bruyant, le signal amélioré, tout comme l'indicateur MD-HRV proposé et calculé depuis le signal bruyant sont indiqués dans les tracés. Nous pouvons clairement voir dans les tracés que les indicateurs MD-HRV résultent dans les plus hautes corrélations, dans les plus petits intervalles de confiance de régression et dans les

tracés plus compacts de Bland-Altman autour de 0 (axe des ordonnées) que l’indicateur de référence sdHR dans les cas: ‘avec’ et ‘sans’ amélioration de vaguelettes.

### 0.6.5 Discussion

Dans ce section, un nouvel indicateur HRV résistant au bruit a été proposé, basé sur une représentation spectro-temporelle d’ECG appelée ‘modulation spectrum’. Le but de cet indicateur fut de mesurer de manière fiable l’HRV dans des circonstances de grand bruit, sans avoir besoin a priori d’amélioration d’ECG ou de détection de pic pour les analyses RR. L’indicateur proposé a été comparé à six indices HRV de référence calculés utilisant le domaine de temps, le domaine de fréquence et les méthodes non-linéaires résumés dans la documentation, avec et sans amélioration d’ECG.

Dans le tableau 5.1, il est montré que les indicateurs de référence HRV calculés depuis les signaux synthétiques bruyants sont généralement en corrélation avec les vraies valeurs d’HRV calculées depuis les signaux purs d’ECG pour des niveaux de RSB plus grands que 0 dB. Cependant, pour des niveaux de RSB faibles, en dessous de -5 dB, certains d’entre eux observés durant un exercice intense ont une mesure de précision de HRV qui se dégrade rapidement. L’amélioration de la vaguelette a démontré à tour de rôle qu’elle était utile pour beaucoup d’indicateurs, particulièrement pour des RSB en dessous de -8 dB.

D’un autre côté, l’indicateur MD-HRV proposé et calculé uniquement avec un signal d’ECG bruyant a montré des valeurs de corrélation stables généralement plus hautes que 0.9, jusqu’à un RSB de -8 dB., avec une baisse jusqu’à 0.71 – 0.76 à un RSB de -10 dB. Dans le cas de bruit élevé, il fut difficile de détecter précisément le lobe principal dans le spectrogramme de modulation (correspondant au rythme cardiaque), compromettant ainsi les mesures d’HRV. Néanmoins, nous avons pu voir qu’avec l’indicateur SDNN, pendant que l’amélioration de la vaguelette a augmenté  $\rho$  par environ 99% relatif au cas bruyant, l’indicateur proposé a surpassé le cas bruyant par 253%. Des augmentations ont été observées à travers tous les indicateurs de référence, incluant SDANN (177% comparé aux 63% de post-amélioration), sdHR (239% comparé aux 27% de post-amélioration), SD1 et SD2 (385% et 184% comparés respectivement aux 161% et 68% de post-amélioration) et la puissance totale (266% comparé aux 68% de post-amélioration). Plus généralement, les valeurs de corrélation obtenues avec les indicateurs MD-HRV à un RSB de -10 dB sont en adéquation avec celles obtenues avec les indicateurs de référence post-amélioration à  $-8 \text{ dB} \leq \text{RSB} \leq -5$ . Une examination plus poussée a montré que l’indicateur de référence HRV de puissance totale résulta dans la faible corrélation avec MD-HRV sur tous les niveaux de RSB. Cet indicateur de référence se montra le plus sensible aux artéfacts, et résulta dans les faibles valeurs de corrélation de tous les indicateurs de référence, même pour un RSB de 10 dB.

Ces résultats ont été vérifiés par la suite depuis la dispersion et les tracés de Brand-Altman illustrés dans les figures 5.2 et 5.3 respectivement, pour les indicateurs sdHR (pré et post-

amélioration) et proposés; les tracés correspondent à 100 signaux d’ECG (100 bpm et RSB à -10 dB) sélectionnées aléatoirement. Les tracés de Brand-Altman montrent par exemple que les divergences entre le vrai sdHR (calculé depuis les signaux purs) et le sdHR calculé depuis les signaux de vaguelettes améliorées avaient une différence de  $11.3 \pm 8.1$ , tandis que l’indicateur MD-HRV proposé, calculé depuis les signaux bruyants, avait une différence de  $2.2 \pm 3.1$ . En somme, les résultats du tableau 5.1 et des figures 5.2 et 5.3 suggèrent que l’indicateur proposé peut être utile dans des conditions extrêmes, là où les signaux d’ECG sont hautement affectés par des artéfacts de mouvement, tels que la période d’effort maximal lors de l’entraînement de performance.

Le tableau 5.2 a reporté les résultats obtenus tour à tour d’après les données d’ECG pathologiques enregistrées. Par rapport au tableau 5.1, les valeurs de corrélation suggèrent une quantité juste de bruit présente dans les enregistrements. L’amélioration des vaguelettes n’a eu aucun impact dans les améliorations de performance pour la plupart des indicateurs de référence, soulignant ainsi les limitations des algorithmes d’amélioration existante pour des données enregistrées dans des conditions réelles. Néanmoins, l’indicateur proposé a fourni des résultats fiables sans l’aide d’une amélioration a priori; globalement, les valeurs  $\rho$  et  $\rho_S$  restent entre 0.8–0.9 pour les six indicateurs de référence. Plus généralement, il a été observé un gain d’environ 49% pour  $p$  avec l’indicateur proposé MD-HRV sur les cas d’amélioration de vaguelette. Dans le cas de signaux synthétiques d’ECG, l’indicateur de référence HR du domaine de fréquence montra qu’il était le plus sensible aux artéfacts. Ainsi, pour l’ensemble de données 2, l’amélioration de vaguelette a détérioré la performance de mesure HRV de référence, due à l’ajout d’artéfacts indésirables post-amélioration. Comme pour les signaux synthétiques, la dispersion et les tracés de Brand-Altman dans les figures 5.4 et 5.5 montrent respectivement des intervalles de confiance plus petits et des distributions plus étroites autour de la valeur nulle de l’axe des abscisses. D’une manière globale, l’indicateur MD-HRV proposé conclut une simple différence de  $0.5 \pm 3.6$  avec le sdHR calculé depuis les étiquettes des rythmes cardiaques originaux, comparant ainsi favorablement la valeur  $-0.9 \pm 5.5$  obtenue avec l’indicateur de référence amélioré. Ces découvertes précisent que l’indicateur proposé supporte non seulement le bruit, mais aussi les différentes pathologies cardiaques, ceci étant un candidat idéal pour le contrôle du patient avec des ECG ambulatoires.

## 0.7 Vers des applications de télésanté sensibles à la qualité

Nous examinons trois classifieurs pour distinguer les signaux d’ECG utilisables de ceux qui ne sont pas utilisables. Plus spécifiquement, une analyse discriminante linéaire (LDA), une machine à vecteurs de support (SVM) et des classifieurs à ‘seuillage manuel’ (SM) sont étudiés. Les classifieurs LDA et SVM sont entraînés sur des signaux d’ECG synthétiques, puis testés sur des signaux non-disponibles durant l’entraînement, collectés avec trois systèmes

différents: (1) un appareil d'ECG portable à 12 électrodes, (2) un appareil d'ECG ambulatoire à 2 électrodes (données collectées sur des patients souffrant d'arythmie), et (3) un système d'ECG textile à une électrode.

### 0.7.1 Stratégies de classification

Des classifieurs LDA et SVM ont été entraînés avec la boîte à outils de statistiques de MATLAB. La LDA tente de trouver une combinaison linéaire afin de séparer deux classes ou plus. Elle possède des variables indépendantes continues (normalement distribuées) et des variables dépendantes catégoriques connues sous le nom d'étiquettes de classe. Différentes classes sont basées sur différentes distributions gaussiennes pour produire des données. Durant l'étape d'entraînement, des paramètres correspondant aux distributions gaussiennes pour chaque classe sont estimés. Dans l'étape de prévision, de nouvelles données sont classifiées avec le plus petit coût de mauvaise classification. D'autre part, une SVM projette les données dans une dimension plus élevée en utilisant un noyau, afin qu'un hyperplan puisse séparer les différentes classes. Puisque les deux classifieurs ont été très utilisés dans la littérature, une description complète n'est pas incluse ici. Le lecteur intéressé est invité à consulter [49] pour plus de détails sur la LDA et [50] pour une description en profondeur des SVM. D'autre part, nous avons examiné une méthodologie de SM pour distinguer la qualité de signaux en utilisant le seuil de 0.5 trouvé pour le MS-QI. En outre, un seuil de kurtosis de  $\kappa = 5$  qui a été proposé par [28] pour distinguer entre la basse ( $\kappa < 5$ ) et la haute qualité ( $\kappa \geq 5$ ) de signaux d'ECG a été employé. Tandis qu'un tel seuil de kurtosis s'est avéré utile dans la section 0.4 pour l'ECG synthétique, des valeurs plus élevées ont été identifiées pour les signaux enregistrés.

### 0.7.2 Traits caractéristiques de référence et fusion de traits caractéristiques

Le kurtosis de l'ECG ( $\kappa$ ), une mesure statistique de la pointicité du signal, a été très utilisé comme mesure de qualité du signal ([26], [25]). Ainsi, des classifieurs LDA et SVM sont également entraînés sur des traits caractéristiques du  $\kappa$  et utilisés comme point de référence pour mesurer les avantages apportés par les traits caractéristiques de MS-QI. Afin d'étudier la complémentarité potentielle des traits caractéristiques de MS-QI et de  $\kappa$ , nous étudions les avantages de la fusion de traits caractéristiques, où des classifieurs LDA et SVM sont entraînés avec les ensembles combinés de traits caractéristiques. Les données d'ECG et de  $\kappa$  ont été normalisées pour obtenir un écart type de [0,1] avant la fusion et l'entraînement. Finalement, la stratégie de classification par SM a été examinée avec les seuils mentionnés ci-dessus pour les traits caractéristiques de MS-QI et de  $\kappa$  afin d'être comparé à la méthode d'apprentissage automatique.

### 0.7.3 Ensemble de données d’entraînement: ECG synthétique

Des signaux d’ECG synthétiques ont été employés. Pour l’entraînement, des signaux d’ECG bruités avec un RSB de -5 dB, 0 dB ou 5 dB ont été étiquetés comme “non utilisables”, tandis que les signaux d’ECG avec un RSB de 15 dB à 30 dB ont été marqués comme “utilisables”. Ce choix a permis d’inclure 600 signaux non-utilisables et 600 utilisables lors de l’entraînement du classifieur.

### 0.7.4 Ensembles de données de test 1 et 2

Un sous-ensemble des signaux d’ECG de la base de données Physionet/Computing in Cardiology 2011 Challenge [23] ont été employés. Des enregistrements d’ECG de la base de données d’arythmie de Physionet MIT-BIH ont quant à eux été employés comme deuxième ensemble de test. Finalement, des signaux d’ECG enregistrés avec le vêtement Hexoskin ont également été employés dans le deuxième ensemble de test.

### 0.7.5 Évaluation de la performance

La performance des classifieurs est mesurée via trois facteurs de qualité : l’exactitude (ACC), la sensibilité (SE) et la spécificité (SP).

$$ACC = \frac{TN + TP}{TN + TP + FN + FP} * 100\%, \quad (5)$$

$$SE = TP / (TP + FN) * 100\%, \quad (6)$$

$$SP = TN / (TN + FP) * 100\%, \quad (7)$$

où TP est le nombre de vrais positifs; FN est le nombre de faux négatifs; TN est le nombre des vrais négatifs; et FP est le nombre de faux positifs.

### 0.7.6 Résultats et discussion

Le tableau 6.1 présente les résultats d’exactitude/sensibilité/spécificité obtenus avec les trois classifieurs. Les résultats sont présentés pour l’ECG synthétique, de même que pour les ensembles de données #1 #2 non-disponibles durant l’entraînement. Les classifieurs ont été entraînés sur les ensembles de MS-QI,  $\kappa$ , et les ensembles de fusion de traits caractéristiques. Dans le cas de l’ECG synthétique, 50% des données a été employé pour l’entraînement et 50% pour l’évaluation de la performance. Dans les autres cas, l’ensemble de données d’entraînement de données d’ECG synthétique est employé en entier pour l’optimisation des hyperparamètres des classifieurs.

Comme il peut être vu, les classifieurs d'apprentissage automatique entraînés avec les traits caractéristiques de référence se comportent bien avec l'ECG synthétique, mais leur performance se dégrade rapidement lorsque des données réelles sont employées dans l'ensemble de test. Les traits caractéristiques de MS-QI, d'autre part, se sont avérés robustes à différentes modalités de mesure et ont surpassé les traits caractéristiques de  $\kappa$  par autant que  $2\times$  et  $5\times$  en termes d'exactitude et de spécificité. Ces résultats suggèrent que les traits caractéristiques de MS-QI jouent un rôle essentiel dans les applications de télésanté, qui peuvent avoir des signaux fortement bruités par des artefacts. De plus, la fusion de traits caractéristiques, malgré qu'ayant sensiblement amélioré la performance des traits caractéristiques de  $\kappa$ , n'a pas amélioré l'exactitude du classifieur de MS-QI.

Concernant le type de classifieur, la SVM s'est avérée légèrement meilleure que la LDA pour les traits caractéristiques de MS-QI. Pour les deux classifieurs, la performance est demeurée stable à travers les ensembles de données examinés. Pour le trait caractéristique de  $\kappa$ , d'autre part, le meilleur classifieur a dépendu de l'ensemble de données de test. Par exemple, pour l'ECG synthétique, la LDA s'est avérée la mieux adaptée. Pour des données enregistrées dans un contexte réel, la SVM a mené à la meilleure performance. Toutefois, avec l'ensemble de fusion de traits caractéristiques, la LDA a mené à la meilleure performance. Les résultats du SM, quant à eux, suggèrent que le trait caractéristique de MS-QI est robuste au type de données d'ECG, surpassant les traits caractéristiques de référence d'exactitude de près de deux fois. En outre, les classifieurs LDA et SVM ont menés à une performance légèrement meilleure que le SM pour les signaux synthétiques en termes d'exactitude et de spécificité. Pour l'ensemble de données de test #1, d'autre part, la méthodologie du SM s'est avérée la meilleure. Les traits caractéristiques de référence dans la méthode de SM se sont avérés sensibles au type d'ECG (voir le schéma 3.6), comme fut le cas de la classification par apprentissage automatique; la performance était ainsi bonne pour les signaux synthétiques puis a diminué avec les données enregistrées.

Afin d'examiner les avantages d'une transmission de données sensible à la qualité pour des applications de télésanté, nous employons l'ensemble de données de test #3 enregistré avec une électrode d'ECG textile. Les figures aux schémas 6.1 et 6.3 présentent le profil d'actimétrie obtenu pour un participant pendant différents niveaux d'activité: rester assis, courir et marcher, pour une méthode d'apprentissage automatique (LDA) et la méthodologie de SM, respectivement. Les valeurs d'actimétrie les plus élevées sont observées pendant la course et, dans ce cas, ont été étiquetées comme non-utilisables. Le schéma 6.2 présente un extrait de 10 secondes du signal d'ECG collecté pendant la course. Comme peut être vu, les crêtes de PQRS sont inexistantes: le signal ne donne ainsi aucune information cardiaque utile. Les niveaux d'actimétrie sont calculés à partir de l'accéléromètre triaxial et sont moyennés par fenêtres de 5 secondes.

Les profils d'actimétrie des schémas 6.1 (a) et (b) présentent aussi les étiquettes obtenues avec les classifieurs LDA entraînés avec les traits caractéristiques de MS-QI et de  $\kappa$ , respectivement. L'étiquette 0 correspond aux segments de données non-utilisables tandis que l'étiquette 1 correspond aux segments utilisables. Comme peut être vu, les classifieurs de MS-QI peuvent détecter correctement les segments utilisables et peuvent distinguer avec exactitude la course des autres activités, et pourraient donc potentiellement être employés comme détecteurs de niveau d'activité pour des applications de télésanté.

En termes d'économie de stockage, pour le profil présenté au schéma 6.1, un total de 615 secondes est illustré (123 fenêtres de 5 secondes). Le stockage de telles données exigerait  $615 \text{ s} \times 256 \text{ échantillons/seconde} \times 12 \text{ bits/échantillon} = 236 \text{ MB}$ . Avec des applications de télésanté basées sur des classifieurs de MS-QI, la capacité de stockage serait réduite à 210 secondes de données utilisables, ayant ainsi pour résultat une économie de stockage de 65 %. Les classifieurs de  $\kappa$ , d'autre part, auraient classifié 470 secondes comme utilisables, menant ainsi à une économie de seulement 25 %. Comme peut être vu, l'application de télésanté sensible à la qualité proposée ici peut mener à des gains significatifs en stockage ou en transmission, et potentiellement permettre de plus longues durées de vie de batterie, deux aspects critiques pour les applications de télésanté.

Le profil présenté au schéma 6.3 montre l'économie de stockage pour la méthode de SM. La capacité de stockage avec la configuration de MS-QI a été réduite à 255 secondes de données utilisables, ayant pour résultat une économie de stockage de 59%. D'autre part, le trait caractéristique de référence a identifié 490 secondes de données utilisables, ayant ainsi pour résultat une économie de stockage de 21%.

## 0.8 Conclusions

Les avancées concernant les applications de télémédecine d'ECG ont imposé l'utilisation de techniques de traitement de signal pour des diagnostics précis et la représentation de la santé du patient. De plus, la portabilité et la facilité d'utilisation de ces appareils en développement ont ouvert la voie à des applications au-delà des diagnostics de santé, incluant par exemple la forme physique, le contrôle de la performance et l'endurance athlétique. Plusieurs défis sont créés afin de garantir la bonne qualité de l'ECG dont nous avons besoin pour des diagnostics fiables, réduire les fausses alarmes dans les systèmes automatisés et réduire la transmission et/ou le stockage des données corrompues d'ECG. Pour prendre en compte ces problèmes, cette thèse a proposé l'utilisation d'une représentation spectro-temporelle d'ECG, appelée 'modulation spectrum', qui permet la séparation précise des composants spectraux de la modulation d'ECG des composants spectraux de bruit. Pour rendre cette séparation possible, quatre innovations dans le domaine de processus d'ECG de résistance au bruit et des applications ont été développés.

Premièrement, un index de qualité de domaine de modulation (MS-QI) a été présenté dans la section 0.4. Cet index a été testé sur des signaux d'ECG synthétiques et réalistes, celui-ci étant plus performant que deux indicateurs de qualité de référence conventionnels. Expérimentalement, il a été observé que les valeurs de MS-QI sont erronées de 0 et 1.5, où l'index peut être utilisé pour dissocier la mauvaise qualité (MS-QI proche de 0) et la bonne qualité (MS-QI proche de 1.5) du signal et aussi pour différencier les différents niveaux d'activité comme être assis, marcher et courir. D'où le MS-QI permet de détecter la mauvaise qualité des signaux d'ECG dans le but d'éviter des fausses alarmes et des diagnostics erronés sur la santé de l'utilisateur.

Dans la section 0.5, un filtrage spectro-temporel pour la détection de pic d'ECG amélioré a été proposé. En utilisant des transformations réversibles pour obtenir une représentation spectro-temporelle du signal, le filtrage peut être utilisé dans le domaine de modulation spectral et le signal amélioré peut être reconstruit. Ainsi, le signal d'ECG a été amélioré, utilisant des filtres FIR de bande passante adaptifs et centrés au lobe principal (dépend du rythme cardiaque) et plusieurs de ses harmoniques. L'algorithme proposé a été testé sur des signaux synthétiques et réalistes. Les résultats expérimentaux ont montré que l'algorithme proposé est plus performant qu'un algorithme pointu d'amélioration de vaguelette dans des termes d'amélioration de RSB, de pourcentage d'erreur de rythme cardiaque, de kurtosis et de mesure d'HRV. Ces résultats obtenus démontrent que la technique proposée convient parfaitement pour les appareils d'ECG embarqués à moindre coût qui peuvent être grandement contaminés par des artefacts en mouvement et peut être utilisée pour améliorer la qualité des moniteurs d'ECG embarqués, même dans des conditions extrêmes, jouant ainsi un rôle clé dans l'entraînement et le contrôle des performances de pointe athlétique.

Un nouvel index HRV nommé domaine de modulation HRV (MD-HRV) fut proposé dans la section 0.6. L'index a montré sa résistance au bruit, même dans des scénarios extrêmes. Les mesures MD-HRV de la déviation standard des composants spectraux de modulation par bordure correspondent au rythme cardiaque. Elles ont été testées en utilisant des signaux bruyants synthétiques et enregistrés et comparées aux six indicateurs HRV de référence calculées dans le domaine de temps, le domaine de fréquence et les méthodes non-linéaires des signaux purs. L'indicateur proposé fut plus performant que les indicateurs de référence calculés depuis les signaux bruyants sans aucune amélioration antérieure d'ECG, montrant ainsi son adaptation à des conditions de bruit extrême avec des appareils d'ECG portables.

Enfin, la section 0.7 présente une application pour le MS-QI proposé dans la section 0.4. Un bilan en ligne de qualité d'ECG pour les applications de télémédecine a été proposé, où le MS-QI fut utilisé en tant que caractéristique pour deux classificateurs (LDA et SVM). Ces classificateurs ont été testés pour différencier les données 'utilisables' et 'non-utilisables' pour l'importance de la qualité dans les applications, tout comme pour représenter les différents états d'activité (par exemple être assis, marcher et courir) pour les applications d'activités

importantes. La caractéristique du MS-QI proposé a été comparée au kurtosis d'ECG utilisé majoritairement, utilisant des signaux d'ECG synthétiques et réels. Les résultats des expériences avec les deux classificateurs ont montré que le MS-QI est plus performant que le kurtosis en tant que configuration caractéristique fusionnée. Des gains de 65% ont pu être observés dans les enregistrements en ignorant les segments non-utilisables de l'ECG perturbé de façon sonore. Ces découvertes ont été comparées à un 'seuil manuel', utilisant le seuil de 0.5 trouvé dans la section 0.4. Des enregistrements stockés de 59% ont été trouvés, concluant ainsi que la méthode d'apprentissage de la machine est la plus performante.



# Chapter 1

## Introduction

Recent statistics have placed heart disease as the leading cause of death in the United States, representing 1 in every 4 deaths [1]. Worldwide, the statistics are similar and 30% of all global deaths are related to cardiovascular diseases [2]. According to the Heart and Stroke Foundation, the electrocardiogram (ECG) is an available powerful tool capable of helping clinicians to detect, diagnose, and monitor certain heart diseases. Representative applications can include: detection of abnormal heart rhythms (arrhythmias), ongoing heart attacks, coronary artery blockage, areas of damaged heart muscle from a prior heart attack, enlargement of the heart, inflammation of the sac surrounding the heart (pericarditis), electrolyte imbalances, lung diseases, as well as monitor the effectiveness of certain heart medications or a pacemaker, or even rule out hidden heart diseases in patients about to undergo surgery [3]. Hence, burgeoning telehealth applications are emerging where ECG is the most common measured signal not only to detect cardiovascular diseases but also activities, stress levels [4], emotions, and athlete endurance [5], to name a few. Recent market projections have forecasted the ECG monitoring and cardiac rhythm management market to grow

to nearly \$27 billion by 2020 [6] due to e.g., increases in the number of cardiovascular disease cases [7], new healthcare [8] and disease management applications [9], as well as the burgeoning sports and quantified-self markets [51].

Telehealth applications have been growing in the last few years in both medical and non-medical fields. Medical applications comprise healthcare solutions for e.g., aging and/or diseased populations in which medical personnel (doctors, clinicians, nurses, and physicians) and patients are involved. These applications are focused on the continuous measurement of a user's biological signals, such that caregivers or medical personnel can monitor, diagnose, and track a patient's health. Non-medical applications, in turn, have normal everyday users as the target and are deployed in entertainment, security, fitness monitoring applications, and self-quantification purposes. Some leading telehealth applications, including ECG as a representative vital sign, include:

- **Remote patient monitoring:** This application consists of monitoring a patient's vital signs, commonly from a hospital or healthcare setting, to provide medical personnel with advice on the patient's health condition. Traditional patient monitoring devices include ECG to monitor heart conditions. The majority of the applications use intelligent signal processing to detect pathological patterns (e.g., arrhythmia), and rely on event-based transmission to reduce power consumption. For example, multi-lead ECG data is only transmitted if an arrhythmia is detected, or multimodal signals are sent continuously if a fall is detected [52]. Also, severe heart failure is detected through a platform to enhance the efficiency of home monitoring using data mining [53].
- **Patient rehabilitation:** Physical exercises and activities performed by the patient are monitored in order to avoid improper exercises, update exercise complexity, monitor recovery,

compare different treatment protocols, and to enable telerehabilitation. ECG monitoring during rehabilitation can help avoid excessive exercise in patients with critical heart conditions through physical activity recognition algorithms [54].

- **Biofeedback:** According to the Association for Applied Psychophysiology and Biofeedback, biofeedback is the process of using precise instruments to measure physiological activity, and “feed” this biological information “back” to the user, thus allowing the individual to learn how to better control or change this physiological activity in order to improve health and performance. Biofeedback has been used since the early 1960’s and has been shown to be useful in controlling emotional states and involuntary body functions, such as migraine and blood pressure, to name a few. Biofeedback devices can include those that monitor breathing, heart function, muscle activity, and brainwaves. Since the heart rate can reflect workload, stress, drowsiness, and lack of concentration, a system to indicate heart rate using music therapy can be used for patient relaxation [55].
- **Assisted living:** Assisted living facilities have emerged as an alternative housing facility for people with disabilities (and elderly) who are not considered “independent” but do not need around-the-clock medical care, as in nursing or retirement homes. As such, assisted living promotes independence and dignity (aging in place) whilst reducing medical costs. To this end, physiological activity, including movement and heart rate, can be monitored at any time helping to improve people’s quality of life [56].
- **Biometrics:** Not only personal authentication is a topic widely discussed within medical applications (e.g., encrypt patient data for privacy purposes), but also for non-medical purposes, where biometrics are used for banking, accessing secure information/services, or even unlocking a smart phone. Biosignals such as the ECG, electroencephalogram, and electroder-

mal activity provide unique biometric signatures which are hard (if not impossible) to steal, copy, forget, or lose. One such system is the one developed by the United States of America Department of Homeland Security termed FAST (Future Attribute Screening Technology), which uses biosignals such as heart and respiration rate, facial skin temperature, voice pitch, pupil dilatation, and body movements. Also, a mechanism for person identification using ECG signals can be used [57] for abnormal cardiac conditions in network environments.

- **Fitness, performance, and wellness monitoring:** As reported by ABI Research, by 2017 60% of telehealth applications will be geared towards fitness, performance, and wellness tracking. This comes as no surprise as sleep, stress, and obesity are three global public health problems thus boosting the quantified self (QS) movement in the last few years (recent statistics show over 110 QS groups spread over 88 cities in 31 countries). Moreover, performance and fitness monitoring tools allow athletes and military personnel to optimize training protocols, thus improving endurance and outcomes and putting them in front of the competition or enemy, respectively. For athletic applications, coaches can see the exact status of every athlete in the field and detect injuries. To this end, wearable sensors are employed, being ECG one of the most common signals to measure [58].

At present, there is a high interest in applications for self-quantification purposes. People are more interested in improving their quality of life wearing sensors (i.e., wearables) that can give information about their health status. With the emergence of these applications, wireless ECG monitors have proliferated not only within the clinical realm (e.g., [10]), but also within the sports and consumer markets (e.g., [5, 11, 12]). This witnessed increase in “quantified-self” applications has been driven mostly by recent advances in innovative, lower-cost wireless ECG monitors (e.g., [13]), smart shirts and bras (e.g., OMSignal), wireless body area networks (WBANs), and smartwatches.

A number of devices have reached the market, such as the Hexoskin garment (Carre Technologies, Canada), nECG (Nuubo, Spain), BioHarness (Zephyr, USA), Fitbit (USA), Jawbone's UP wristband (USA), Biopeak's Biofusion chestband (Canada), and Corbelt (Corscience, Germany), to name a few.

Therefore, the use of wearable sensors in telehealth applications has witnessed a steep growth in the last few years. Experts named 2014 as "Year of wearables" as the wearable fitness industry was valued at \$700 million that year [6]. Furthermore, according to "Statista", the global wearable market will reach 19 billion US dollars in 2018 [14]. However, while such devices have opened doors to emerging telehealth applications, several challenges have been created that still need to be addressed, the most pressing being the quality of the collected ECG signals. Low-cost ECG wearables sensors are extremely sensitive to different types of artifacts, including respiration, body movement, and muscle contractions, thus hampering heart rate (HR), and heart rate variability (HRV) analysis [15] and requiring noise-robust techniques. These shortcomings are discussed in the following section.

## 1.1 Challenges with Noisy ECG Signals

Commonly, ECG signals are contaminated by several artifact types, including baseline drifts due to respiration, power line interference, body movement, and muscle contractions [15]. With lower-cost sensors, increased sensitivity to such artifacts occurs, particularly due to movement (as the users are now mobile), electrode contact noise (when sensor loses contact with skin during movement), as well as missing data due to wireless transmission losses [59], thus hampering signal quality. As

such, poor signal quality can have severe detrimental effects, such as erroneous HR monitoring or heart disease diagnosis [28], or HRV calculations. Such artifacts significantly limit the usefulness of automated systems aimed at measuring HRV, a measure commonly used to monitor, for example, stress levels [4] and athlete endurance [5]. For this reason, in clinical applications medical personnel often rely on visual inspection of the ECG [28].

With advances in telehealth applications and devices, however, clinicians are now being provided with hours of collected data from numerous modalities. To process such “big data”, automated decision support systems are required. In order for reliable systems to be developed, online monitoring of ECG data quality is paramount, so that intelligent signal processing can be used [9, 60, 61]. In fact, a reliable ECG quality index can also be used to train inexperienced staff [62]. Also, reliable HR and HRV calculations are needed for a number of applications, including but not limited to athlete endurance monitoring [5], stress detection [4], heart failure detection [63], and sleep disorders monitoring [64]. Hence, ECG quality is an important metric that has been assessed in recent Physionet challenges. For example, the Physionet/Computing in Cardiology Challenge 2011 was conducted to improve the quality of ECGs collected using mobile phones [23]. The Challenge aimed to find efficient real-time algorithms within a mobile phone in order to acquire useful ECG information. Thus, the designed software indicates if the ECG is adequate for analysis or if a new recording is required. Physionet/Computing in Cardiology Challenge 2014, in turn, explored robust methods for locating heart beats in continuous long-term recordings not only in ECG signals but also in other physiological signals [31]. The motivation was focused on ECG missing information due to bad-quality recordings. Thus, other physiological signals such as continuous blood pressure, and photoplethysmograms were used to assist with ECG peak detection (and consequently heart rate and heart rate variability measurement).

As can be seen, with the burgeoning of telehealth and quantified-self monitoring applications using wearable ECG devices, the need for accurate ECG quality monitoring tools, enhancement algorithms, as well as noise-robust metrics and/or applications are needed. This is where this thesis comes in. As detailed in the following section, this thesis proposes innovative solutions to tackle the following four critical problems.

## 1.2 Thesis Contributions

The aim of this thesis is four-fold: (1) analyze noisy ECG signals for emerging telehealth applications using the modulation spectrum representation for quality assessment, (2) ECG enhancement, (3) accurate heart rate variability analysis in extremely noisy scenarios, and (4) incorporate these findings into a noise-robust application. The key contributions are:

1. The proposal of a new ECG quality index termed modulation spectral based quality index (MS-QI). To this end, the ECG modulation spectral representation that allows separating ECG spectral components from ECG artifacts was used. The index is similar to the signal-to-noise (SNR) ratio since it relates energy of the ECG spectral components to noise spectral components. The MS-QI values showed to be typically between 0 and 1.5 with higher values corresponding to improved quality. The index can be used as a quality-aware metric as well as an activity level detector (e.g., sitting, walking, and running). It can be useful not only for remote telehealth applications but also for fitness/training where the ECG is highly contaminated with motion artifacts. The results of this contribution appeared in publications #2 and #3 listed in Section 1.3.

2. A new ECG enhancement algorithm based on spectro-temporal filtering is proposed. The algorithm improves peak detection (i.e., heart rate detection), HRV analysis, quality (e.g., kurtosis), and SNR ratio since ECG spectral components can be separated from noise in the modulation spectrum domain. For this purpose, a bank of adaptive linear-phase finite impulse response (FIR) bandpass modulation filters were used to extract the ECG modulation spectral components. By using invertible transforms to compute the modulation spectral representation, filtering could be performed in this domain and the enhanced ECG signal then reconstructed in the time-domain. The method is suitable for lower-cost wearable ECG devices that can be highly contaminated by movement artifacts. Publications resulting from this contribution include #3, #4, and #5 listed in Section 1.3.
3. A new noise-robust heart rate variability index, named modulation domain HRV (MD-HRV), is proposed. The heart rate can be estimated in the modulation domain by quantifying the rate-of-change of the ECG spectral components. Hence, the heart rate can be extracted even in very noisy scenarios, thus eliminating the need for applying any ECG enhancement algorithm. As a result, the MD-HRV index is calculated as the standard deviation of the per-frame central modulation frequencies, which correspond to the heart rate. The proposed index can be suitable in portable cardiac monitoring applications where movement can hamper reliable ECG recordings. This contribution is described in publications #6 and #7 listed in Section 1.3.
4. An online ECG quality assessment using the proposed MS-QI for quality-aware applications is presented. Usable and unusable ECG signals were classified to obtain savings in storage space for telehealth applications. Also, the classification results can be used for activity-aware applications to distinguish among different activity levels (e.g., sitting, walking, and running). This contribution appears in publication #8 listed in Section 1.3.

### 1.3 Publications and Patents

1. D. Tobón, T. Falk, and M. Maier, “Context Awareness in WBANs: A Survey on Medical and Non-Medical Applications,” *IEEE Wireless Communications*, vol. 20, no. 4, pp. 30–37, 2013.
2. D. Tobón, T. Falk, and M. Maier, “MS-QI: A Modulation Spectrum-Based ECG Quality Index for Telehealth Applications,” *IEEE Transactions on Biomedical Engineering*, vol. 63, no. 8, pp. 1613–1622, 2016.
3. T. Falk, D. Vallejo, M. Maier, Method and System for Evaluating a Noise Level of a Biosignal, US patent application number: 61/941,842, Filed on February 19, 2014. Intl PCT filed on February 17, 2015. Canada: 2,937,693; approved July 22, 2016.
4. D. Tobón and T. Falk, “Adaptive Modulation Spectral Filtering for Improved Electrocardiogram Quality Enhancement,” in *Computing in Cardiology Conference (CinC)*, vol. 43, pp. 441-444, 2016.
5. D. Tobón and T. Falk, “Adaptive Spectro-Temporal Filtering for Electrocardiogram Signal Enhancement,” *IEEE Journal of Biomedical and Health Informatics*, 2016, accepted with minor modifications.
6. D. Tobón, S. Jayaraman, and T. Falk, “Spectro-Temporal Electrocardiogram Analysis for Noise-Robust Heart Rate Variability Measurement,” *IEEE Transactions on Biomedical Engineering*, 2016, submitted, under review.
7. T. Falk, D. Tobón, and S. Jayaraman, “Spectro-temporal electrocardiogram analysis for noise-robust heart rate variability measurement.” Provisional patent application in preparation, October 2016.

8. D. Tobón and T. Falk, “Online ECG Quality Assessment for Context-Aware Wireless Body Area Networks,” in 2015 IEEE 28th Canadian Conference on Electrical and Computer Engineering (CCECE), pp. 587–592, 2015.

## 1.4 Thesis Organization

This thesis was compiled based on the collection of six publications (#1, #2, #4, #5, #6, #8) and two patent submissions (#3 and #7) with minor modifications, all of them listed in Section 1.3. In Chapter 1, the importance of noisy ECG analysis is highlighted. Chapter 2 gives an overview of the ECG signal, conventional ECG signal processing techniques and their current challenges and highlights the ECG modulation spectral representation (spectro-temporal representation) that is used in subsequent chapters. Chapter 3 presents a new ECG quality index (MS-QI) using the so-called modulation spectrogram. Chapter 4 addresses an enhancement ECG algorithm using spectro-temporal filtering for improved peak detection in noisy ECGs. Chapter 5 introduces a noise-robust HRV index using spectro-temporal ECG analysis. Chapter 6 explores a quality-aware application using the proposed MS-QI. Finally, Chapter 7 draws final conclusions and outlines future research directions.

## Chapter 2

# Electrocardiogram Signal Processing

### 2.1 The Electrocardiogram Signal

The ECG signal is generated by a series of electrical changes in the human heart. Within the cardiac muscle, also known as myocardium, electrical discharges take place from specific nodes spreading through the myocardium. Thus, coordinated contractions are stimulated to pump blood to the lungs for oxygenation and oxygenated blood through the body to peripheral organs. Figure 2.1 illustrates the two main pumps in the heart. Each pump has one atrium and one ventricle. The deoxygenated blood from the body goes into the right atrium which pumps it to the right ventricle. Then, that ventricle sends the deoxygenated blood to the lungs to be oxygenated. The blood, now oxygenated, arrives again to the heart at the left atrium through the pulmonary veins. Afterwards, the left atrium pumps the blood to the left ventricle to pump it through the body. All this process is part of one cardiac cycle. The cycle includes two main phases known as diastole and systole. Diastole is

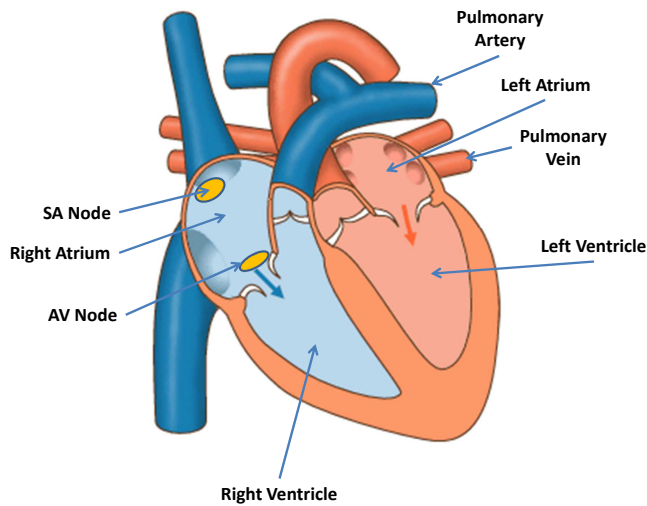


**Figure 2.1 – Electrical conduction system of the heart. Two main pumps are illustrated with their atria and ventricles. SA corresponds to sinus node and AV to atrioventricular node.**

the blood filling phase where ventricles are filling and relaxing, whilst atria are relaxing. Systole, in turn, corresponds to heart contractions in order to pump the blood to either the body or the lungs. Hence, the cycle has two electrical phases termed depolarization (activation) and repolarization (recovery).

The cardiac cycle initiates due to the electrical stimulation (self-excitation) of the sinus (SA) node. That node generates an electrical impulse spontaneously, which is then conducted to the atrioventricular (AV) node. The AV node connects the electrical impulse from the atria to the ventricles (that conduction lasts about 100 ms). Afterwards, there is a refractory period of at least 200 ms and then the heart goes to its resting electrical potential. As a result, the cardiac cycle is ready to start again [16].

### 2.1.1 ECG Waveform

The ECG is a signal that measures the cardiac activity of the heart generated by the electrical impulse of the SA node, which propagates across the heart through the cardiac cells. Hence, the electrical impulse can be detected on the surface of the skin resulting in the ECG measurement. A normal ECG segment shows repolarization and depolarization effects in different parts of the heart.

Figure 2.2 depicts a normal ECG segment. The segment corresponds to one cardiac cycle or heartbeat. The cycle starts by the electrical impulse generated by the SA node, which propagates through the atria. Consequently, the atria contract and depolarize resulting in the ‘P-wave’. The ‘PQ or PR segment’ (iso-electric segment) is the result of a delay of less than 100 ms after the electrical impulse reaches the AV node. This delay gives time to the atria to contract before the depolarization of ventricles. Afterwards, a contraction generated when the impulse reaches the ventricles is reflected in the ‘QRS complex’ (ventricular depolarization), where the atria repolarization is hidden in it. Then, the ‘ST segment’ emerges when the entire ventricles are depolarized, depolarization that can last up to 350 ms. Lastly, a repolarization wave called ‘T-wave’ appears when the ventricles relax.

### 2.1.2 Recorded ECG Signal

The electrical impulse generated by the SA node changes its magnitude and direction over time. Consequently, across the surface of the body, a vector can measure the electrical potential. Thus, the type of ECG measurement will depend on the position of the skin electrodes with respect to the electrical impulse propagation, named cardiac vector. Hence, one pair of electrodes (the voltage difference between them is known as a lead) shows ECG information depending on the cardiac vector

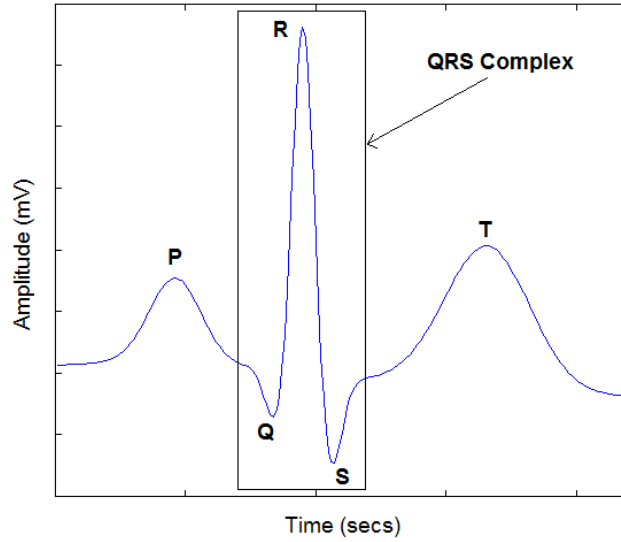


Figure 2.2 – Normal ECG waveform that shows one cardiac cycle or heartbeat and the polarization and repolarization waves.

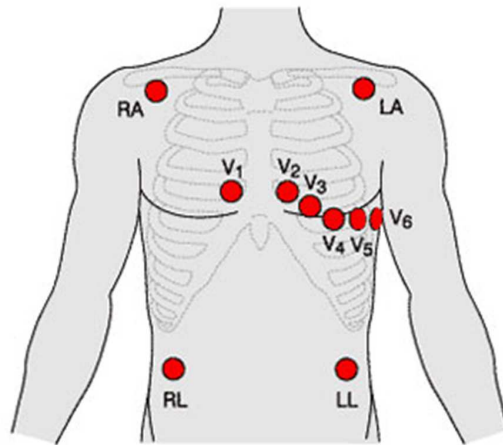


Figure 2.3 – Ten-electrode location for the 12-lead standard ECG configuration.

changes with respect to one particular axis [65]. A standard 12-lead ECG configuration is employed to fully represent the cardiac activity. Ten electrodes are used in this configuration: four located on the limbs and six on the chest, as depicted by Figure 2.3. As such, the 12-lead configuration is defined as follows [66]:

- **Leads I, II, and III:** The electrodes are located in left arm (LA), right arm (RA), and left leg (LL) in a configuration called Einthoven's triangle with the heart in the center. Each lead

is derived using the three electrodes as seen in the equations (2.1)-(2.3), respectively:

$$I = LA - RA, \quad (2.1)$$

$$II = LL - RA, \quad (2.2)$$

$$III = LL - LA, \quad (2.3)$$

- **Leads aVF, aVR, and aVL:** These leads are derived from the same three electrodes as in leads I, II, and III as shown in equations (2.4)-(2.6), respectively:

$$aVF = LL - \frac{1}{2}(LA + RA), \quad (2.4)$$

$$aVR = RA - \frac{1}{2}(LA + LL), \quad (2.5)$$

$$aVL = LA - \frac{1}{2}(RA + LL), \quad (2.6)$$

- **Leads V1 to V6:** These leads are defined as the difference between the potential of the electrodes located on the chest and the Wilson's central terminal (i.e., average potential RA, LA, and LL).

Index (i)	P	Q	R	S	T
Time (secs)	-0.2	-0.05	0	0.05	0.3
$\theta_i$ (radians)	$-\frac{1}{3}\pi$	$-\frac{1}{12}\pi$	0	$\frac{1}{12}\pi$	$\frac{1}{2}\pi$
$a_i$	1.2	-5.0	30.0	-7.5	0.75
$b_i$	0.25	0.1	0.1	0.1	0.4

Table 2.1 – ECG model parameters for the ECG dynamic model.

### 2.1.3 Synthetized ECG Signal

Synthetized ECG signals employed in this thesis were generated using the *ecgsyn* Matlab function available in Physionet [21]. The function uses a dynamic model to generate the realistic ECG waveform [67] and allows for several user-settable parameters, such as mean heart rate, sampling frequency, waveform morphology (i.e., P, Q, R, S, and T timing, amplitude, and duration), standard deviation of the RR interval (R-peak to R-peak interval), and the low-frequency (LF) to high-frequency (HF) ratio. Also, the model implements respiratory sinus arrhythmia at the high frequencies and Mayer waves at the low frequencies.

The model generates a tridimensional trajectory with coordinates  $x, y, z$  as depicted in Figure 2.4. A trajectory movement around the  $xy$  plane (unit circle) reflects the quasi-periodicity of the ECG signal, which represents one RR interval. A trajectory movement along  $z$  axis represents interbeat variation. In addition, P, Q, R, S, and T peaks have fixed angles and times around the unit circle in  $xy$  plane as shown in Table 2.1. Those fixed angles and times were chosen from a typical subject with normal ECG and are relative to the position of the R-peak. As a result, when the trajectory is approaching the fixed angles, it is pushed upwards or downwards from the unit circle. Consequently, when the trajectory is moving away from that circle, it is pulled back towards it.

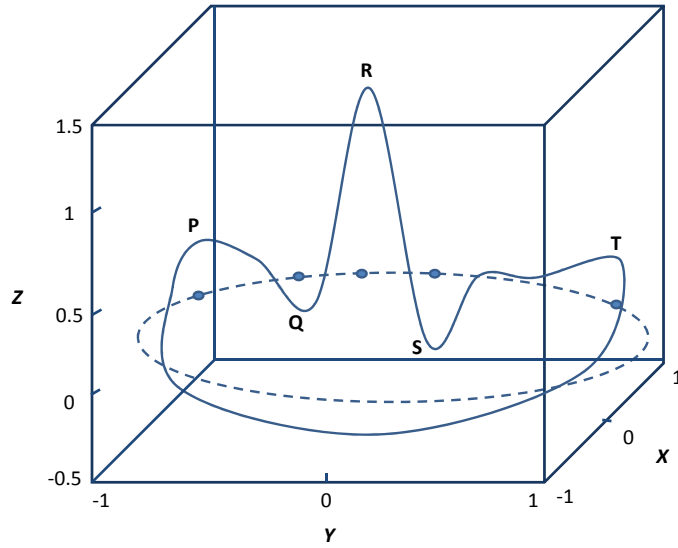


Figure 2.4 – Tridimensional trajectory generated by the dynamic model proposed in [67]. The dashed lines represent the unit circle and the small blue points the positions of P, Q, R, S, and T events.

The dynamical model is given by three ordinary differential equations as follows,

$$\dot{x} = \alpha x - wy, \quad (2.7)$$

$$\dot{y} = \alpha y - wx, \quad (2.8)$$

$$\dot{z} = - \sum_{i \in \{P, Q, R, S, T\}} a_i \Delta \theta_i \exp\left(-\frac{\Delta \theta_i^2}{2b_i^2}\right) - (z - z_o), \quad (2.9)$$

where,

$$\alpha = 1 - \sqrt{x^2 + y^2},$$

$$\Delta \theta_i = (\theta - \theta_i) \bmod 2\pi,$$

$$\theta = \text{atan2}(y, x),$$

$w$  is the angular velocity of the trajectory around the unit circle,

$z_o(t) = A\sin(2\pi f_2 t)$  (baseline wander with a respiratory frequency  $f_2$  and  $A = 0.15mV$ ).

The three ordinary differential equations were integrated numerically using fourth-order Runge-Kutta method [68] with a time step of  $\Delta t = 1/f_s$  ( $f_s$  corresponds to the sampling frequency). On the other hand, respiratory sinus arrhythmia (RSA) and Mayer waves (i.e., cyclic changes in arterial blood pressure that is reflected in the ECG) were incorporated in the model in the power spectrum of the RR intervals.

After generating clean synthetic ECG signals using the dynamic model at different heart rates, the signals were corrupted by several noise sources at known SNR levels as depicted in Figure 2.5. The noise sources were combined, scaled, and added to the clean synthetic signals. The heart rate range and the SNR levels studied in this thesis are described in the subsequent chapters. According to [69], three types of artifacts are commonly present in ECG signals: environmental, experimental, and physiological. The first type can be originated from the main powerline interference, electromagnetic interference, and from the circuit components themselves. The second type is due to undesired changes in the experimental setup, such as human error or user motion. Such artifacts are difficult to remove as they overlap in time and frequency with the desired ECG signal. Lastly, physiological artifacts are those generated by other physiological processes in the body, such as muscle artifacts or baseline wander due to breathing modulation.

For the experiments described herein, three half-hour recordings of typical noise in ambulatory ECG were used to corrupt the clean synthetic ECG signals. These noise sources were taken from the widely-used MIT-BIH Noise Stress Test [20, 21] and comprised recorded electrode motion artifacts (record ‘em’), baseline wander noise (record ‘bw’), and muscle artifacts (record ‘ma’). The noise

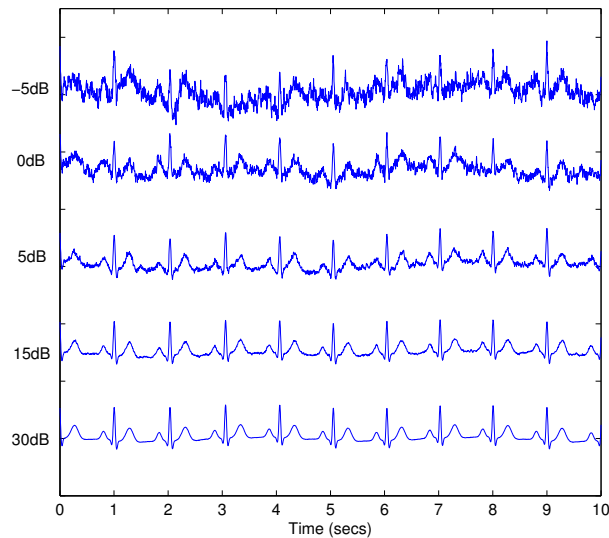


Figure 2.5 – Ten-second excerpts from the noisy synthetic ECG signals.

recordings were taken from active volunteers, ECG recorders, leads, and electrodes located on the limbs. Two other types of noise sources were also added, namely pink or  $1/f$  noise (commonly used to model observation noise) and brownian or  $1/f^2$  noise (used to model electrode movement artifacts) [15]. Electrode artifacts are considered to be the most problematic noise to suppress due to their characteristics, thus are the main focus of this thesis. Powerline interference (mains noise) is not investigated here as notch filters have been extensively used in the literature for this purpose.

## 2.2 Conventional ECG Signal Analysis Methods

### 2.2.1 Heart Rate Variability

Typically, heart rate variability (HRV) analysis has been used as a viable technique for non-invasive assessment of the automatic nervous system (ANS), both in healthy individuals and in patients with

cardiac disorders (e.g., [70–75]). The ANS is comprised of the sympathetic and parasympathetic nervous systems, where the former prepares the body for action and maintains homeostasis, whilst the latter stimulates the body for relaxation. In response to such ANS activity, heartbeat intervals fluctuate causing a change in the variability of the heart rhythm. This variability has been shown to be related to cardiac autonomic function regulation [76, 77], as well as to stress, anxiety, diabetes, hypertension, fatigue, and drowsiness [78, 79], to name a few factors. Over the years, several indices have been proposed to measure HRV, including linear (time domain, spectral domain) and non-linear methods (e.g., geometric method, entropy, and fractal dynamic methods), as described next.

### **Time Domain Metrics**

Time domain methods typically evaluate the variability in ECG peak-to-peak intervals (also known as ‘RR’ periods) and in the so-called normal-to-normal (NN) intervals between adjacent QRS complexes resulting from sinus node depolarizations [80]. They are statistics calculated directly from the inter-beat interval (IBI) series without resampling. The most common metrics include:

- **Mean IBI:** Average of the all NN intervals series.
- **sdHR:** Standard deviation of the measured heart rate.
- **SDNN:** Standard deviation of all NN intervals series.
- **SDANN:** Mean IBI of each segment (usually 5-minute length) is used to calculate the standard deviation of all means usually in a 24 hour recording.
- **SDNNi:** Standard deviation of each IBI segment (usually 5-minute length) is used to calculate the mean of all standard deviations usually in a 24 hour recording.

- **RMSSD:** Root mean square of differences between adjacent IBI series.
- **NNx:** Number of differences between adjacent IBI series that are greater than x milliseconds.
- **pNNx:** Percentage of differences between adjacent IBI series that are greater than x milliseconds.

### Frequency Domain Metrics

Frequency domain methods apply either auto-regressive models or Welch periodogram analysis on the RR interval series in different frequency bands. The power spectral density (PSD) is calculated within the IBI interval series to quantify changes in the heart rate and gives information about the amount of power of frequencies contributing to the IBI series. Hence, the amount of power is computed by integrating the PSD between the band frequency limits. The most common frequency-domain metrics are listed below:

- **Ultra low frequency (ULF):** Total spectral power of all IBI series between 0.0001 and 0.003 Hz.
- **Very low frequency (VLF):** Total spectral power of all IBI series between 0.003 and 0.04 Hz.
- **Low frequency (LF):** Total spectral power of all IBI series between 0.04 and 0.15 Hz.
- **High frequency (HF):** Total spectral power of all IBI series between 0.15 and 0.4 Hz.
- **LF/HF:** Low frequency to high frequency ratio which is the so called sympatho-vagal balance.

- **Total power:** Total spectral power of all IBI series in ULF, VLF, LF, and HF band frequencies.

## Nonlinear Metrics

Non-linear methods have been proposed and shown to better characterize the complex dynamics of the cardiac autonomic system [81]. As such, geometric methods have been used to convert the RR intervals into a geometric form (e.g., triangle or ellipse), thus representing different classes of HRV [82, 83]. Other non-linear measures include indices of the signal “randomness” (entropy), with measures such as approximate, sample, multiscale, fuzzy, and fuzzy measure entropy [84], as well as statistical properties of fractals [85–87]. A complete description of such HRV indices is beyond the scope of this dissertation and the interested reader is referred to [80] and the references therein for more complete details. Lastly, non-linear Poincaré plots are used to quantify self-similarity assuming that each inter-beat interval (IBI) is influenced by the previous one [30]. Thus, an ellipse is fitted with a long axis representing the line of identity as well as a perpendicular axis to it. If the IBIs are longer than the previous ones, the points will be located above the line of identity and below for the opposite case. Consequently, the so-called SD2 parameter represents the standard deviation along the line of identity and the SD1 parameter the standard deviation over the perpendicular line. Hence, SD1 indicates the standard deviation of instantaneous beat-to-beat (i.e., short term variability) and SD2 of continuous or long-term variability [43].

### 2.2.2 QRS Detection Algorithm

The IBI or RR times are extracted from the ECG signal in order to perform the HRV analysis. To this end, the QRS detector algorithm implemented by Pan-Tompkins [36] is commonly employed to obtain the R peak locations to further calculate the RR times. The Pan-Tompkins algorithm processing steps can be visualized in the block diagram depicted by Figure 2.6 [88] and corresponds to two main stages: pre-processing and decision making. Each stage comprises the following steps:

- **Preprocessing**

- A low pass filter followed by a high pass filter (band-pass filter between 5 and 15 Hz) are implemented in order to eliminate muscle and baseline wander noise.
- A derivative filter is applied to the filtered signal to highlight the QRS complex.
- The signal is squared to accentuate the R-peaks (higher frequencies) and make all the ECG data positive.
- A moving window is used to integrate the squared signal in order to get rid of noise as well as to see the energy distribution, which helps for the fiducial point localization (onset of the PQRST waves).

- **Decision rule**

- In order to localize the QRS complex (rising edge of the integrated waveform), a weighting is applied to the maxima values.
- Two threshold values, one for the signal and other for the noise, are continuously adapted according to the ECG signal quality to identify QRS complexes from noise peaks.

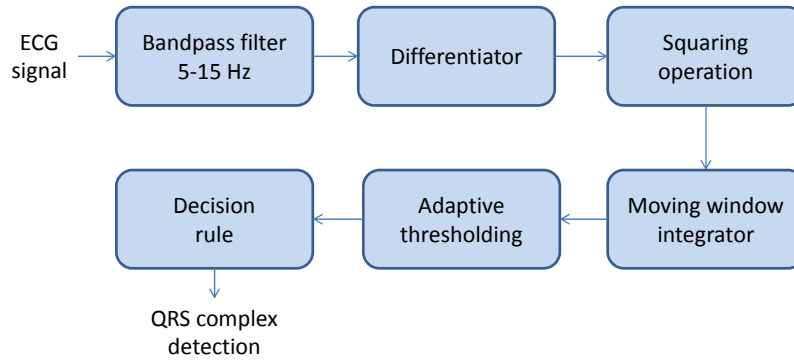


Figure 2.6 – Block diagram of the Pan-Tompkins algorithm steps to detect QRS complexes [88].

- Missed QRS complexes are searched when a long period expires without any QRS detection. To this end, a search back is performed assuming that a missed QRS occurs at the highest peak between the two thresholds.
- Multiple QRS detections are eliminated within a refractory period (200 ms) to reduce false positives, since a QRS complex does not occur within that period after a previous one.
- A T wave discrimination is needed to distinguish between an actual QRS complex or an abnormal T wave. Thus, if the slope at the detected location is less than one half of the previous QRS complex, the wave corresponds to a T wave, otherwise it corresponds to a QRS complex.

### 2.2.3 Heart Rate Variability Analysis Software (HRVAS)

The open-source heart rate variability analysis software (HRVAS) [30], developed in Matlab, was used in this thesis to calculate the HRV metrics in time domain, frequency domain, and nonlinear analysis (Poincaré). The software provides a graphical user interface (GUI), batch processing, and

allows exporting HRV results into a Microsoft excel file. As input formats, HRVAS can read ASCII files such as IBI files (.ibi) and text files (.txt). The files must have one or two columns. In the case of one column, it must correspond to IBI/RR values in unit of seconds. Two columns, in turn, must represent time in seconds and IBI/RR values in units of seconds for the first and second column, respectively. For the HRV calculations herein, text files with the RR information in seconds are used as an input file. The RR information was extracted using the Pan-Tompkins algorithm described in the previous section.

Figure 2.7 shows a flowchart of the HRVAS software with the process to compute the HRV metrics in time domain, frequency domain, time-frequency domain, and nonlinear. The software performs preprocessing of the IBI time series before HRV analysis consisting of ectopic interval detection, ectopic interval correction, and IBI detrending. Ectopic interval detection identifies abnormal IBI intervals due to either false or missed beats. To detect them, a percentage filter is used to identify interval changes in regard to the previous one that are bigger than a defined percentage (often 20%). Then, the ectopic interval correction is performed by simply removing the ectopic intervals detected. Afterwards, IBI detrending using wavelet packets is applied to remove low frequency trends. The signal is decomposed using wavelet packet transform (DWPT) where both high frequency and low frequency components are splitted into finer components. Thus, wavelet coefficients corresponding to frequency components of the undesired trend are set to zero. Afterwards, an inverse DWPT is employed to reconstruct a detrended IBI series [89]. Finally, a resampling is applied due to frequency metrics calculations (Fourier-based power spectrum) require time series regularly sampled in time in order to avoid harmonics in the power spectrum. Herein, the resampling method used was linear interpolation. Lastly, HRV metrics are computed from the processed IBI intervals.

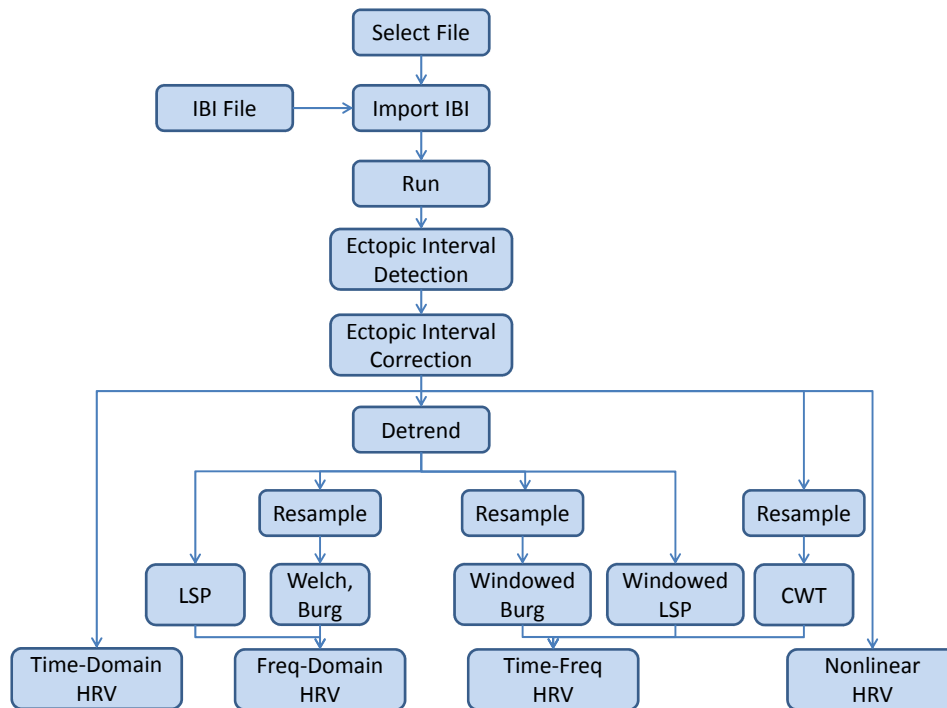


Figure 2.7 – Flowchart of the HRV analysis employed in the HRVAS software [30]. LSP: Lomb-Scargle periodogram, Welch: Welch periodogram, Burg: Burg periodogram, and CWT: continuous wavelet transform.

## 2.3 ECG Signal Enhancement

Several ECG enhancement techniques have been explored due to the increase of telehealth applications in recent years. Such techniques are necessary to remove noise from the ECG signal in order to avoid false alarms, incorrect readings, erroneous diagnoses, and increase application performance. To this end, researchers have explored different methods such as empirical mode decomposition (EMD), wavelet transform, artificial neural networks, fuzzy logic, and filtering as discussed next.

The EMD method consists of decomposing the ECG signal into intrinsic mode functions (IMFs) derived adaptively from the data. The algorithm consists of several steps: i) identify maximum and minimum points of the signal, ii) generate envelopes for the lower and upper points, iii) calculate

the envelope mean function, iv) compute the difference between the signal and the mean function. This difference is the first IMF if the numbers of extreme and zero crossing points are the same or different for at most one, as well as if the mean value of the envelope for local minima and local maxima is zero at any point. If these conditions are not satisfied, the difference signal calculated in step iv is used to repeat the above steps from step i, v) the residual is calculated using the noisy signal and the IMF computed, vi) the previous steps are repeated in order to find the other IMFs. The process is stopped when the residual is a monotonic function. As a result, the original signal is represented in terms of a collection of IMFs and the residual.

A handful of EMD solutions have been proposed. For example, an algorithm called ensemble EMD (EEMD) was implemented in [90]. The authors designed it to overcome the EMD mode mixing effect. Mixing effect means that different time scale oscillations can coexist in the same IMF or different IMFs are assigned to oscillations with the same time scale. Hence, the EEMD algorithm removes this effect by adding white noise to the signal. In order to find an optimal EEMD level, lower IMFs are suppressed until a given mean square error (MSE) is found. The EEMD algorithm, however, is very time consuming to obtain the adequate IMF levels. Another ECG denoising algorithm based on EMD is presented in [91]. The algorithm finds the first-order intrinsic mode function named F-IMF, which contains higher frequency components (where the most artifacts are located). Then, three statistical measurements are calculated to analyze motion artifacts complexity, and variability such as Shannon entropy (characterize randomness), mean (quantify low noise level), and variance (quantify variability). The authors found threshold values for the three statistical measurements plotting characteristic curves of 24-hour recordings from 15 healthy people. Those threshold values allow separating the clean signal from the noisy ECG signal. Moreover, the F-IMF signal is normalized and squared in order to find another threshold value for

the optimum low-noise level. The three statistical measurements are analyzed for each threshold value. If the measurements are higher than the threshold values, the segment is declared as noise corrupted. On the other hand, if one segment has a lot of ECG information, it is detected as noise free. However, a limitation of this algorithm is that the three statistical threshold values depend on long-term measurements from an individual user. Typically, EMD algorithms have been tested on ECG signals corrupted by Gaussian noise, as well as recorded noise from the MIT-BIH Noise Stress Database [21]. Typically, an SNR level of around 10 dB is assumed (e.g., see [92]), thus higher than levels witnessed in today's wearable devices, which can reach levels of SNR=-10 dB in extreme cases.

The wavelet transform, in turn, represents an ECG signal as the sum of the product between a mother wavelet and wavelet coefficients thus representing low and high frequency components in the signal. These components are then filtered by low-pass and high-pass filters with different cut-off frequencies. For enhancement purposes, wavelet coefficients with noise (highest components with some QRS information) and with most of the QRS information (lowest components) are separated. The performance of the wavelet denoising algorithm relies on a choice of several parameters, such as mother function, thresholding method (i.e., soft and hard), number of decomposition levels, and threshold selection rules (i.e., universal, Stein's Unbiased Risk Estimate (SURE), heuristic SURE, and minimax); typically, these are selected empirically [33]. The universal shrinkage method finds the threshold as  $\sqrt{2 * \log(n)}$ , where  $n$  is the number of wavelet coefficients. SURE, in turn, uses the principle of Stein's unbiased likelihood estimation, where given the threshold, likelihood estimation is calculated and the non-likelihood threshold is minimized [93]. Heuristic SURE combines these two methods, and finally, minimax finds the threshold value that results in the minimum error between wavelets coefficients of the noisy and original signals.

Several wavelet solutions have been proposed in the literature. For example, a wavelet Wiener filtering method is proposed in [94]. The authors add a block for noise estimation with two inputs: the noisy signal and the estimated noise-free signal. Then, the wavelet and filter parameters are configured based on this estimation. The algorithm uses two adaptive methods. In the first one, the signal is divided into segments with a constant level of noise, which are filtered according to that level. In the second, the threshold value for each segment is configured based on the standard deviation of the noise. A fixed threshold value is not possible for signals with dynamic noise changes requiring an adaptive configuration. The stationary wavelet transform (SWT) in the Wiener filter is used in order to find the filter parameters and a suitable filter bank according to the SNR. This method is compared with the classic wavelet Wiener filter obtaining a better performance.

A variant combines both the EMD and wavelet principles for ECG enhancement, as proposed in [92]. The algorithm aims at preserving the QRS complex information contained in the first three IMFs. To this end, a windowing in the EMD domain is performed. Then, the noise-reduced signal is carried out to DWT domain, where adaptive thresholding of the wavelet coefficients is used for reconstructing the clean ECG signal. A sum signal resulting of the three IMFs signals is obtained, where the QRS complex is bounded by two zero crossing points and the R-wave peak (maximum of the noisy segment) is identified. Also, the QRS complex is conserved using a time domain window (Tukey window) centered in the R-wave peak with a length that covers the entire QRS complex. This method was compared with EMD soft thresholding, wavelet soft thresholding, and EMD-wavelet methods using SNR, MSE, and percent root mean square difference (PRD). It was found that it achieved better performance at different SNR levels.

Moreover, DWT and artificial neural networks with adaptive learning ability can be combined for ECG denoising. For example, in [95], the authors propose a modified wavelet transform called “multi-adaptive bionic wavelet transform” (MABWT). The wavelet transform decomposes the signal into wavelets coefficients, where their threshold value is found using a self-learning and adaptive artificial neural network. The high frequency noise is discarded in the thresholding process. Then, the denoised coefficients are passed as input to the artificial neural network. The network performs an inverse wavelet transform to reconstruct the signal and acts as a nonlinear adaptive filter to reduce the noise. The weights of the neural networks are updated using the error signal obtained when the network compares its output with the clean ECG signal. The authors compared their method with traditional wavelet transforms and found SNR improvement and reduction of several types of noise. Another approach using genetic algorithm and wavelet hybrid scheme for ECG denoising is found in [96]. The genetic algorithm is used to select the optimal wavelet parameters. This selection, normally, is made empirically depending on the user’s experience and the signal. The genetic algorithm uses selection, crossover, and mutation and works over a population (possible values of the parameters). After several iterations, the genetic algorithm finds the best solution based on an objective function and MSE. The approach is evaluated using the SNR and PRD in order to analyze the noise reduction performance. The results showed a better performance compared with other wavelet methods. In addition, the authors also found that soft thresholding is better than hard thresholding as the former produced discontinuities in the signals.

Fuzzy logic methods are also used to denoise ECG signals. For example, wavelet packet analysis and fuzzy thresholding are combined in [97]. The threshold value and variance for the wavelets coefficients are constant in the soft and hard thresholding methods. As a result, some important coefficients can be discarded or noise components can be taken as clean signal. Consequently, the

authors propose a method to find these values in an optimal manner, where the signal is decomposed into several levels using the wavelet packet transform. Then, a fuzzy method is applied in order to find the threshold adjusting a gradient s-function value. Then, the highest correlation coefficient is found to select the adequate threshold and variance values. Finally, the signal is reconstructed using the inverse wavelet packet transform and the coefficients. The method is compared with the traditional soft and hard thresholding methods showing a better SNR performance. Moreover, an algorithm to identify motion artifacts consisting in clustering, fuzzy logic, and multi-parameters decision is proposed in [98]. A QRS feature extraction block detects beats separated into clusters according to QRS waveforms. The beats are divided into four groups according to a QRS histogram curve. The rules and threshold values for that division are based on many experiments. The beats are divided according to a distribution obtained from the histogram curve. Then, a dynamic and self-learning clustering process separates the beats with different shape in different clusters using template beats and several matching rules. A curve is obtained using fuzzy-logic and reflects the variability of QRS waveforms and the likelihood of the motion artifact segments. Finally, the motion artifact is discriminated using kurtosis from the time domain signal and other beat features. However, this algorithm will not detect the single motion artifact (present in portable ECG devices) in clean ECG recordings because the artifact detection is based on QRS waveform variability beat to beat.

Other solutions based on filtering have been proposed. In [99], adaptive filtering using a moving average filter was proposed and tested on signals corrupted with additive white Gaussian noise. Moreover, in [100], a nonlinear Bayesian filtering framework was proposed and used in several Bayesian filters, including the extended Kalman filter, smoother, and unscented Kalman Filter. Experimental results with additive white and coloured Gaussian noise across a wide range of SNR

values (ranging from 30 to -5 dB) showed the algorithm to perform well at SNR levels below 15 dB and achieved SNR gains (relative to input SNR) of 10 dB for an input SNR of -5 dB. Notwithstanding, issues with filter stability and convergence in the presence of abnormal ECGs and more realistic noise scenarios were highlighted, as was the need for some *a priori* information, thus making the algorithm not completely 'blind'.

Although the aforementioned solutions have shown a good performance to denoise ECG signals, they have some limitations since filtering and estimation procedures can distort the R-wave interval and produce an incorrect reconstructed signal [91]. In addition, other limitations in the mentioned denoising methods are: i) with adaptive filtering, a reference signal is required to be correlated with the motion artifact and must be recorded at the same time as the ECG signal, ii) machine learning based solutions are extremely sensitive to changes in training data characteristics [92], thus may limit performance of data recorded by a new unseen device; iii) EMD and wavelet-based solutions, despite being the most popular, rely on numerous parameters that need to be optimized a priori, such as IMF thresholding method, mother wavelet, decomposition level, thresholding type (soft/hard), and shrinkage type [[93], [101]-[102]]. In our pilot experiments, it was observed that wavelet-based methods performed better across different datasets, thus are used herein.

Notwithstanding, despite the numerous existing ECG enhancement algorithms available in the literature, it has been observed that the majority are tested only on moderate amount of noise levels, roughly around 5-10 dB SNR. With wearables under extreme movement conditions, much noisier signals are recorded, thus limiting the usage of existing algorithms under such harsh settings.

## 2.4 Benchmark ECG Quality Metrics

To date, a handful of ECG quality indices have been developed [15]. The most widely-used measures include:

- ECG root mean square (RMS) value computed within the isoelectric region (i.e., the period between atrial and ventricular depolarization).
- Ratio of the R-peak to noise amplitudes in the isoelectric region.
- Peak-to-RMS ratio.
- The in-band to out-of-band spectral power ratio (IOR) within the QRS complex [15]. The latter measure assumes that the majority of the ECG spectral power will be between 5 – 40 Hz. Assuming a 256 Hz sample rate, the IOR metric is defined here as:

$$IOR = \frac{\int_5^{40} X(f)df}{\int_{0.05}^{128} X(f)df - \int_5^{40} X(f)df}, \quad (2.10)$$

where  $X(f)$  corresponds to the ECG power spectrum density. Higher IOR values are expected for better quality ECG signals.

- The kurtosis of the ECG signal ( $\kappa$ ) [26], or the fourth-order moment, which measures the peakedness of the signal and is given by:

$$\kappa = \frac{\frac{1}{N} \sum_{i=1}^N (x(i) - \bar{x})^4}{\left(\frac{1}{N} \sum_{i=1}^N (x(i) - \bar{x})^2\right)^2}, \quad (2.11)$$

where  $\bar{x}$  is the sample mean of  $x(n)$  and  $N$  are the total number of ECG data points. The kurtosis value increases as the signal quality increases [25]. In [28], a threshold is set such that  $\kappa \geq 5$  is assumed for high quality ECG.

Such measures can be computed for single-lead ECGs, as commonly found in unsupervised telehealth applications [60], or integrated over multi-lead systems using advanced pattern recognition methods (e.g., [103]). Moreover, a few measures rely on characteristics of the ECG waveform (e.g., the T-P to QRS interval power ratio [104]), which may become unreliable in very noisy scenarios where the QRS complex can be buried in noise. Other more advanced measures have also been reported for multi-lead systems and rely on classifiers, adaptive filtering, or inter-lead features (e.g., lead crossing) to classify ECG signals as acceptable or not [9, 105–107]. Several such metrics have been compared in #2 and the kurtosis-based metric has typically been used in the literature.

## 2.5 Proposed ECG Modulation Spectral Analysis

In [108], it is argued that “the presence of amplitude modulation in bioelectrical processes is of fundamental nature, since it is a direct reflection of the control, synchronization, regulation, and intersystem interaction in the nervous and other body systems”. As such, it is expected that the modulation spectral signal representation, which measures the modulation (rate-of-change) of spectral components present in a signal, would lend itself well to ECG analysis. The riding principle is that while cardiac components will have limitations imposed by human physiology, noise/artifact components will not, thus the spectral rate-of-change of the two will differ. Modulation spectral signal analysis consists of the frequency decomposition of temporal trajectories of short-term sig-

nal spectral components, hence it can be viewed as a frequency-frequency signal representation. Modulation spectral analysis has been used in the past to separate heart and lung sounds from digital auscultation recordings [17], as well as speech and ambient noise from real-world microphone recordings [18]. It renders itself useful to such “source separation” applications, as different signals are known to have spectral components modulated at different rates. For ECGs, it is proposed as a tool to separate cardiac and noise components from the recorded noisy signal thus allowing for blind quality assessment, signal enhancement, and noise-robust analyses.

Figure 2.8 depicts the signal processing steps involved in the computation of the ECG modulation-spectral representation. First, the ECG signal  $x(n)$  (here sampled at 256 Hz) is segmented into consecutive overlapping frames using a 32-point sine window with 75% overlap, which are then transformed to the frequency domain using a 512-point fast Fourier transform (FFT), thus resulting in a conventional spectrogram. Spectral magnitude components  $|X(f, m)|$  (for frame index  $m$ ) are then also segmented over the time axis into consecutive overlapping frames using 128-point “modulation” windows with 75% overlap, which are further processed by a 512-point FFT into the final frequency-frequency representation  $\mathcal{X}(f, f_m, k)$  called the modulation spectrogram, where  $f$  corresponds to conventional frequency,  $f_m$  to modulation frequency, and  $k$  is the frame index for the second transform.

It is important to emphasize that these options for base and modulation window sizes, as well as overlap rates were optimized using training synthesized clean ECG data and that they impose a limitation on the minimum duration of a test ECG to be of four seconds. In our pilot experiments, we have found that reducing the modulation window to 64 points (thus reducing the ECG duration limitation to 2 seconds), for example, causes a slight decrease in quality measurement performance

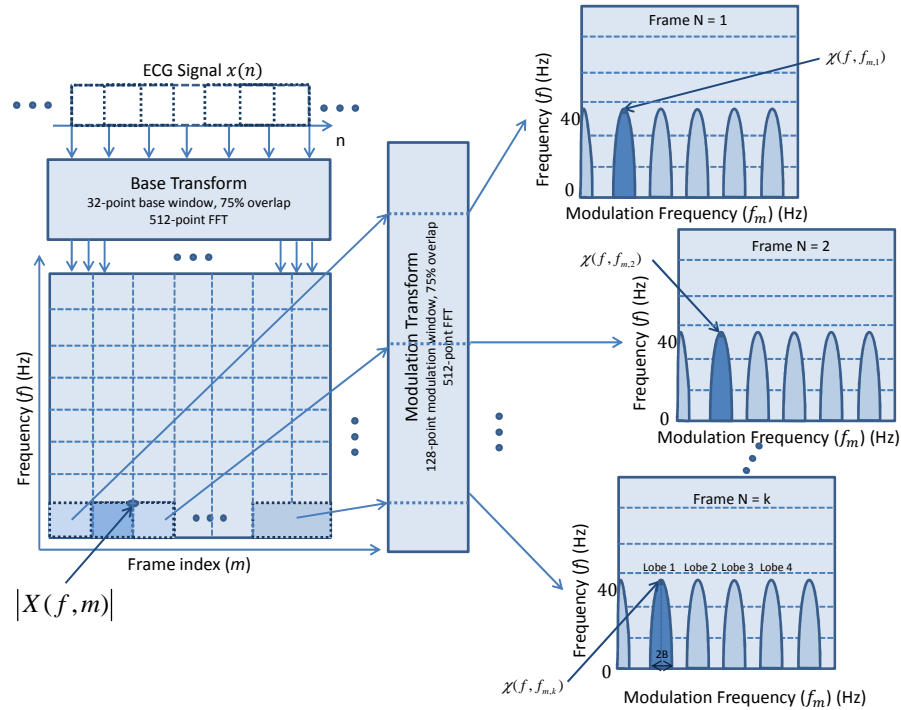


**Figure 2.8** – Processing steps to calculate the modulation spectral signal representation. Base transform (e.g., short-time Fourier transform) is applied to the sampled ECG signal  $x(n)$  to obtain a time-frequency representation. Spectral magnitudes  $|X(f, m)|$  are windowed across time and a second transform (modulation transform) is applied to obtain the frequency-frequency modulation frequency representation  $\chi(f, f_{m,k})$ .

(around 2%). As such, the proposed index may still be further fine-tuned for alternate applications requiring fast responses, such as in intensive care units.

In order to motivate the use of the modulation domain for noise-robust ECG analysis, Figures 2.9 (a) and (b) depict the average per-frame modulation spectrograms shown in Figure 2.8 (right side) of synthetic clean ECG signals with 60 and 150 beats per minute (bpm), respectively (averaged over 2 minutes of ECG data). As can be seen from the two subfigures, the majority of the signal energy is below  $f < 40$  Hz. For the first scenario, i.e., 60 bpm, it can be seen that the ECG spectral components change with a rate of  $f_m = 1$  Hz, as well as several other harmonics. In the case of 150 bpm, spectral components change with a rate of  $f_m = 2.5$  Hz, along with its harmonics.

Figure 2.9 (c), in turn, shows a noisy synthetic ECG signal (with an  $SNR = 5$  dB and 150 bpm) that has been corrupted by several noise components taken from the MIT-BIH Noise Stress Test Database [20]. As can be seen, frequency components around  $f_m = 0$  Hz (i.e., stationary components) are of wider bandwidth ( $f > 40$  Hz) than their clean counterparts, modulation frequency “lobes” are of diminished energy, and modulation frequency energies between lobes are amplified. Notwithstanding, despite the low SNR, ECG components can still be clearly seen in the modulation spectrogram, with clear lobes still being detectable up to  $f_m = 8$  Hz, as opposed to 10 – 12 Hz in the clean ECG scenario. On the other hand, Figure 2.9 (d) shows recorded muscle contraction and electrode movement noise. It can be seen that the noise signal has no clear structure across the modulation frequency dimension and has high lowpass energy around  $f_m = 0$  Hz. Therefore, these insights have motivated us to develop an ECG quality index, an enhancement algorithm for improved peak detection, and a HRV index, which are presented in the subsequent chapters.

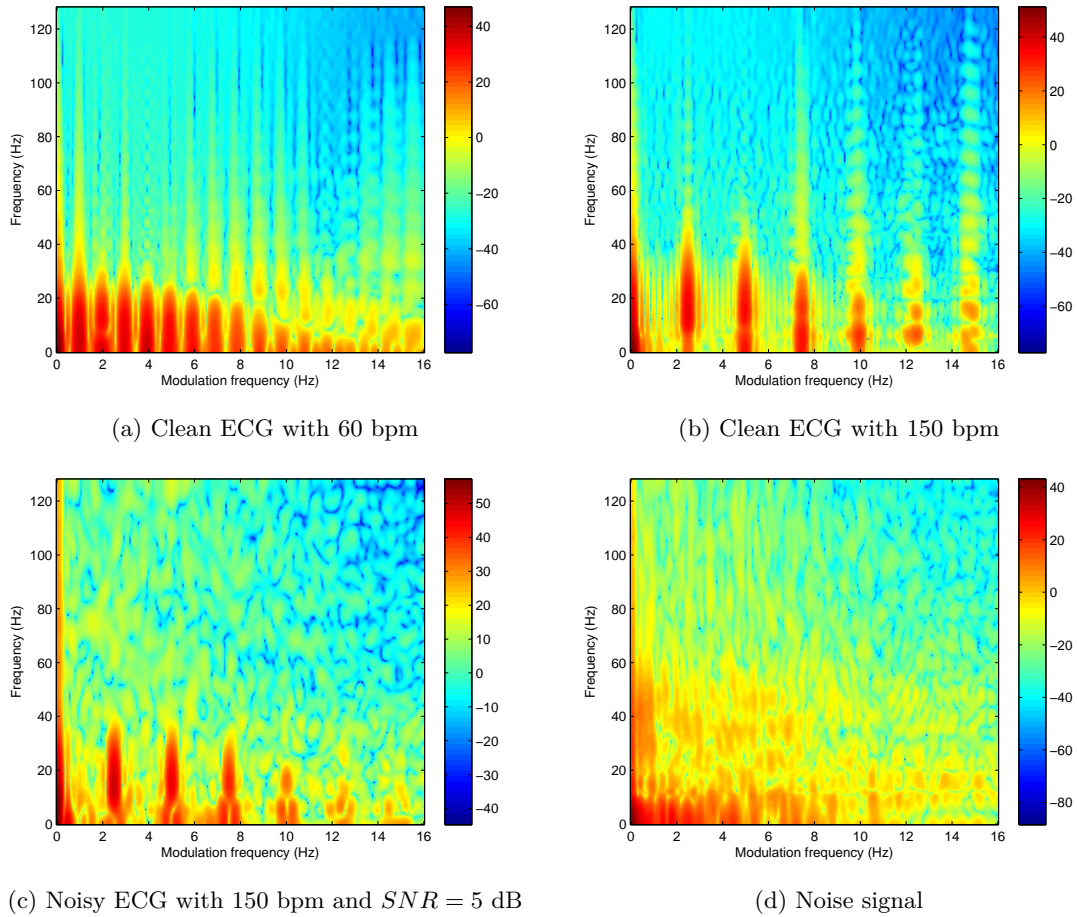


**Figure 2.9** – Modulation spectrograms of synthesized clean ECGs with (a) 60 and (b) 150 bpm, (c) noisy ECG with an  $SNR = 5$  dB (150 bpm), and (d) noise signal with recorded muscle contraction and electrode movement.

## **Chapter 3**

### **MS-QI: A Modulation**

# **Spectrum-Based ECG Quality Index for Telehealth Applications**

## **3.1 Preamble**

This chapter contains material extracted from publication #2 listed in Section 1.3.

## 3.2 Introduction

As shown in Chapter 2, the modulation spectral representation can be useful in separating noise from cardiac components from a noisy ECG signal. We use these insights to propose a signal-to-noise ratio like measure that is adaptive to the user’s heart rate, can operate with single-lead systems, and does not rely on classifier training or QRS detection. Moreover, the metric is shown to outperform two conventional benchmark quality indices across four datasets covering both synthesized and recorded ECGs, as well as ECGs collected from healthy and pathological patients. As such, the proposed metric is shown to be an ideal candidate for emerging remote patient monitoring and telehealth applications.

The remainder of this chapter is organized as follows. Section 3.3 describes the motivation of using the modulation spectral signal representation for ECG quality assessment, the proposed MS-QI measure, and the experimental setup. Experimental results are then presented in Section 3.4 and discussed in Section 3.5. Finally, chapter conclusions are drawn in Section 3.6.

## 3.3 Modulation Spectrum Based Quality Index

From Figures 2.9 (a)-(c), it can be seen that ECG and noise components behave differently in the so-called modulation spectrum domain. ECG components appear in “modulation frequency lobes” centred in modulation frequencies related to the heart rate and its harmonics and are confined to lie between  $0 \leq f \leq 40$  Hz. Noise components, on the other hand, do not follow such patterns and can affect several modulation frequencies, particularly  $f_m = 0$  Hz due to the stationarity properties

of some noise sources (frequency components with zero mean and constant variance). Using these insights, we develop a modulation spectral-based ECG quality index that is akin to a signal-to-noise ratio measure.

To compute the measure, the first “lobe” needs to be detected within each per-frame modulation spectrogram  $\mathcal{X}(f, f_{m,k})$ , thus corresponding to the user’s instantaneous heart rate. To this end, the energy for each modulation frequency bin is computed between  $0.8 \leq f_m \leq 3.3$  Hz (thus covering heart rates from 48-198 bpm) and averaged over the  $0 \leq f \leq 40$  Hz range. The modulation frequency bin  $f_m^*$  with the highest energy is selected as the centre of the first lobe. We have found experimentally that a lobe bandwidth of 0.625 Hz (i.e., one modulation frequency bin to the right and one modulation frequency bin to the left of  $f^*$  ( $2B$ )), as shown in the right-hand side of Fig. 2.8 (frame  $k$ ), results in accurate and reliable results. This lobe bandwidth is related to the particular configuration used to compute the modulation spectrogram as described in Section 2.5 (i.e., sampling frequency, window sizes, overlap, and zero padding). Next, the total ECG modulation energy (EME) for frame  $k$  needs to be computed as the sum of the modulation energies present in the main lobe and in its harmonics. For the sake of quality assessment, we tested the computation of the EME parameter using 1 – 4 harmonics and found that three harmonics (i.e., a total of 4 lobes) resulted in the best performance. As such, the ECG modulation energy is computed as:

$$EME(k) = \sum_{j=1}^4 \mathcal{X}(f|_0^{40}, jf_{m,k}^* - B \leq jf_{m,k}^* \leq jf_{m,k}^* + B), \quad (3.1)$$

where  $f|_0^{40} = 0 \leq f \leq 40$  and  $B = 0.3125$  Hz. The assumption here is that EME parameter represents the information available from the actual ECG components and that everything outside the first four lobes will correspond to noise/artifacts. As such, the per-frame modulation spectral based quality index (MS-QI) is given as the ratio of EME to the remaining modulation energy

(RME), i.e.,

$$MS-QI(k) = \frac{EME(k)}{RME(k)}, \quad (3.2)$$

where RME is found as the difference between the total energy in the modulation spectrogram and EME. The final quality index MS-QI is given as the average MS-QI(k) over all frames in the recorded ECG signal. While the metric is not mathematically bound between [0,1], we have observed experimentally MS-QI values are typically between 0 – 1.5, with higher values corresponding to improved quality.

### 3.3.1 Dataset 1: Synthetic ECG Data

We used the *ecgsyn* Matlab function available in Physionet to generate synthetic ECG signals [21] as described in Chapter 2, Section 2.1.3. For the experiments described herein, 200 signals of 120-second duration were generated by randomly sampling two input parameters: heart rate (uniformly sampled between 50 and 180 beats per minute) and LF/HF ratio (uniformly sampled between 0.5 and 8.9). The heart rate range was chosen to cover certain heart illnesses (e.g., tachycardia), as well as different physical activity levels (e.g., resting, walking, running). The LF/HF ratio range, in turn, covers wakefulness, rapid eye movement, light-to-deep sleep, and myocardial infarction [15]. Noisy signals were generated at SNRs of –5 dB, 0 dB, 5 dB, 15 dB, and 30 dB, following the steps described in [9]. Overall, a total of 40 hours of ECG data (clean and noisy) is available for testing.

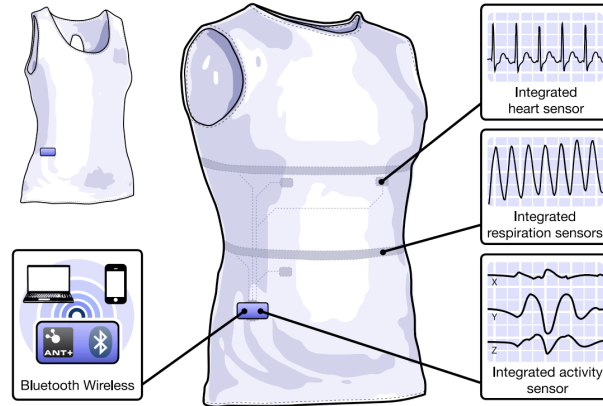


**Figure 3.1** – Hexoskin garment used to collect ECG data during three different activity levels: sitting, walking and running.

### 3.3.2 Dataset 2: Recorded Hexoskin Garment ECG Data

To test the developed quality metric on real recorded data, we use the Hexoskin smart shirt which is equipped with textile ECG, breathing, and 3-D accelerometry sensors (see Figure 3.1). Single-channel ECG signals are collected with 256 Hz sample rate and 12-bit resolution. The Hexoskin transmits data to smart devices via secure Bluetooth, thus is an ideal candidate for telehealth applications which could greatly benefit from an objective quality index. Here, data is recorded from three users wearing the Hexoskin during three different activity levels: sitting, walking and running. Figure 3.2 (a) depicts an actimetry profile measured via the device’s accelerometry sensors and shows the experimental protocol used: approximately 1-minute sitting (actimetry level: 0-50 arbitrary units), followed by 15-minutes running (actimetry level: 250-350) and lastly a 3-minute walk (actimetry level: 50-150). Actimetry levels are given every one second. Figures 3.2 (b) and (c), in turn, depict 10-second excerpts of the ECG data collected during the three activity levels, as well as their respective modulation spectrograms. As can be seen from the two subplots, actimetry values are inversely proportional to quality (i.e., higher activity level, lower ECG quality), as described in [22]. Overall, roughly one hour of data is available for testing.

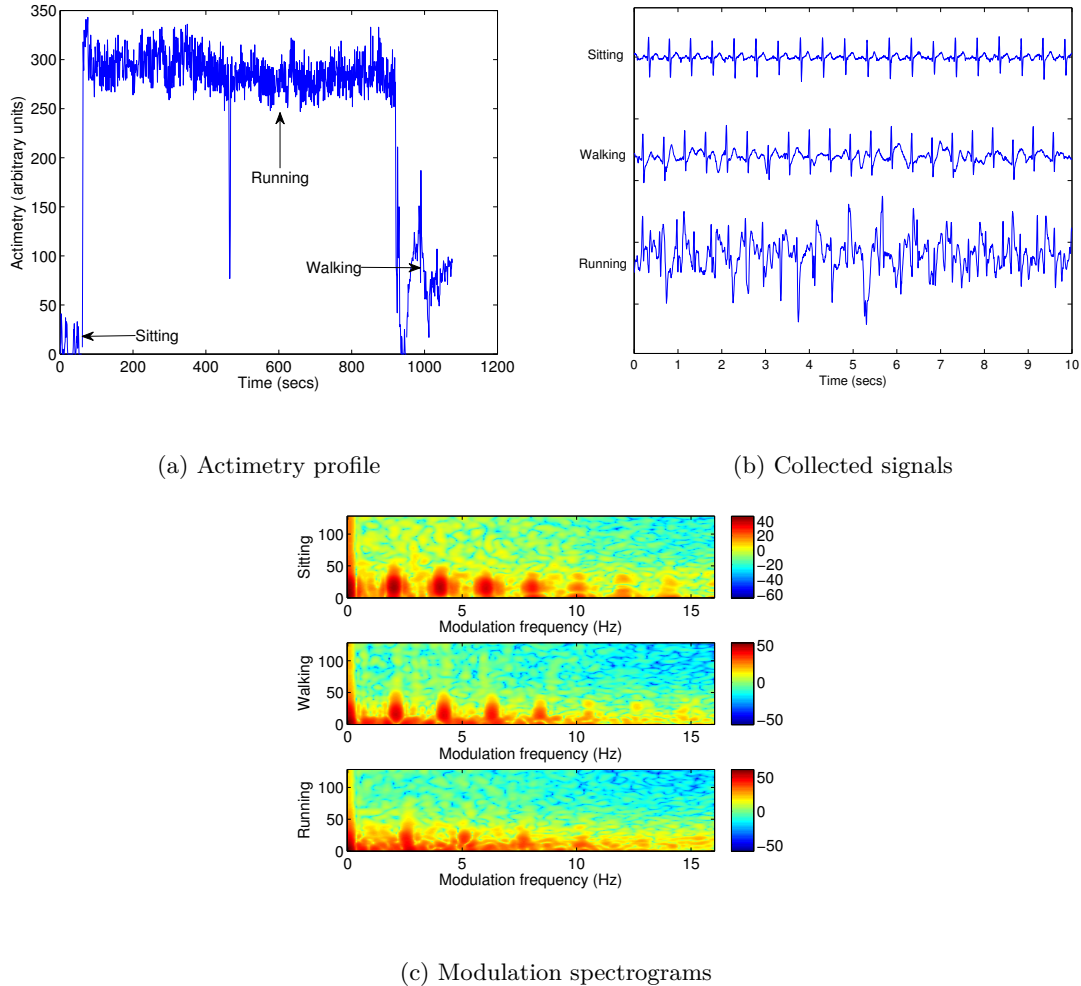


Figure 3.2 – Plots of (a) actimetry profile for ECG recording with the Hexoskin garment, (b) 10-second excerpts of the collected signals during (top to bottom) sitting, walking, and running, and (c) modulation spectrograms for the collected signals.

### 3.3.3 Dataset 3: Physionet Challenge Signal Quality Database

To further test the proposed algorithm, we used a subset of the publicly available Physionet/Computing in Cardiology 2011 Challenge dataset [23]. Data consisted of 12-lead ECG collected at a 500 Hz sample rate using conventional ECG machines. The overall quality over the 12 leads were then manually annotated by a group of 23 volunteers, roughly half experienced and half inexperienced with ECG readings, and later categorized as “acceptable” or “unacceptable”. Here, 100 acceptable and 100 unacceptable 10-second single-lead recordings were randomly pre-selected and downsampled

to 256 Hz. Since a final overall acceptability rating was given over the 12-leads (e.g., by majority vote, if most leads were acceptable, the entire 12-lead signal was deemed acceptable), we found that some of the randomly selected single-channel ‘acceptable’ signals were actually unacceptable and vice-versa. As such, two raters visually inspected the 200 single-lead signals and re-labelled them. Overall, the raters were in agreement on 142 of the total 200 signals, thus the experiments described herein are based on 71 acceptable and 71 unacceptable signals, totalling 24 minutes of ECG data available for testing.

### 3.3.4 Dataset 4: Recorded Ambulatory ECG Data

Lastly, we were interested in testing if MS-QI would be suitable for pathological ECG recordings, thus validating its use for remote telehealth operation. To this end, we used the well-known Physionet MIT-BIH Arrhythmia Database [24]. Data is comprised of two-channel ambulatory ECG recordings collected from 47 cardiology patients (sampled at 360 Hz). The data was analyzed independently by two cardiologists who annotated the readings with beat, rhythm, and signal quality labels. Regarding the latter, segments of the recordings that were deemed noisy by the annotators were labeled as “noisy”, whereas the remaining segments are deemed to be clean. For our experiments, 62 clean and 65 noisy ECG segments of 2-minute duration were used after downsampling to 256 Hz, thus totalling 4 hours and 14 minutes of data available for testing.

### 3.3.5 Benchmark Quality Measures

For performance comparison purposes, two widely-used benchmark measures are used [25]. The first is the ECG sample kurtosis ( $\kappa$ ) [26], or the fourth-order moment. The second metric is the in-band (i.e., 5 – 40 Hz) to out-of-band spectral power ratio (IOR) within the QRS complex [15]. The reader can refer to Chapter 2, Section 2.4 for more details about these two metrics. Note that the proposed MS-QI metric can be seen as an extension of the IOR metric, in the sense that it also looks for ratios of ECG and “non-ECG” components, but with the advantage of having access to a richer pool of information via the modulation frequency content.

### 3.3.6 Performance Assessment

To assess the effectiveness of the proposed and benchmark measures on the first two datasets, two performance figures-of-merit are used, namely the Pearson and Spearman rank correlations. Pearson correlation ( $\rho$ ) measures the linear relationship between two variables  $q(n)$  and  $t(n)$  and is given by:

$$\rho = \frac{\sum_{i=1}^N (q(i) - \bar{q})(t(i) - \bar{t})}{\sqrt{\sum_{i=1}^N (q(i) - \bar{q})^2 \sum_{i=1}^N (t(i) - \bar{t})^2}}, \quad (3.3)$$

where  $\bar{q}$  and  $\bar{t}$  are the sample averages of  $q$  and  $t$ , respectively.

Here,  $q(n)$  represents the estimated quality indices given either by the proposed metric or the two benchmark measures. The variable  $t(n)$ , in turn, represents the true quality value and is given here as either the SNR value in the synthetic ECG case (Dataset 1) or the actimetry level in Dataset 2. In the latter case, since only three activity levels are present, estimated quality values

are computed for a series of 5-second excerpts of the recorded data within each activity type. All investigated metrics are positively correlated with SNR and negatively correlated with actimetry levels. The second metric, Spearman rank correlation ( $\rho_S$ ), measures how well the quality indices rank against the “true” quality indicators (e.g., SNR and activity level). The  $\rho_S$  metric is calculated using (3.3) but with the original data values replaced by the ranks of the data value. A reliable quality indicator will have  $\rho$  and  $\rho_S$  close to unity. For the third and fourth datasets, in turn, since only “acceptable” and “unacceptable” (or “noisy” and “clean”) labels are available, we use the overlap in distributions between the two classes as a figure of merit. In essence, a smaller overlap indicates greater class separability, thus a better quality index. A two-sample Kolmogorov-Smirnov test is used to statistically quantify the separability of the two distributions. Overall, 45 hours and 38 minutes of ECG data are used in our analyses.

### 3.4 Results

Table 3.1 shows the performance obtained with the proposed and the two benchmark metrics for Datasets 1 and 2. For Dataset 1, the correlations are between the obtained metrics and the SNR values for all 1000 signals (200 signals  $\times$  5 SNR levels). For Dataset 2 the correlations are between the obtained metrics and actimetry levels. The scatterplots depicted by Figures 3.3 (a)-(c) show the behaviour of the MS-QI,  $\kappa$ , and IOR metrics, respectively, as a function of SNR for the synthetic ECG signals. To avoid cluttering, only the average metric values per SNR are shown, along with their standard deviations. Moreover, Figures 3.4 (a)-(c) show the behaviour of the MS-QI,  $\kappa$ , and IOR metrics as a function of actimetry level for Dataset 2. To avoid cluttering, only nine 5-second

Dataset	Map	MS-QI		$\kappa$		IOR	
		$\rho$	$\rho_S$	$\rho$	$\rho_S$	$\rho$	$\rho_S$
1	–	0.95	0.93	0.90	0.93	0.93	0.97
	Log	0.90	0.93	0.89	0.93	0.94	0.97
2	–	-0.94	-0.92	-0.81	-0.92	-0.71	-0.89
	Log	-0.90	-0.92	-0.92	-0.92	-0.83	-0.89

**Table 3.1** – Performance comparison between proposed MS-QI measure and the two benchmark metrics for Datasets 1 and 2.

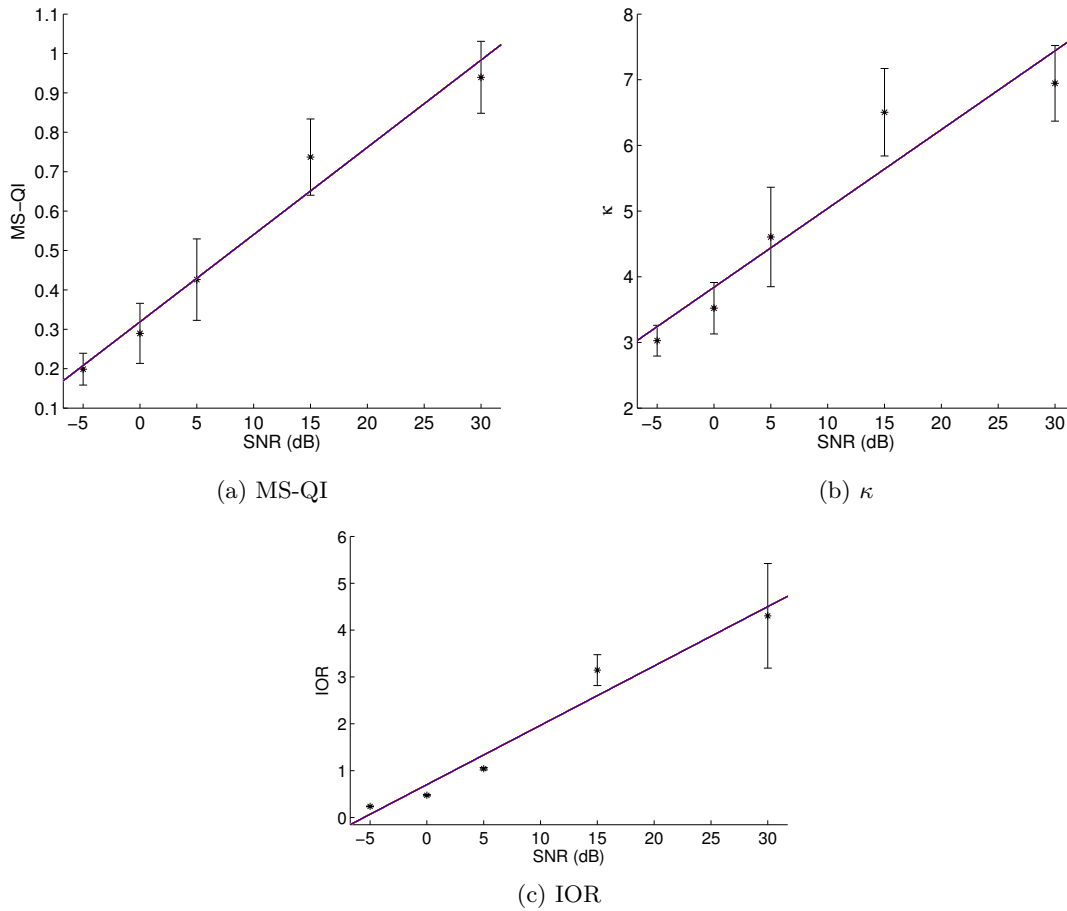


**Figure 3.3** – Scatterplots and errorbars of (a) MS-QI, (b)  $\kappa$ , and (c) IOR as a function of SNR for Dataset 1.

excerpts per activity level are presented. As can be seen, a logarithmic behaviour is present, thus the performances in Table 3.1 are listed both without and with a logarithmic mapping.

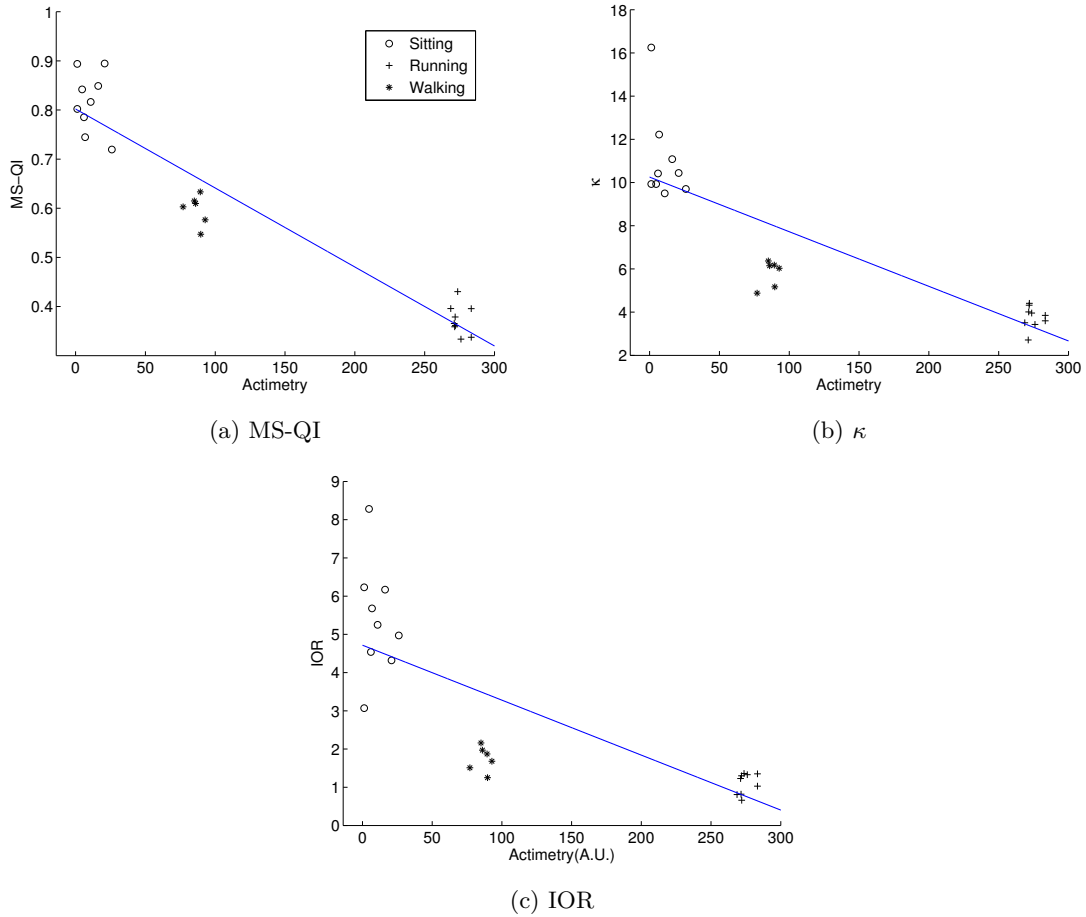


**Figure 3.4 – Scatterplots of (a) MS-QI, (b)  $\kappa$ , and (c) IOR as a function of activity level (actimetry) for Dataset 2.**

Lastly, for Datasets 3 and 4 we use the overlap in distributions between the clean (acceptable, good quality) and noisy (unacceptable, bad quality) ECG recordings as a figure of merit. For the MS-QI metric, kernel fits for the probability distributions are depicted by Figure 3.5, where dark black curves correspond to clean recordings and light gray curves to noisy ones. Dashed lines are for Database 3 and dotted lines for Database 4. For comparison purposes, clean synthetic ECG data are represented by the solid black lines and noisy synthetic (i.e.,  $\text{SNR} \leq 15$  dB) data by gray solid lines. For the sake of brevity, comparisons are only performed for the  $\kappa$  benchmark metric as it performed more consistently across Datasets 1 and 2, relative to the IOR benchmark (see Table 3.1). Figure 3.6 (a) and (b) show the kernel fits for the probability distributions for Datasets 1, as well

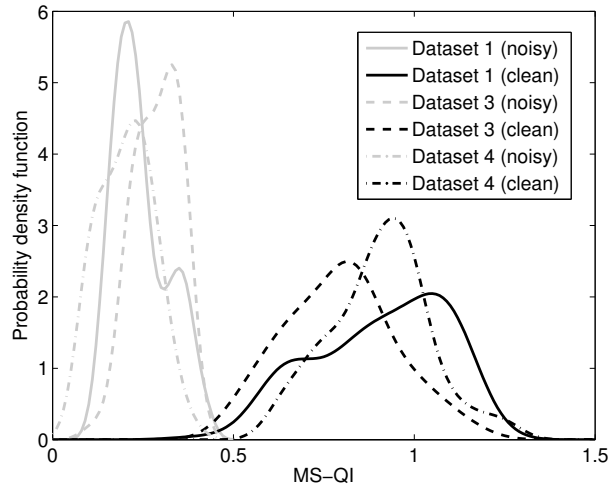


Figure 3.5 – Kernel fit of MS-QI probability distributions for good (black) and bad (gray) quality ECG for Datasets 1 (solid), 3 (dash), and 4 (dash-dot).

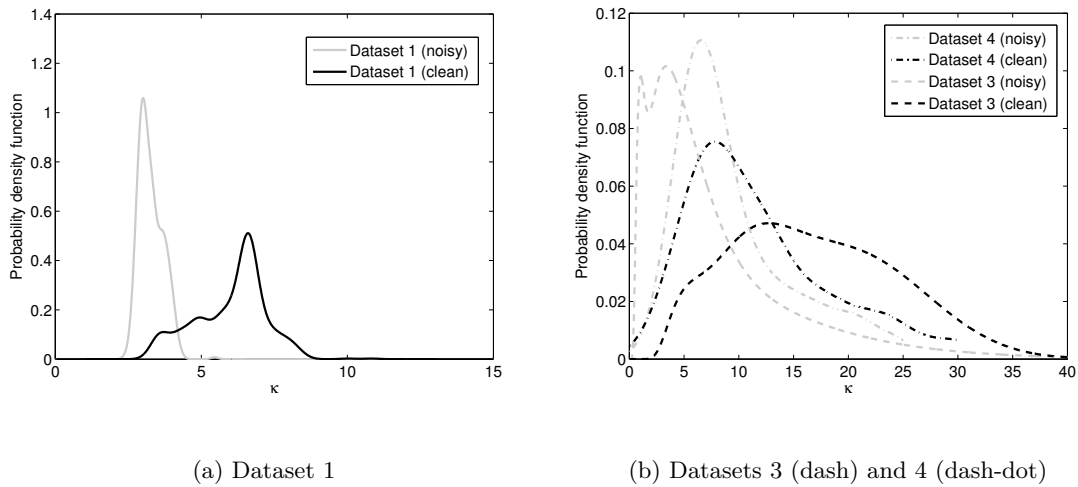


Figure 3.6 – Kernel fit of  $\kappa$  probability distributions for good (black) and bad (gray) quality ECG for (a) Dataset 1, (b) Datasets 3 (dash) and 4 (dash-dot).

as 3 and 4, respectively. As previously, black lines correspond to good quality ECG and gray lines to bad quality recordings.

### 3.5 Discussion

From Table 3.1, it can be seen that the proposed MS-QI metric outperforms the two benchmark algorithms on Datasets 1 and 2 in terms of the  $\rho$  performance metric. Relative to the  $\rho_S$  metric, it achieved results equal to  $\kappa$  on both datasets and outperformed the IOR metric on Dataset 2. The IOR metric, on the other hand, achieved the highest  $\rho_S$  on Dataset 1. Overall, the consistency of the MS-QI metric across the two Datasets suggests that it may be more suitable not only for remote telehealth applications, but also for athletic training applications where the ECG data is highly contaminated with movement artifacts. In fact, if we compare the scatterplot for the MS-QI metric in Fig. 3.4 (a) to that of the  $\kappa$  benchmark versus  $\log(\text{actimetry})$  in Figure 3.7, it can be observed that the discrimination between the three activity levels, particularly between the walking and running conditions, remains higher for the proposed quality index, thus also suggesting potential applications as an activity type detector in telehealth applications. Interestingly, of the three activity conditions explored with Dataset 2, sitting was the one that showed the highest variability, particularly for the benchmark metrics. This could be an artifact from the data collection protocol, as sitting was the first activity performed during data collection and textile ECG coupling may have been lower due to lack of moisture and sweat [27]. Moreover, the performance gains relative to the IOR metric across the two datasets show the importance of the modulation spectral information for the development of a blind SNR-like measure for ECG signals.

As mentioned above, the proposed MS-QI measure achieved comparable results with the  $\kappa$  benchmark, particularly for the  $\rho_S$  metric. The benefits of the proposed MS-QI metric, however, become more apparent from the data collected in real-world settings, such as from Datasets 3 and 4. From Figure 3.5, it can be easily seen that the overlap in probability distributions between the good

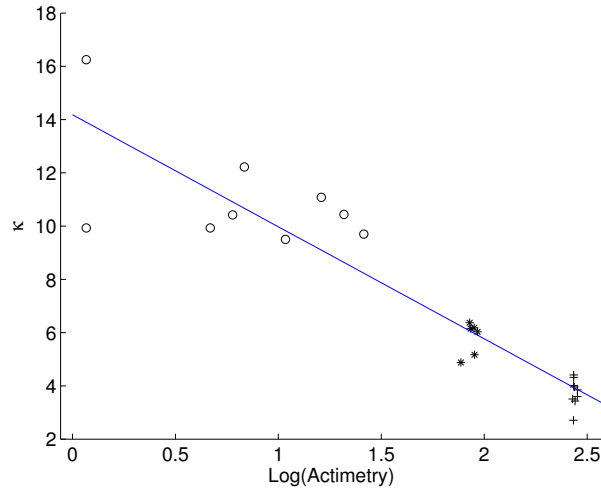


**Figure 3.7 – Scatterplot of  $\kappa$  as a function of  $\log(\text{actimetry})$  for Dataset 2.**

and bad ECG signals was minimal for the MS-QI metric, with a clear boundary between the two conditions at MS-QI = 0.5. This finding remained true not only for the recorded datasets, but also for the synthetic ECG, thus showing the robustness of the proposed metric to ECG type (recorded/synthetic) as well as patient condition (healthy/pathological). The  $\kappa$  metric, on the other hand, showed to be sensitive to ECG type with significant differences in probability distributions between synthetic (Fig. 3.6a) and recorded ECGs (Fig. 3.6b). While the  $\kappa = 5$  boundary between the two conditions, as reported in [28], could be seen with the synthetic ECGs, it increased to nearly 10 with the recorded data. This behaviour may be due to the sensitivity of the fourth order moment to outliers in the noisy signals, which may be misinterpreted as beats in clean ECG recordings [28]. Moreover, the  $\kappa$  metric showed a very high overlap in probability distributions for Dataset 4, thus limiting its use for quality monitoring of pathological ECGs. To quantify this separability statistically, a two-sample Kolmogorov-Smirnov test was used. For the  $\kappa$  parameter, the difference between the two distributions was deemed insignificant, ( $p = 0.11$ ), whereas the separability was highly significant for the proposed MS-QI measure ( $p < 10^{-30}$ ).

On the other hand, the computation time for a 2-minute length ECG signal was around 0.2 seconds for the proposed MS-QI metric, 0.04 seconds for the IOR, and 0.02 seconds for the  $\kappa$ . Even though processing time of the proposed quality index was roughly ten times that of the  $\kappa$  and five times that of the IOR, the findings suggest that in real-world settings the proposed metric outperformed both benchmarks outweighing that limitation in the computation complexity. However, it is important to mention that the Matlab codes developed herein can be optimized as a future work to further reduce processing time.

### 3.6 Conclusion

In this chapter, an innovative ECG quality index termed MS-QI was proposed based on modulation spectral insights. Using the new signal representation, ECG and noise components become more separable in the new modulation domain, thus allowing for a reliable quality measure to be developed. Experimental results showed the proposed measure outperforming two widely-used benchmark quality measures, namely ECG sample kurtosis and the QRS complex ‘in-band to out-of-band’ spectral power ratio, on synthesized ECGs, recorded healthy ECG, as well as recorded pathological ECGs. The proposed metric showed to be more reliable than the benchmark algorithms on four distinct datasets and its behaviour remained stable regardless of ECG type (synthetic vs. recorded), ECG recording mode (textile vs. conventional vs. ambulatory) and patient health (normal vs. pathological ECG). These findings suggest that the developed metric is a potential candidate not only for remote patient monitoring applications that involve patients being mobile and active, but also for athlete monitoring and activity type detection for telehealth applications.



## Chapter 4

# Adaptive Spectro-Temporal Filtering for Electrocardiogram Signal Enhancement

### 4.1 Preamble

This chapter contains material extracted from publications #4 and #5 listed in Section 1.3.

## 4.2 Introduction

A new method of *blind* single-channel ECG enhancement based on adaptive modulation domain filtering is explored. Modulation domain filtering has been proposed in the past for other biological signals, such as speech [18, 109] and auscultatory sounds [17] but this is the first time it is being proposed and validated for ECG enhancement. The modulation domain signal representation was shown to be invariant to ECG abnormalities and to accurately characterize ECG quality of low-cost portable sensors at very low SNRs, as shown in Chapter 3. The main principle behind the technique relies on the fact that the rate-of-change of ECG spectral components differ from the modulation spectral components of noise, thus can be easily filtered in this new domain. Here, we test the performance of the algorithm in improving peak detection in extremely noisy scenarios, thus allowing for accurate heart rate and heart rate variability measurement. Experiments with both synthetic and recorded ECGs are shown.

The remainder of this chapter is organized as follows. Section 4.3 describes the proposed heart rate detection approach using filtering in modulation domain, synthetic and real databases used in this study, benchmark measures, and performance assessment. Section 4.4 presents the experimental results and the discussion, Finally, Section 4.5 presents the conclusion.

## 4.3 Modulation Domain Filtering for Improved Peak Detection

Typically, the spectral rate-of-change of biological signals differ drastically from those of noise, thus filtering can be performed for denoising purposes. Here, a modulation domain filtering approach

for blind, single-channel ECG denoising is proposed. Figure 2.8 depicts the signal processing steps involved in computing the ECG modulation spectral representation. Since invertible transforms are used to find the spectro-temporal signal representation, filtering can be performed in the modulation spectral domain and the resultant signal can be reconstructed into a denoised ECG.

As shown in Fig. 2.8, clean ECG signals are comprised of clear ‘lobes’ in the modulation domain corresponding to stationary and non-stationary components. Heart rate information is clearly encoded in the first lobe and its harmonics. These lobes, however, are not as clear with noisy ECG due to the noise smearing modulation spectral components between lobes. As such, we propose to use a series of adaptive bandpass filters in the modulation domain to filter out noise components. The center modulation frequency of the bandpass filters are adaptive to the signal and rely on finding the  $f_m$  corresponding to the peak modulation energy between  $0 \leq f \leq 40$ . To speed up processing, we constrain the search to  $0.8 \leq f_m \leq 3.3$ , thus corresponding approximately to  $48 \leq \text{bpm} \leq 198$ . Moreover, in order to remove stationary noise components, the lowpass components near  $f_m = 0$  Hz are also removed. While removing these stationary components affects the complete reconstruction of the ECG signal, for heart rate detection in non-clinical applications (e.g., athlete monitoring) this has minimal impact. It is important to note, however, that for clinical applications requiring close-to-perfect reconstruction of P and T waves, further research would be needed to devise alternate filtering strategies for components around  $f_m = 0$  Hz.

Figure 4.1 depicts the block diagram of the signal processing steps involved in the proposed modulation filtering scheme and the steps performed within each modulation processing module. For the sake of notation, let  $s(f, m)$ ,  $f = 1, \dots, N$  and  $m = 1, \dots, T$ , denote the short-term spectral component at the  $f^{\text{th}}$  frequency bin and  $m^{\text{th}}$  time step of the short-term analysis.  $T$  and  $N$  denote

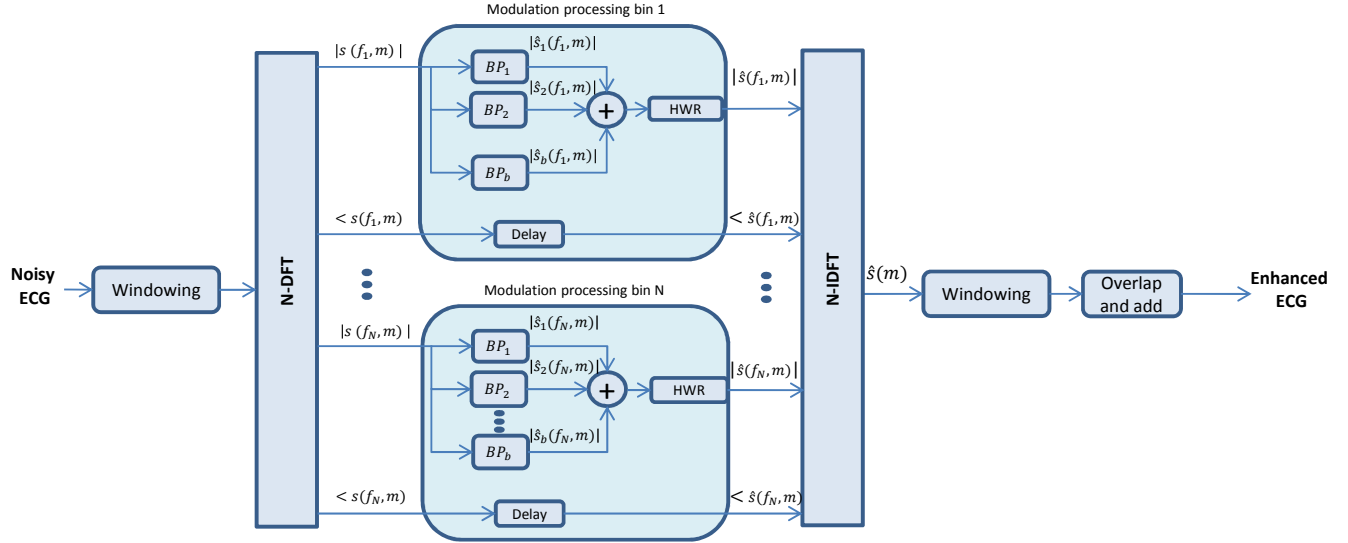


**Figure 4.1 – Block diagram of the general signal processing steps involved in the proposed modulation filtering scheme.**

total number of time steps and frequency bands, respectively. For a fixed frequency band  $f = F$ ,  $s(F, m), m = 1, \dots, T$ , represents the  $F^{th}$  band temporal trajectory. Here, frequency bands below  $f = 40$  Hz are processed. To simplify algorithm description, in the figure and text the discrete Fourier transforms (DFT) is shown, but in practice a fast Fourier transform was implemented.

For processing, the ECG signal is windowed by a 32-point power complementary sine window with 75% overlap. A 32-point DFT (no zero-padding) is then taken and the magnitude ( $|s(f, m)|$ ) and phase ( $\angle s(f, m)$ ) components of each frequency bin (up to 40 Hz) are input to a “modulation processing” module where modulation filtering and phase delay compensation are performed. The outputs of the N modules correspond to the processed magnitude ( $|\hat{s}(f, m)|$ ) and phase ( $\angle \hat{s}(f, m)$ ) components, which are input to an inverse DFT to generate  $\hat{s}(m)$ . The output is windowed by the power complementary window and overlap-and-add is used to reconstruct the denoised signal.

In essence, the “per frequency bin” magnitude trajectory  $|s(f, m)|, m = 1, \dots, T$  is filtered using a bank of  $B$  adaptive linear-phase finite impulse response (FIR) bandpass modulation filters (termed  $BP_b$ ) to generate signals  $|\hat{s}_b(f, m)|$ , where ‘b’ denotes the bandpass filter index. It was found experimentally that a lobe bandwidth in the modulation domain of approximately 0.625 Hz was optimal for the task at hand, as it allows for  $\pm 18.75$  (bpm) variability in the heart rate within the processing window, thus covering typical values seen for athletes [110]. Bandpass filters of length 101 were implemented [29]. For each ECG signal,  $B$  is found based on the centre modulation frequency of the main lobe and the maximum modulation frequency possible based on the choice of window and shift durations of the first transform. In our experiments this corresponded to 16 Hz, thus  $B$  typically ranged from 5-10 covering the main lobe plus 4-9 harmonics.

The  $|\hat{s}_b(f, m)|$  signals are then added to result in a final  $|\hat{s}(f, m)|$ . After bandpass filtering, however, the removal of lowpass modulation spectral content may result in negative power spectral values. As such, half-wave rectification (HWR) is performed to allow for signal reconstruction. Lastly, the remaining modulation processing step consists of delaying the phase by 50 samples, corresponding to the group delay of the implemented linear phase filters, thus resulting in  $\angle \hat{s}(f, m)$ . Figure 4.2 shows an ECG signal with 60 bpm and  $SNR = -5dB$  before and after modulation filtering. For comparison purposes, the output of a wavelet denoising algorithm is also shown, along with the modulation spectrograms of the noisy and two enhanced signals. Once the noisy ECG is enhanced, the Pan Tompkins algorithm [36] is applied to extract R peaks and RR time series, which are then input to the open-source HRVAS software to calculate HR and HRV metrics [30].

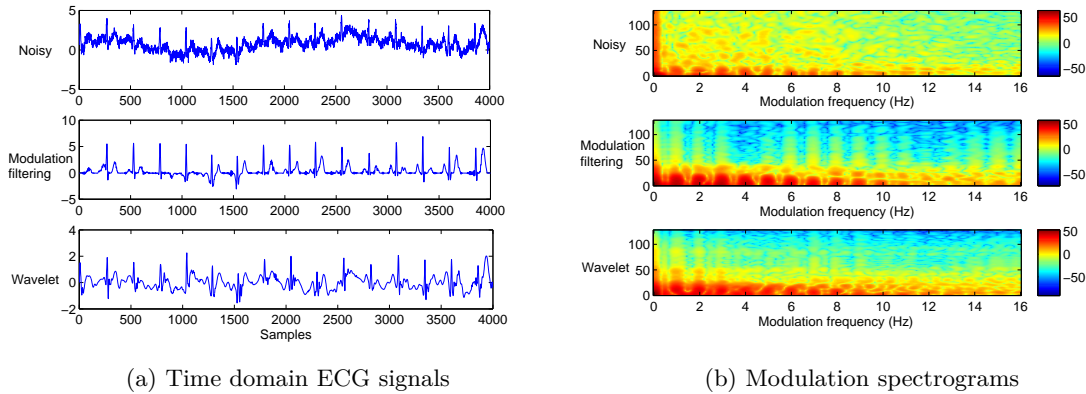


**Figure 4.2** – Plots of (a) time domain ECG signals with 60 bpm for a noisy ECG signal with SNR of -5 dB, and modulation filtering and wavelet enhanced signals, (b) modulation spectrograms for the noisy and enhanced signals.

### 4.3.1 Database 1: Synthetic ECG

Synthetic ECG data were generated using the Matlab function ‘ecgsyn’ available within Physionet [21] as described in Chapter 2, Section 2.1.3. Here, 700 2-minute signals sampled at 256 Hz were generated with heart rate values ranging from 50 to 180 bpm, as well as with varying LF/HF ratios randomly sampled between 0.5 and 8.9 as described in Chapter 3, Section 3.3.1. The clean ECG synthetic signals were contaminated at known levels in order to generate signals at five different SNR levels, namely  $\text{SNR} = -10, -8, -5, 0, \text{ and } 5$  dB. Overall, 3500 noisy 2-minute signals were available for processing, thus totalling over 116 hours of ECG data for testing.

### 4.3.2 Database 2: Physionet 2014 Challenge Data

In order to test the algorithm in more realistic scenarios, the Physionet/Computing in Cardiology 2014 Challenge dataset was also used. The challenge explored methods to locate heart beats in continuous long-term multi-channel recordings from bedside monitors of patients with a wide range of problems, as well as healthy volunteers. As argued in [31], the quality of the ECG signal varied

considerably over time, thus making the task of accurate heart beat detection challenging. Here, we used the ECG signals from the training and extended training sets, which contained reference beat annotation files found by expert volunteers. The two sets combined contained 200 signals of 10-minute duration (or somewhat shorter) and a sampling frequency of 250 Hz (in some cases in the extended set, a sampling rate of 360 was used).

### 4.3.3 Benchmark Algorithm and Performance Assessment Metrics

Two benchmark algorithms were explored, one based on EMD [32] and the other on wavelet denoising [33]. In pilot experiments, it was found that the wavelet-based benchmark consistently outperformed the EMD-based one, thus results are only reported herein for the former. The performance of the wavelet denoising algorithm relies on a choice of several parameters, such as mother function, thresholding method, number of decomposition levels, and threshold selection rules; typically, these are selected empirically [33]. In our experiments, we explore both hard and soft thresholding, as well as several different shrinkage rules, namely: universal, Stein’s Unbiased Risk Estimate (SURE), heuristic SURE, and minimax.

In order to optimize benchmark algorithm parameters for the task at hand, 100 files from Dataset 1 were used. Table 4.1 lists the errors (percentage) achieved in heart rate estimation between estimated HR estimates from the enhanced signal relative to the true HR for different SNR levels, as per (4.1):

$$\text{HR}_{error} = \frac{\text{true HR} - \text{estimated HR}}{\text{true HR}} \times 100\%. \quad (4.1)$$

SNR	HeurSURE	Minimaxi	SURE	Universal
-10	124.8	20.3	124.8	7.6
-8	59.8	1.8	59.8	1.2
-5	0.5	0.1	0.5	0.1
0	0.0	0.0	0.0	0.0
5	0.0	0.0	0.0	0.0

**Table 4.1 – Percentage HR estimation error for wavelet benchmark algorithm for different thresholding selection rules.**

As can be seen, the benchmark algorithm suppressed the artifacts sufficiently to achieve perfect HR estimation for SNR levels greater than 0 dB. For extremely noisy conditions, however, the universal shrinkage method resulted in the best performance, thus is used in our experiments. Moreover, the Daubechies 6 mother wavelet with 8 decomposition levels was used, based on insights from [34] and pilot experimentation.

In terms of performance, several metrics are used to gauge the benefits of the proposed algorithm. For the synthetic ECG signals (Database 1), since we have access to the original clean signal, the following metrics are used: (1) heart rate error percentage (as per Eq. 4.1); (2) Post-enhancement SNR; (3) kurtosis ( $\kappa$ ) measured within a window around the R peaks in the QRS complexes; (4) inter-beat-interval (IBI) error percentage, computed using (4.1) but with IBI values in lieu of HR; and (5) pNN50 HRV statistic error percentage between enhanced and clean signals. The pNN50 metric is a member of the time-domain pNNx family [35] and corresponds to the fraction of consecutive normal sinus (NN) intervals that differ by more than 50 ms. The reader can refer to Chapter 2, Section 2.2.1 for more details about these metrics. In the case of Database 2, since only the reference beat annotation files were available, the heart rate error percentage was used.

Input SNR (dB)	Noisy		Proposed			Benchmark		
	HR Error (%)	$\kappa$	HR Error (%)	Post-SNR (dB)	$\kappa$	HR Error (%)	Post-SNR (dB)	$\kappa$
-10	57.0 ± 73.6	3.1 ± 0.0	2.2 ± 3.2	1.4 ± 1.2	6.2 ± 1.5	6.2 ± 4.4	-2.3 ± 0.1	3.0 ± 0.1
-8	27.4 ± 41.7	3.4 ± 0.0	0.3 ± 0.3	2.5 ± 1.3	7.3 ± 1.6	1.7 ± 2.3	-2.0 ± 0.2	3.5 ± 0.1
-5	0.2 ± 0.2	4.2 ± 0.2	0.0 ± 0.0	3.9 ± 1.2	8.6 ± 1.7	0.2 ± 0.2	-1.2 ± 0.2	4.4 ± 0.3
0	0.0 ± 0.0	5.6 ± 0.4	0.0 ± 0.0	5.5 ± 0.9	10.0 ± 1.7	0.0 ± 0.0	1.2 ± 0.2	5.8 ± 0.6
5	0.0 ± 0.0	6.3 ± 0.6	0.0 ± 0.0	6.4 ± 0.7	10.7 ± 1.7	0.0 ± 0.0	5.0 ± 0.2	6.5 ± 0.8

**Table 4.2 – Performance comparison (HR error, post-SNR, and  $\kappa$ ) before and after enhancement with proposed and benchmark algorithms for Database 1.**

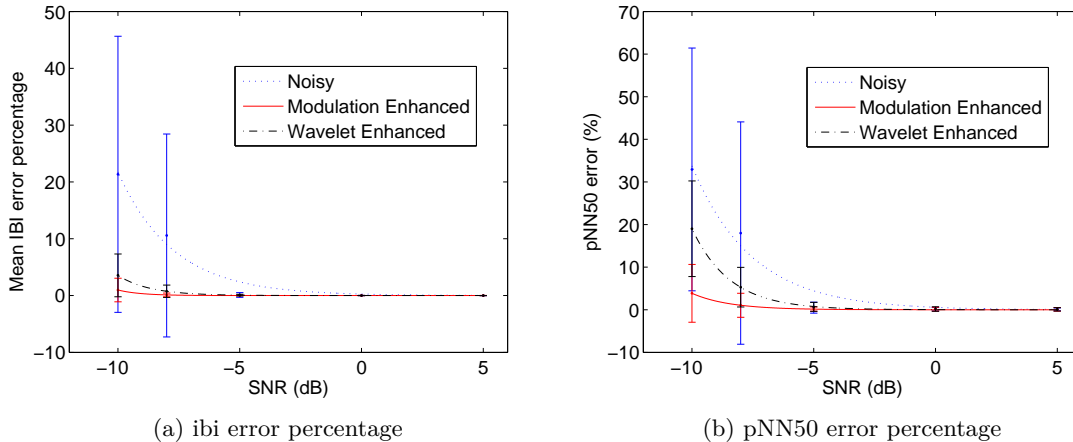


**Figure 4.3 – (a) Inter-beat interval (ibi) and (b) pNN50 error percentage for noisy, proposed, and benchmark-enhanced algorithms for Database 1.**

## 4.4 Experimental Results and Discussion

Table 4.2 reports the HR error percentage,  $\kappa$ , and SNR for the noisy signals in Database 1, as well as the performance metrics post enhancement for the proposed and benchmark algorithms. The plots in Fig. 4.3 (a) and (b), in turn, depict the inter-beat-interval errors and pNN50 errors, respectively, for the noisy, as well as proposed and benchmark denoising algorithms for Dataset 1. Finally, for Database 2, Fig. 4.4 depicts kernel fits for the probability distributions of the HR error percentages for the combined training and extended training sub-datasets.

As can be seen from Table 4.2, the proposed denoising algorithm outperforms the benchmark across all investigated metrics and SNR levels. For extremely noisy cases (e.g.,  $SNR = -5$  and

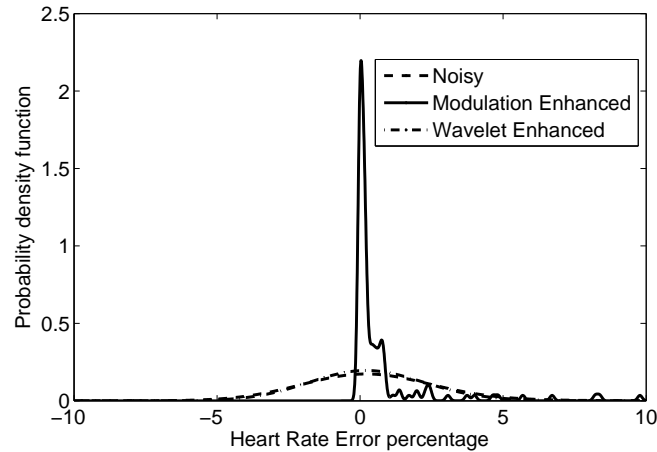


**Figure 4.4 – Kernel fit of probability distributions of HR error percentage for noisy (dash), proposed (line), and benchmark (dash-dot) algorithms for Database 2.**

–10 dB), for example, representative of a low-cost device used during running, the average SNR improvement of the proposed algorithm was of 11 dB, relative to the 6.8 dB improvement achieved with the benchmark. The average HR error percentage over different heart rates and HF/LF ratios was also nearly a third of that achieved by the benchmark. An average  $\kappa$  increase over the noisy signal of 4 was obtained with the proposed algorithm, thus outperforming the subtle increase of 0.1 obtained with the benchmark. Using the  $\kappa$  threshold of 5 suggested in [25, 28] to indicate good quality ECG, this could be achieved with the proposed solution even in extremely noisy cases (SNR = –10 dB), thus comparing favourably against the benchmark which only achieved this at an SNR = 0 dB. Overall, the proposed solution had a higher  $\kappa$  standard deviation, which seemed to be around 1.6 irrespective of the tested SNR. Despite the higher deviation, the  $\kappa$  increases with the proposed algorithm were significantly higher than those achieved with the benchmark across all SNR levels. By exploring a wide range of heart rates and HF/LF ratios, these findings suggest that the proposed algorithm performs well across a wide range of normal and “abnormal” ECG conditions. It can be seen from the table that for an input  $SNR = -10dB$ , the standard deviation of the HR error percentage was higher than the average. A more in-depth analysis showed that this large variability was due to higher errors obtained with lower heart rate values ( $50 \leq \text{bpm} \leq 80$ ), possibly due to

limitations in the Pan-Tompkins peak detection algorithm [36]. Moreover, an additional comparison was performed with the conventional auto-correlation method, typically used to detect periodicity in noisy signals (i.e., heart rate for the task at hand). While the auto-correlation method was shown to be useful in detecting the heart rate of mildly distorted synthetic ECGs, it performed poorly on very noisy and recorded signals. For example, by applying a peak detection algorithm to the auto-correlation curve, an average heart rate error percentage of 80% was achieved at  $SNR = -10dB$ , thus worse than processing the noisy ECG signal directly.

From plots in Fig. 4.3, in turn, it can be seen that the proposed algorithm also resulted in improved HRV analyses, reducing inter-beat-interval and pNN50 errors relative to the noisy signal. Relative to the benchmark, gains of 2.6% and 15% were achieved, respectively. Moreover, gains were most significant at extremely low SNR values, thus showing the advantages of the proposed algorithm for fitness/athletic applications. As an example, in [111], the pNN50 metric was used to quantify differences in highly qualified athletes and non-athletes. It was found that pNN50 percentage of endurance training athletes (e.g., long-distance running, polyathlon) was 15.2 higher than the controls, whereas with strength training athletes (e.g., weightlifting, power-lifting), it was 11.5 lower than the non-athlete controls. As can be seen from Fig. 4.3 (b), however, noisy signals and wavelet enhancement result in pNN50 measurement errors between 20-30%, thus would be problematic for such task. The pNN50 errors attained with the proposed algorithm, however, would still allow for useful athlete vs non-athlete comparisons even at SNRs as low as -10 dB. Lastly, regarding Database 2, Fig. 4.4 shows the advantages of the proposed algorithm with low-quality ECGs recorded in realistic scenarios. The HR error percentage achieved with the proposed algorithm was concentrated around zero with a standard deviation of approximately 1%. The noisy and wavelet-

enhanced methods, on the other hand, presented a much wider estimation error variability with a standard deviation of approximately 8%.

Lastly, it is important to emphasize that the proposed enhancement algorithm has some limitations and room for further improvements. First, as it relies on modulation domain filters of length 101, thus corresponding to a processing “window” of approximately 3 seconds. As such, it assumes that the heart rate will not vary faster than this filtering window. Notwithstanding, given the bandwidth of the filters being set to 0.625 Hz around  $f_c$ , this provides room for heart rate changes of approximately  $\pm 18.75$  bpm. We have found that this variability within 3 seconds suffices to cover heart rate changes within the applications we are targeting, as in athletes it has been documented that heart rate changes during endurance training are of approximately 40 bpm within 2 minutes [112, 113], and much slower during recovery. Broader bandwidths or shorter filters may be explored if faster heart rate changes are expected within this time window, but at the cost of reduced performance. Second, since we are using FIR filters, a 50-sample phase shift (approximately 1.6 seconds) is needed for signal reconstruction, thus limiting real-time processing. For the targeted application this was not an issue, but alternate filter structures and phase estimation strategies could be explored to further reduce this delay. Lastly, the computational time of the proposed algorithm was roughly twice that of the benchmark in the “worst case” scenarios involving low bpm values, as more bandpass filters were needed. Processing speed gains can be attained if a lower number of bandpass filters are used, thus trading-off accuracy and computational time. Moreover, since the Matlab codes implemented herein have not been optimized for processing time, further reductions may still be attained. Overall, it is believed that the gains in ECG enhancement obtained with the proposed algorithm over the benchmark outweigh these limitations, thus making it an ideal candidate for ECG enhancement for non-clinical applications.

## 4.5 Conclusion

In this chapter, a new method for denoising ECGs was proposed based on spectro-temporal filtering. Comparisons with a state-of-the-art wavelet based enhancement algorithm showed the proposed method outperforming the benchmark across several figures of merit, particularly in extremely noisy scenarios. In particular, the proposed method improved SNR by around 11 dB, resulted in  $HR_{error}$  percentage of 2%, compared to 57% with the noisy signal and 6% with the wavelet-enhanced ECG. Moreover,  $\kappa$  measurements were higher with the proposed algorithm across all tested SNR levels, thus suggesting improved quality over the benchmark. The proposed solution was shown to not only improve SNR,  $\kappa$ , and HR estimation, but to also improve heart rate variability measurement, thus opening doors for accurate analysis of ECG data collected with low-cost devices in the field. Further investigation is still needed to validate such findings in a strictly clinical setting involving e.g., abrupt changes in heart rate such as arrhythmia absolute in atrial fibrillation or significant ventricular entropy.



## Chapter 5

# Spectro-Temporal ECG Analysis for Noise-Robust HRV Measurement

### 5.1 Preamble

This chapter contains material extracted from publication #6 listed in Section 1.3.

### 5.2 Introduction

Despite the method used to measure HRV, one commonality between all methods is their sensibility to ECG artifacts, particularly movement artifacts. Such limitations have been reported for time [114] and frequency domain [115] measures, as well as non-linear ones [116]. Erroneous HRV measurements

resultant from noisy ECG signals can have severe detrimental effects, including a rise in false alarms in automated health monitoring devices [117]. A common practical approach taken to alleviate this shortcoming is to perform ECG enhancement (i.e., artifact removal) prior to HRV index calculation [45] as shown in Chapter 2, Section 2.3. Typically, wavelet-based enhancement algorithms have been used for this purpose [101, 118]. However, alternate strategies are still needed as i) ECG enhancement algorithm performance is still limited in very noisy settings, as shown in Chapter 4, and ii) emerging wearable-based applications require low computational overhead, thus bypassing the need for ECG enhancement prior to HRV measurement. Hence, the goal of this chapter is to propose an innovative method of measuring HRV that is robust to ECG artifacts, even in very noisy cases. While the previous chapter has shown that modulation-domain enhancement prior to HRV computation can help improve HRV measurement accuracy, such an approach still requires several stages of processing, including enhancement, RR peak detection (e.g., Pan-Tompkins algorithm) and HRV calculation, with each stage introducing potential errors to the final task at hand. The proposed representation, however, lends itself well to measuring HRV directly from the modulation domain, without the need for enhancement or peak detection.

More specifically, the proposed metric, termed modulation-domain HRV (MD-HRV), is shown to accurately estimate the heart rate (and consequently HRV) in extremely noisy cases on both synthetic and recorded signals, and to outperform several existing HRV metrics computed after wavelet-based enhancement. These findings suggest that MD-HRV can be a useful metric for medical and non-medical applications involving noisy ECGs.

The remainder of this chapter is organized as follows. Section 5.3 provides a description of the ECG modulation spectral representation, the proposed MD-HRV metric, benchmark HRV met-

rics, and performance figures-of-merit. Experimental results are then presented in Section 5.4 and discussed in Section 5.5. Finally, conclusions are drawn in Section 5.6.

### 5.3 Modulation Domain HRV Measurement

As outlined in Chapter 3, the spectro-temporal ECG representation allows distinguishing modulation spectral components even in extremely noisy scenarios, as depicted in Figure 5.1 for an ECG signal with 120 bpm and at  $SNR = -10dB$ . Here, we propose a new modulation-domain HRV metric (MD-HRV). In order to compute the metric, the central frequency (i.e., first lobe) within each per-frame modulation spectrogram  $\mathcal{X}(f, f_{m,k})$  has to be detected; this is represented by the shaded lobes in the modulation spectrograms of Figure 2.8. For this purpose, the energy for each modulation frequency bin is calculated between the  $0 \leq f \leq 40$  region where most of the ECG energy is concentrated. The modulation frequency bin with the highest energy between  $0.8 \leq f_m \leq 3.3$  is selected as the center of the first lobe. The  $f_m$  range was chosen to cover heart rates between 48 and 198 bpm, thus encompassing different cardiac diseases and activity levels. Next, the standard deviation of the per-frame central frequencies is calculated. For the sake of notation, let  $\mathcal{X}_k = \mathcal{X}(f, f_{m,k})$ , thus the MD-HRV over all per-frame modulation spectrograms is computed as:

$$MD-HRV = \sqrt{\frac{1}{N-1} \sum_{k=1}^N (\mathcal{X}_k - \bar{\mathcal{X}})^2}, \quad (5.1)$$

where  $N$  is the total number of ‘modulation frames’,  $\mathcal{X}_k$  is the central frequency at the  $k^{th}$  modulation frame, and  $\bar{\mathcal{X}}$  is the mean central frequency calculated over all per-frame modulation spectrograms. Here, modulation spectrograms are estimated every 5 seconds with 75% overlap.

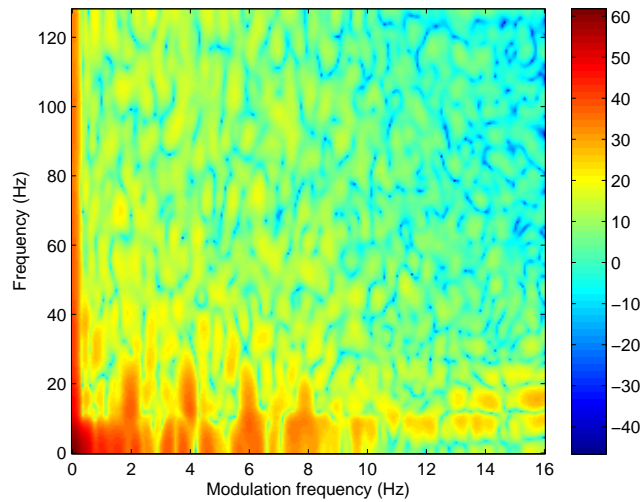


**Figure 5.1 – Modulation spectrogram of synthesized ECG with 120 bpm and at  $\text{SNR} = -10$  dB. The color bar shows the range values in dB.**

### 5.3.1 Dataset 1: Synthetic ECG

Synthetic ECG signals were generated using the ‘ecgsyn’ function in Matlab<sup>TM</sup> available in Physionet [21] as described in Chapter 2, Section 2.1.3. Here, in total 700 signals of 10-minute duration sampled at 256 Hz were generated by randomly sampling the heart rate standard deviation between 1 and 10 bpm for heart rates ranging from 50 to 180 bpm. Clean synthetic signals were corrupted by several artifacts at known SNR levels. Noisy signals were generated at 6 SNR levels of  $-10$  dB,  $-8$  dB,  $-5$  dB,  $0$  dB,  $5$  dB, and  $10$  dB. Overall, 4200 noisy 10-minute signals (700 hours) were generated for HRV metric assessment.

### 5.3.2 Dataset 2: MIT-BIH Arrhythmia Dataset

In order to test the proposed HRV metric in realistic pathological signals, the MIT-BIH Arrhythmia database was also used [42]. For the experiments described herein, the two-channel signals were

segmented to create 10-minute segments downsampled at 256 Hz. Thus, a total of 288 10-minute segments were created providing an overall of 48 hours for testing. These segments were then grouped according to the heart rate (HR) and heart rate standard deviation (sdHR), similar to the synthetic ECG signals, thus allowing for easier comparison between the two databases. Hence, four groups were found: Group 1 ( $60 \pm 10$ bpm), Group 2 ( $80 \pm 10$  bpm), Group 3 ( $100 \pm 10$  bpm), and Group 4 ( $120 \pm 10$  bpm).

### 5.3.3 Benchmarks and Figures-of-Merit

In order to compare the proposed MD-HRV metric with “gold standard” benchmarks, several time domain, frequency domain, and non-linear HRV metrics, as shown in Chapter 2, Section 2.2.1, were computed from the *clean* ECG signals. Time-domain HRV metrics include i) SDNN, ii) SDANN, and iii) stdHR. The frequency-domain metric, in turn, measures the total spectral power contained in all frequency sub-bands such as VLF, LF, and HF. Lastly, non-linear Poincaré plots are used with the so-called SD1 and SD2 parameters [43].

Moreover, a wavelet-based ECG enhancement algorithm [44] was used for artifact removal prior to benchmark HRV measurement. Such setup exemplifies the process used in existing state-of-the-art HRV monitoring applications [45]. Here, comparisons will be made between the proposed MD-HRV metric computed from the *noisy* signal and benchmark HRV metrics computed from the *noisy* and *enhanced* signals. Based on experiments in Chapter 4 and insights from [34], Daubechies-6 mother wavelets with 8 levels of decomposition, combined with soft thresholding and universal shrinkage were used [46]; such settings resulted in the best enhancement performance on the two datasets used herein.

As for figures-of-merit, Pearson ( $\rho$ ) and Spearman ( $\rho_s$ ) correlations were used to gauge the benefits of the proposed MD-HRV metric. Due to the availability of the original clean synthetic signal and the annotation files for the arrhythmia dataset, the proposed metric could be compared with ‘ground truth’ benchmark HRV values. Pearson correlation shows the linear relationship between MD-HRV and the ‘true’ HRV metrics. Spearman correlation, in turn, measures how well MD-HRV ranks against the ‘true’ metrics. Higher correlation values correspond to improved metrics. Additionally, to evaluate the bias and to estimate an agreement interval between metrics, Bland-Altman plots were also used [47]. A Bland-Altman plot depicts the differences (vertical axis) against the averages (horizontal axis), hence, are used to verify the level of agreement between the ‘true’ metrics and the proposed MD-HRV [48]. Typically, Bland-Altman plots with a more compact point distribution around zero (vertical axis) represent metrics in better agreement. Lastly, linear regression analysis is also performed to show the linear fitting with confidence intervals at 95%; smaller confidence intervals represent more reliable metrics.

## 5.4 Results

Tables 5.1 and 5.2 show the performance comparison for the different HRV metrics calculated from the noisy signals, their enhanced wavelet counterparts, and the proposed MD-HRV metric for datasets 1 and 2, respectively. The Pearson ( $\rho$ ) and Spearman ( $\rho_s$ ) correlations were obtained between the ‘true’ benchmark HRV metrics for clean signals (i.e., SDNN, SDANN, sdHR, total power, SD1, and SD2) and HRV metrics for noisy and enhanced signals, as well as between the ‘true’ metrics and the proposed MD-HRV. The results reported in the tables correspond to the average over the four groups, as described in Section 5.3.2.

Table 5.1 – Performance comparison ( $\rho$  and  $\rho_S$ ) of HRV metrics for noisy signals, wavelet enhanced signals, and the proposed MD-HRV metric for Dataset 1 at different SNR level.

SDNN						
Input SNR (dB)	Noisy		Enhanced		MD-HRV	
	$\rho$	$\rho_S$	$\rho$	$\rho_S$	$\rho$	$\rho_S$
-10	0.221	0.201	0.439	0.447	0.781	0.837
-8	0.505	0.480	0.615	0.626	0.924	0.932
-5	0.896	0.900	0.852	0.854	0.969	0.971
0	0.912	0.912	0.965	0.965	0.979	0.984
5	1.000	0.999	0.976	0.977	0.988	0.992
10	1.000	1.000	1.000	1.000	0.990	0.993
SDANN						
Input SNR (dB)	Noisy		Enhanced		MD-HRV	
	$\rho$	$\rho_S$	$\rho$	$\rho_S$	$\rho$	$\rho_S$
-10	0.271	0.273	0.443	0.449	0.751	0.824
-8	0.541	0.522	0.650	0.657	0.915	0.925
-5	0.920	0.919	0.859	0.860	0.962	0.967
0	0.944	0.943	0.970	0.972	0.970	0.977
5	0.994	0.993	0.985	0.986	0.980	0.985
10	0.996	0.995	0.998	0.998	0.982	0.987
sdHR						
Input SNR (dB)	Noisy		Enhanced		MD-HRV	
	$\rho$	$\rho_S$	$\rho$	$\rho_S$	$\rho$	$\rho_S$
-10	0.225	0.207	0.285	0.292	0.762	0.830
-8	0.537	0.522	0.494	0.522	0.924	0.931
-5	0.883	0.906	0.836	0.866	0.969	0.969
0	0.989	0.989	0.991	0.992	0.980	0.984
5	0.999	0.999	0.996	0.996	0.990	0.992
10	0.999	0.999	0.999	0.999	0.991	0.993
SD1						
Input SNR (dB)	Noisy		Enhanced		MD-HRV	
	$\rho$	$\rho_S$	$\rho$	$\rho_S$	$\rho$	$\rho_S$
-10	0.156	0.150	0.407	0.413	0.757	0.824
-8	0.443	0.402	0.562	0.568	0.916	0.923
-5	0.821	0.826	0.794	0.795	0.963	0.964
0	0.802	0.808	0.906	0.908	0.973	0.976
5	0.969	0.993	0.887	0.895	0.981	0.984
10	0.993	0.994	0.999	0.999	0.983	0.985
SD2						
Input SNR (dB)	Noisy		Enhanced		MD-HRV	
	$\rho$	$\rho_S$	$\rho$	$\rho_S$	$\rho$	$\rho_S$
-10	0.267	0.256	0.450	0.461	0.759	0.829
-8	0.528	0.512	0.638	0.647	0.921	0.931
-5	0.917	0.927	0.864	0.869	0.963	0.967
0	0.952	0.952	0.980	0.980	0.974	0.980
5	0.998	0.996	0.991	0.992	0.982	0.987
10	0.998	0.997	1.000	1.000	0.984	0.988
Total power (AR)						
Input SNR (dB)	Noisy		Enhanced		MD-HRV	
	$\rho$	$\rho_S$	$\rho$	$\rho_S$	$\rho$	$\rho_S$
-10	0.194	0.201	0.346	0.383	0.711	0.802
-8	0.423	0.457	0.524	0.552	0.871	0.908
-5	0.803	0.843	0.760	0.808	0.908	0.945
0	0.791	0.842	0.889	0.904	0.918	0.959
5	0.921	0.970	0.922	0.934	0.926	0.967
10	0.924	0.971	0.998	0.998	0.928	0.968

**Table 5.2 – Performance comparison ( $\rho$  and  $\rho_S$ ) of HRV metrics for noisy signals, wavelet enhanced signals, and the proposed MD-HRV metric for Dataset 2.**

HRV metrics	Noisy		Enhanced		MD-HRV	
	$\rho$	$\rho_S$	$\rho$	$\rho_S$	$\rho$	$\rho_S$
SDNN	0.632	0.837	0.617	0.844	0.893	0.830
SDANN	0.687	0.816	0.641	0.809	0.899	0.814
sdHR	0.608	0.759	0.616	0.778	0.902	0.834
SD1	0.675	0.828	0.632	0.820	0.908	0.734
SD2	0.611	0.820	0.601	0.841	0.879	0.817
Total Power (AR)	0.452	0.826	0.281	0.819	0.893	0.800

Figures 5.2 (a)-(c) further depict the scatterplots (and linear fit curves) of the sdHR metric computed from the noisy (subplot a) and enhanced signals (subplot b), as well as the MD-HRV metric computed from the noisy signals (subplot c). To avoid cluttered plots, only 100 noisy signals at 100 bpm and SNR= $-10$  dB are shown, thus representing scenarios similar to high levels of exercise and movement. Furthermore, Figures 5.3 (a)-(c) show the Bland-Altman plots for the three cases mentioned above, respectively.

Lastly, Figures 5.4 and 5.5 show the scatterplots and Bland-Altman plots for Group 2 ( $80 \pm 10$  bpm) in dataset 2, respectively. As above, the sdHR benchmark metric computed from the noisy signal, the enhanced signal, as well as the proposed MD-HRV metric computed from the noisy signal are shown in the plots. It is clear from the plots that the proposed MD-HRV metric results in higher correlations, tighter regression confidence intervals, and more compact Bland-Altman plots around zero (vertical axis) than the sdHR benchmark metric in both cases with and without wavelet enhancement.

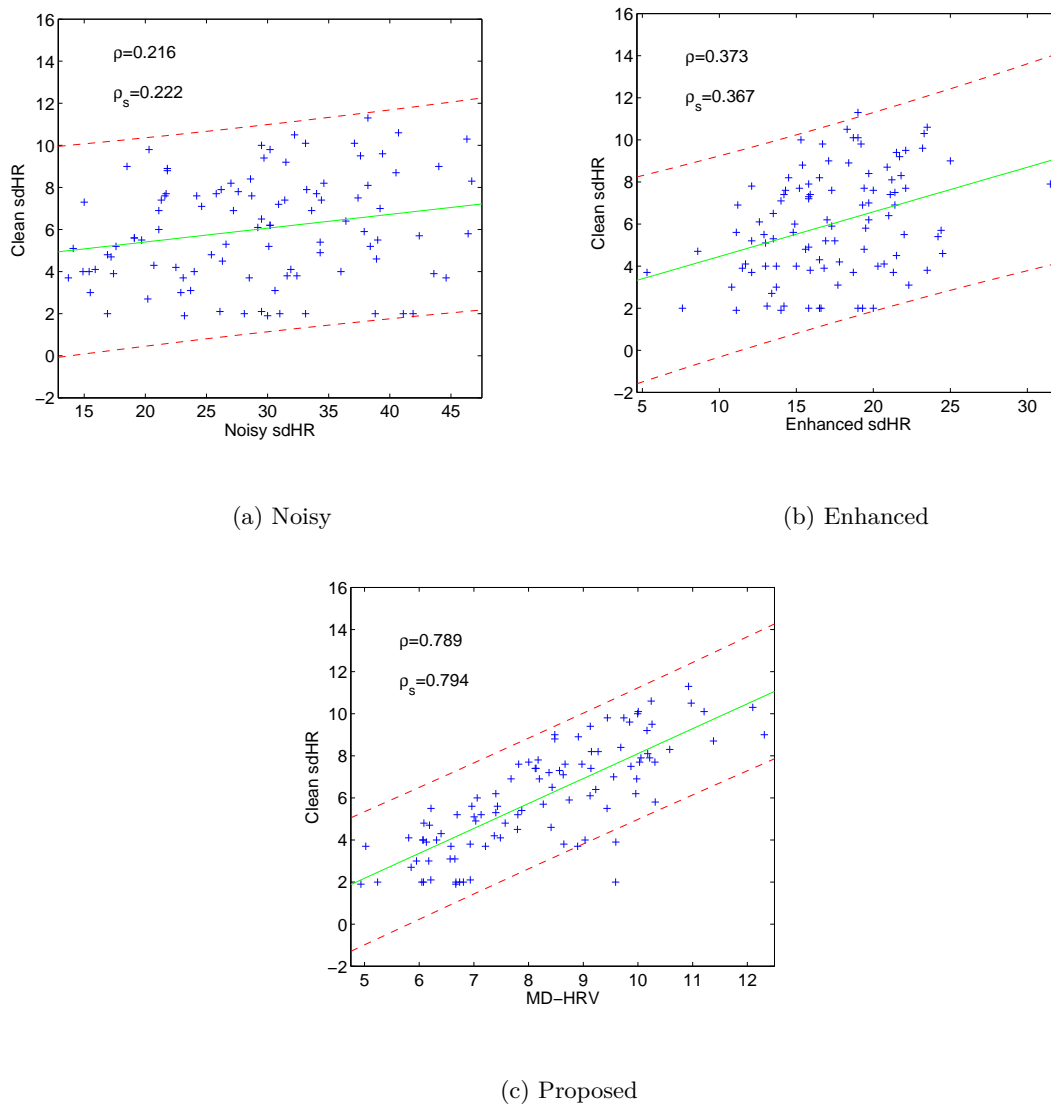
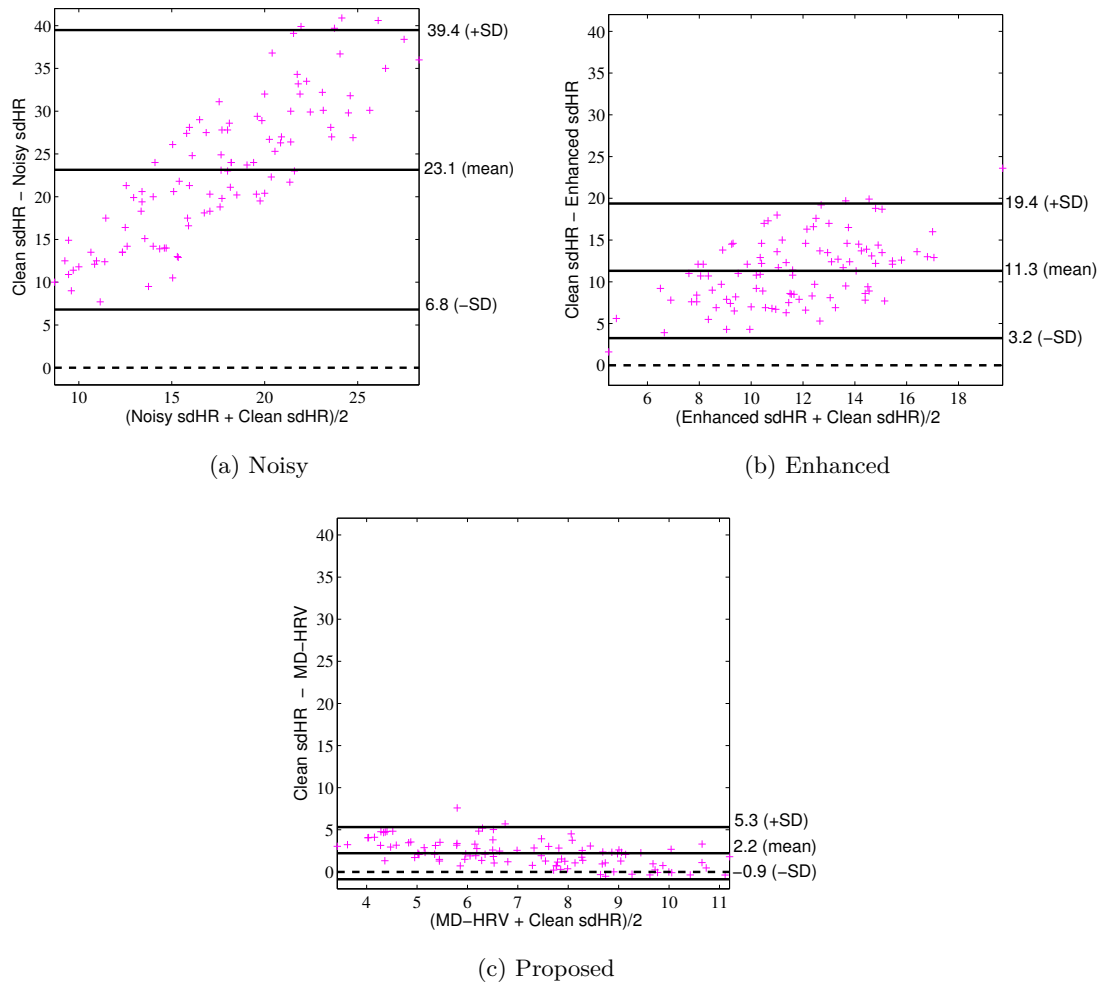


Figure 5.2 – Scatterplots for noisy ECG signals with 100 bpm and  $\text{SNR} = -10$  dB between (a) ‘true’ sdHR and noisy sdHR, (b) ‘true’ sdHR and wavelet enhanced sdHR, and (c) ‘true’ sdHR and proposed MD-HRV.

## 5.5 Discussion

In this chapter, a new noise-robust HRV metric was proposed based on a spectro-temporal ECG representation termed ‘modulation spectrum.’ The goal of the metric was to reliably measure HRV in extremely noisy settings, without the need for a priori ECG enhancement or peak detection for RR analyses. The proposed metric was compared to six benchmark HRV indices computed using



**Figure 5.3** – Bland-Altman plots for noisy ECG signals with 100 bpm and SNR =  $-10$  dB between (a) ‘true’ sdHR and noisy sdHR, (b) ‘true’ sdHR and wavelet enhanced sdHR, and (c) ‘true’ sdHR and proposed MD-HRV.

time-domain, frequency-domain and non-linear methods reported in the literature, with and without ECG enhancement.

From Table 5.1, it can be seen that benchmark HRV metrics computed from noisy synthetic signals are generally well correlated with the true HRV values computed from the clean ECG signals for SNR levels greater than 0 dB. For extremely low SNR levels below  $-5$  dB, however, typical of those observed with wearables during intense exercise as shown in publication #2, HRV

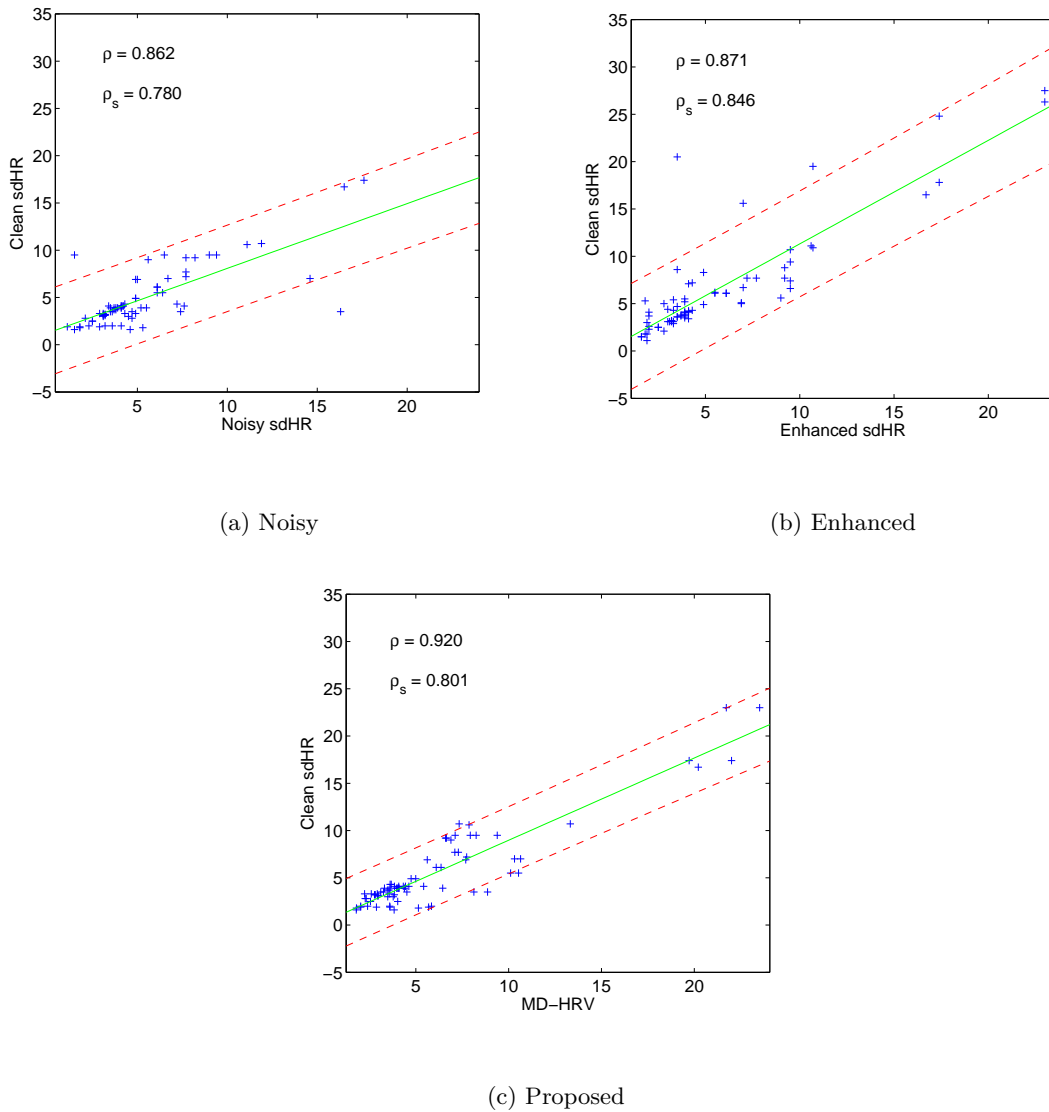
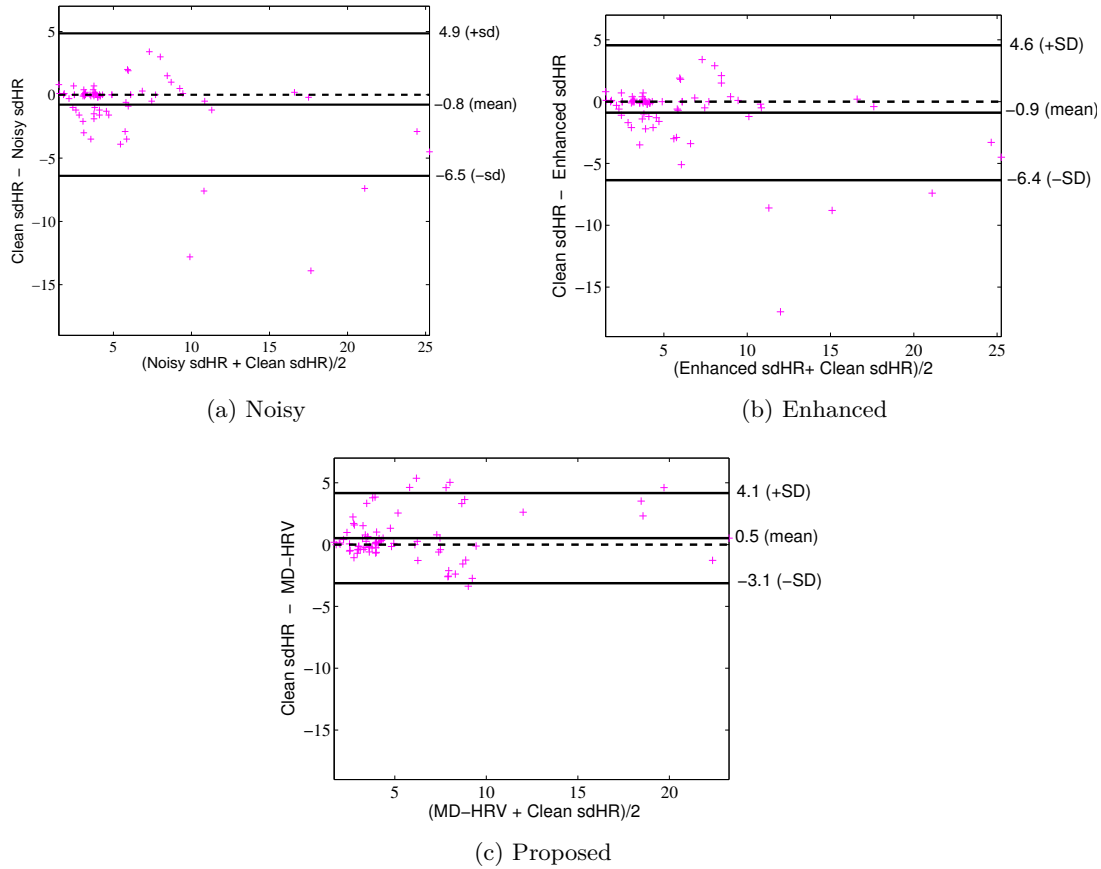


Figure 5.4 – Scatterplots for Group 2 in Dataset 2 for (a) Noisy sdHR and ‘true’ sdHR, (b) Wavelet enhanced sdHR and ‘true’ sdHR, and (c) Proposed MD-HRV and ‘true’ sdHR.

measurement accuracy degrades quickly. Wavelet-based enhancement, in turn, was shown to be useful for most metrics, particularly for SNRs below  $-8$  dB.

The proposed MD-HRV metric, on the other hand, computed only from the *noisy* ECG signal, showed stable correlation values generally greater than 0.9 up to an SNR =  $-8$  dB, with a drop to around 0.71–0.76 at an SNR =  $-10$  dB. In this extremely noisy scenario, it was difficult to accurately detect the main lobe in the modulation spectrogram (corresponding to the heart rate, see Chapter 3),



**Figure 5.5 – Bland-Altman plots for Group 2 in Dataset 2 for (a) Noisy sdHR and ‘true’ sdHR, (b) Wavelet enhanced sdHR and ‘true’ sdHR, and (c) Proposed MD-HRV and ‘true’ sdHR.**

thus compromising HRV measurement. Notwithstanding, it can be seen that with the SDNN metric, while wavelet enhancement improved  $\rho$  by about 99% relative to the noisy case, the proposed metric outperformed the noisy case by 253%. Similar gains were seen across all of the benchmark metrics, including SDANN (177% compared to 63% post enhancement), sdHR (239% compared to 27% post enhancement), SD1 and SD2 (385% and 184% compared to 161% and 68% post enhancement, respectively), and total power (266% compared to 78% post enhancement). Overall, the correlation values obtained with the MD-HRV metric at an SNR =  $-10$  dB are inline with those obtained with the benchmark metrics *post* enhancement at  $-8 \text{ dB} \leq \text{SNR} \leq -5 \text{ dB}$ . Closer inspection showed that the total power HRV benchmark metric resulted in the lowest correlation with MD-HRV across all

tested SNR levels. Interestingly, this benchmark metric showed to be the most sensitive to artifacts, and resulted in the lowest correlation values of all benchmark metrics even for SNR= 10 dB.

These results are further validated from the scatter and Bland-Altman plots shown in Figures 5.2 and 5.3, respectively, for the proposed and sdHR (pre and post enhancement) metrics; plots correspond to 100 randomly-selected ECG signals at 100 bpm and an SNR= -10 dB. The Bland-Altman plots, for example, show that the discrepancies between the true sdHR (computed from the clean signals) and the sdHR computed from the wavelet enhanced signals had a mean difference of  $11.3 \pm 8.1$ , whereas this difference was of  $2.2 \pm 3.1$  for the proposed MD-HRV metric computed from the noisy signals. Overall, results from Table 5.1 and Figures 5.2 and 5.3 suggest that the proposed metric could be useful in extreme conditions where wearable ECG signals are highly contaminated with motion artifacts, such as during peak performance training.

Table 5.2, in turn, reported results obtained from ambulatory recorded pathological ECG data. Relative to Table 5.1, the correlation values suggest a fair amount of noise is present in the recordings. Interestingly, wavelet based enhancement did not result in performance improvements for most of the benchmark metrics, thus highlighting the limitations of existing enhancement algorithms for data recorded in real-world settings. Notwithstanding, the proposed metric achieved reliable results without the need for a priori enhancement; overall,  $\rho$  and  $\rho_S$  values stayed between 0.8 – 0.9 for all six benchmark metrics. Overall, an average gain in  $\rho$  of approximately 49% was observed with the proposed MD-HRV metric over the wavelet-enhanced case. As in the case for synthetic ECG signals, the frequency-domain HR benchmark metric showed to be the most sensitive to artifacts. In fact, for Dataset 2, wavelet enhancement deteriorated benchmark HRV measurement performance, likely due to the introduction of additional unwanted artifacts post enhancement. As with the synthetic

signals, the scatter and Bland-Altman plots in Figures 5.4 and 5.5 show smaller confidence intervals and tighter distributions around the null bias, respectively. Overall, the proposed MD-HRV metric achieved a mean difference of  $0.5 \pm 3.6$  with the true sdHR computed from the original heart rate labels, thus comparing favourably to the  $-0.9 \pm 5.5$  obtained with the wavelet enhanced benchmark metric. These findings suggest that the proposed metric is not only robust to noise, but also to different cardiac pathologies, thus is an ideal candidate for patient monitoring with ambulatory ECGs.

## 5.6 Conclusion

This chapter has proposed a new method of estimating HRV in extremely noisy settings. The metric is based on the spectro-temporal representation of the ECG signal, commonly termed “modulation spectral” representation. The proposed metric, termed MD-HRV (modulation domain HRV), was extensively tested using both synthetic and recorded noisy ECG signals, and compared to six benchmark HRV metrics computed from the noisy, as well as enhanced ECG signals, which had artifacts removed using a state-of-the-art wavelet-based algorithm. MD-HRV, computed from the noisy signal, was shown to outperform benchmark metrics computed from the enhanced signals across different figures-of-merit, thus showing the potential of the metric for HRV measurement in extreme conditions with low-cost portable devices.

## Chapter 6

# Towards Quality-Aware Telehealth

## Applications

### 6.1 Preamble

This chapter contains material extracted from publication #8 listed in Section 1.3.

### 6.2 Introduction

In telehealth applications data is either streamed or stored on the wearable ECG device, which typically has limited storage capability. If unusable data is stored or transmitted, this leads to unnecessary battery loss, bandwidth usage, or storage losses. A quality-aware solution based on the

proposed MS-QI that would overcome this limitation is proposed in this chapter. The benefits are shown to be two-fold. First, a quality-aware transmission scheme is shown to save energy, bandwidth and storage space by avoiding the transmission of “unusable” ECG signals. Second, the MS-QI measure is shown to accurately represent different activity states, thus enabling an activity-aware telehealth application which could have potential application for athlete monitoring.

To achieve our goals, we test three classifiers to discriminate between usable and unusable ECG signals. More specifically, linear discriminant analysis (LDA) and support vector machine (SVM) classifiers were investigated, as well as a manual thresholding (MT) method based on threshold previously reported in the literature. The LDA and SVM classifiers are trained on synthetic ECG signals and all three methods are tested on unseen signals collected with three different systems: (1) a 12-lead portable ECG device, (2) a 2-lead ambulatory ECG recorded from arrhythmia patients, and (3) a single-lead textile ECG system. Experimental results show the proposed classifiers outperforming benchmark ones trained on ECG kurtosis features, which are typically used today to measure ECG quality [9].

The remainder of this chapter is organized as follows. Section 6.3 describes the classification strategies used in this study as well as benchmark features, datasets, and performance assessment metrics. Experimental results are then presented and discussed in Section 6.4. Finally, chapter conclusions are drawn in Section 6.5.

## 6.3 Classification Strategies

Both LDA and SVM classifiers were built using the statistics toolbox in Matlab. LDA is a method for finding a linear combination to separate two or more classes of objects. It has continuous independent variables (normally distributed) and categorical dependent variables known as class labels. Different classes are based on different Gaussian distributions to generate data. In the training step, parameters corresponding to Gaussian distributions for each class are estimated. In the prediction step, the new data is classified with the smallest misclassification cost. On the other hand, SVM performs a mapping to a higher dimension using a kernel that allows for a hyperplane to separate the data. Since both classifiers have been widely used, a complete description is beyond the scope of this thesis and the interested reader is referred to [49] for more details on LDA classifiers and [50] for an in-depth description of SVM. On the other hand, the manual thresholding method uses previously-reported values to discriminate between ‘good’ and ‘bad’ quality signals. More specifically, for the MS-QI metric, a threshold of 0.5 was used, as per insights from Chapter 3 and Fig. 3.5. For the kurtosis benchmark metric, in turn, a threshold of  $\kappa = 5$  was used [28] to discriminate between low ( $\kappa < 5$ ) and high ( $\kappa \geq 5$ ) quality ECGs.

### 6.3.1 Benchmark Features and Feature Fusion

ECG signal kurtosis ( $\kappa$ ), i.e., a statistical measure of the peakedness of the signal, has been widely used as a measure of signal quality ([26], [25]). As such, LDA and SVM classifiers are also trained on  $\kappa$  features and used as a benchmark to gauge the benefits of using the MS-QI features. In order to investigate the potential complementarity of the MS-QI and  $\kappa$  features, we investigate the benefits

of feature fusion, where LDA and SVM classifiers were trained with the combined feature sets. The ECG and  $\kappa$  data were normalized by using standard deviation to [0,1] before fusion and training. Lastly, the MT classification strategy was tested with the thresholds mentioned above for both features MS-QI and  $\kappa$  in order to be compared to the machine learning methods.

### 6.3.2 Training Dataset: Synthetic ECG

Synthetic ECG signals were generated and contaminated by several SNR levels as described in Chapter 2, Section 2.1.3. We generated 200 signals of 120-second duration each. The signals were generated by randomly sampling two parameters, namely heart rate uniformly over the 50-180 beats per minute range, and the LF/HF ratio uniformly over the 0.5 to 8.9 range as in Chapter 3, Section 3.3.1. Noisy ECG signals were generated at SNRs of  $-5$  dB, 0 dB, 5 dB, 15 dB, and 30 dB. For classifier training, noisy ECG with SNR equal to  $-5$  dB, 0 dB and 5 dB were labelled as “unusable”, whereas the clean ECG signals along with the noisy ones at 15 dB and 30 dB SNR were labelled as “usable”. This choice allowed for 600 unusable and 600 usable ECG signals to be used for classifier training.

### 6.3.3 Test Dataset 1: Physionet Challenge Signal Quality Database

A subset of the ECG signals from Physionet/Computing in Cardiology 2011 Challenge dataset [23] were used as unseen test data. The dataset consists of 12-lead ECG signals collected at a 500 Hz sample rate. The signals were classified as “acceptable” or “unacceptable” by a group of experts as

described in Chapter 3, Section 3.3.3. For the experiments described herein, 71 good quality and 71 bad quality signals, each with 10-second duration, were used.

#### **6.3.4 Test Dataset 2: Recorded Ambulatory ECG Data**

ECG recordings from the Physionet MIT-BIH Arrhythmia Database [24] from 47 subjects were used as unseen test data. The signals are two-channel recordings sampled at 360 Hz. Signal quality labels (i.e., “noisy” and “clean” segments) were annotated by cardiologists as described in Chapter 3, Section 3.3.4. We selected 62 clean and 65 noisy ECG segments with 2-minute duration each.

#### **6.3.5 Test Dataset 3: Textile ECG Data from Hexoskin Garment**

ECG signals recorded from Hexoskin garment were used as unseen data. The garment allows 150+ hours of standalone recording and measures heart rate, heart rate variability to estimate stress and fatigue, heart rate recovery, ECG, breathing rate (RPM), minute ventilation (L/min), activity intensity, peak acceleration, steps, cadence and sleep positions. The garment streams the data to a mobile device via low power Bluetooth wireless communication, as well as to the cloud, thus enabling more advanced biosignal analysis to be performed in quasi real-time as described in Chapter 3, Section 3.3.2.

Single channel ECG signals were collected during three different activities: sitting, walking, and running, totaling 15 minutes. Data was collected from three participants. The signals were sampled at 256 Hz with 12-bit resolution. The three different activities can be identified depending on the

actimetry level values. Actimetry level between 0 and 50 corresponds to sitting, around 100 to walking, and 300 to running. As described in [22], the ECG signal quality is inversely proportional to the actimetry values (e.g., higher ECG quality, lower actimetry level), issue that can be used in telehealth applications to discriminate among different activity levels. In order to investigate the use of ECG quality detection in telehealth applications, one simple system is tested here. Data from test set 3 is used and the trained classifiers are used to label each 5-second excerpts as usable or unusable. Only data streams deemed usable would be sent in a real setting, thus resulting in energy, bandwidth and storage savings.

### 6.3.6 Performance Assessment

Classifier performance is gauged via three commonly-used figures-of-merit: Accuracy (ACC), Sensitivity (SE), and Specificity (SP). These measurements are computed as follows,

$$ACC = \frac{TN + TP}{TN + TP + FN + FP} * 100\%, \quad (6.1)$$

$$SE = TP / (TP + FN) * 100\%, \quad (6.2)$$

$$SP = TN / (TN + FP) * 100\%, \quad (6.3)$$

where TP is the number of the true positives; FN is the number of the false negatives; TN is the number of the true negatives; and FP is the number of the false positives. Within a telehealth

application, we use reduction in transmission bandwidth (or storage capacity) attained, relative to traditional transmission, as a figure of merit.

## 6.4 Results and Discussion

Table 6.1 shows the accuracy/sensitivity/specificity results obtained with the three classifiers. Results are shown for the synthetic ECGs, as well as the unseen test Datasets #1 and #2. The machine learning classifiers were trained on the MS-QI,  $\kappa$ , and fused feature sets. In the synthetic ECG case, 50% of the data is used for classifier training and 50% is left for testing. In the other cases, the entire synthetic ECG training database is used for classifier parameter optimization.

As can be seen, machine learning classifiers trained with the benchmark feature perform well with synthetic ECGs but performance degrades quickly once recorded data is used for testing. The MS-QI feature, on the other hand, showed to be robust to signal measurement modality and outperformed the  $\kappa$  features by as much as  $2\times$  and  $5\times$  in terms of accuracy and specificity. These results suggest that the MS-QI features play a crucial role in telehealth applications, which can have signals highly contaminated by artefacts. Moreover, feature fusion, while substantially improved the  $\kappa$  feature performance, did not improve the accuracy of the MS-QI classifier.

Regarding classifier type, SVMs performed slightly better than the LDA classifiers for the MS-QI features. For both classifiers, the performance remained stable across the tested datasets. For the  $\kappa$  feature, on the other hand, the best classifier depended on the test dataset. For example, for synthetic ECG, an LDA classifier performed best. For recorded data in real-world setting, the SVM performed the best. With the fused feature set, the LDA classifier performed the best. The MT results, in

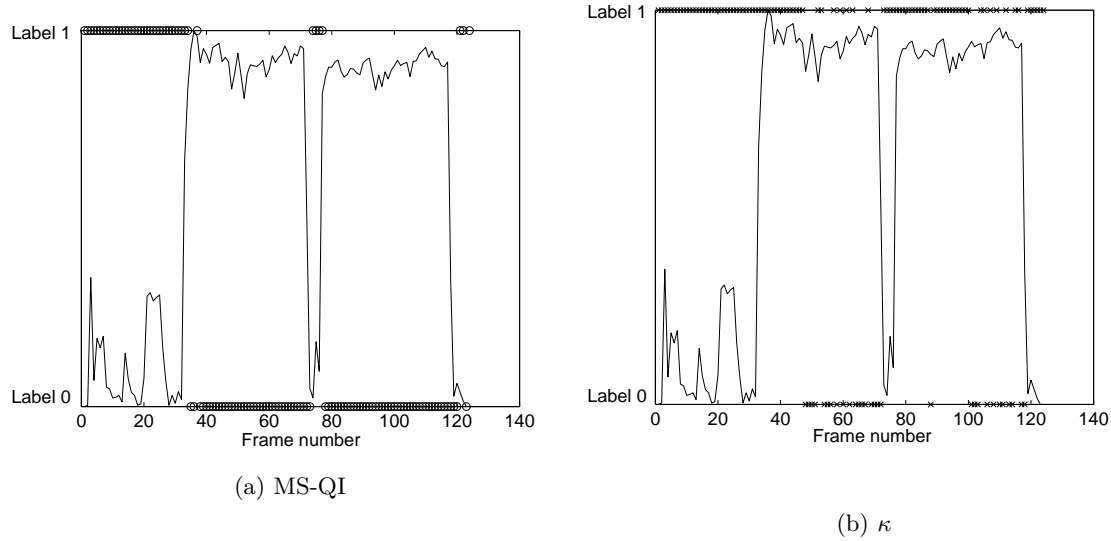
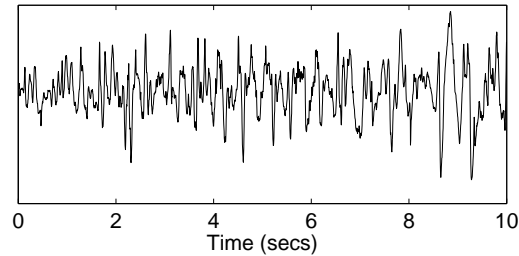


Figure 6.1 – Actimetry profile for one participant of test Dataset 3. LDA classifier decisions are labelled 1 for usable and 0 for unusable using the (a) MS-QI and (b)  $\kappa$  features.

Classifier	Synthetic			Test Dataset 1			Test Dataset 2		
	MS-QI	$\kappa$	Fusion	MS-QI	$\kappa$	Fusion	MS-QI	$\kappa$	Fusion
LDA	97/100/95	96/93/100	98/97/99	95/100/90	54/90/20	75/100/48	100/100/100	68/97/39	75/100/50
SVM	98/99/98	89/100/78	83/100/66	96/100/92	57/84/31	65/100/28	100/100/100	71/93/49	64/100/29
MT	95/99/91	94/100/89	-	100/100/100	50/100/0	-	100/100/100	51/90/14	-

Table 6.1 – Performance comparison of LDA and SVM classifiers trained on MS-QI and  $\kappa$  features, as well as a fusion of both feature sets. Results for the synthetic ECG dataset correspond to training the classifiers with 50% of the data and testing with the remaining 50%. The MT classification strategy was tested in all the datasets as well. Results correspond to accuracy/sensitivity/specificity.

turn, suggest that the MS-QI feature is still robust to the type of ECG data, outperforming the benchmark feature 2x in terms of accuracy. Also, it can be seen that both LDA and SVM classifiers performed slightly better than the MT for synthetic signals in terms of accuracy, and specificity. For test Dataset #1, in turn, the MT methodology was the best. On the other hand, the benchmark feature in the MT method showed to be sensitive to ECG type (see Figure 3.6) as in the machine learning classification results, thus the performance was accurate for synthetic signals and reduced with recorded data.



**Figure 6.2 – Ten-second excerpt from the ECG signal during running.**

In order to test the benefits of quality-aware telehealth transmission, we use test Dataset #3 collected with a textile ECG sensor. Plots in Figures 6.1 and 6.3 show the actimetry profile seen for one participant during the sitting, running, and walking tasks for one machine learning method (LDA) and the MT methodology, respectively. The higher actimetry values are observed during running and in this case resulted in unusable data. Figure 6.2 shows a 10-second excerpt of what the ECG signal looked like during running. As can be seen, PQRST peaks are nonexistent, thus the signal conveys little useful cardiac information. Actimetry levels are calculated from the 3-axis accelerometer and are averaged over 5 second frames.

Overlaid on the actimetry profiles shown in Figures 6.1 (a) and (b) are the output labels obtained with the LDA classifiers trained on MS-QI and  $\kappa$  features, respectively. Label 0 corresponds to unusable data segments whereas label 1 to usable segments. As can be seen, the MS-QI classifiers are able to correctly detect the usable segments and can accurately track running versus not running tasks, thus could potentially be used as an activity level detector for telehealth applications.

In terms of storage savings, for the profile depicted in Figure 6.1, a total 615 seconds is depicted (123 5-second frames). Storage of such data would require  $615 \text{ s} \times 256 \text{ samples/s} \times 12 \text{ bits/sample} \sim 236 \text{ MB}$ . With telehealth applications based on MS-QI classifiers, the storage capacity would be reduced to 210 seconds of usable data, thus resulting in storage savings of 65%. Using the  $\kappa$

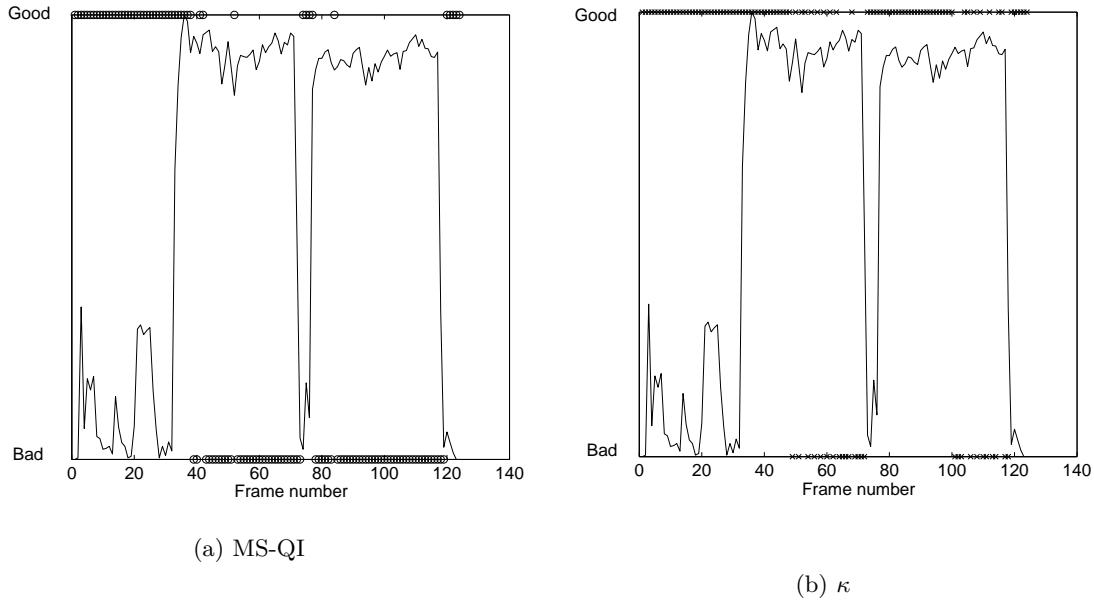


**Figure 6.3 – Actimetry profile for one participant of test Dataset 3. Manual thresholding decisions are labelled ‘Good’ for usable and ‘Bad’ for unusable using the (a) MS-QI and (b)  $\kappa$  features.**

classifiers, on the other hand, would have resulted in 470 seconds of data classified as usable, thus resulting in only a savings of 25%. As can be seen, the proposed quality-aware telehealth application can result in significant storage/transmission gains and potentially result in longer battery lives, two critical aspects in telehealth applications.

The profile depicted in Figure 6.3, in turn, shows the storage savings for the MT method. The storage capacity with the MS-QI feature was reduced to 255 seconds of usable data, resulting in storage savings of 59%. On the other hand, the benchmark feature reported 490 seconds of usable data, thus resulting in storage savings of 21%. These findings suggest that the MS-QI metric combined with machine learning can lead to greater storage savings than the metric combined with a simple manual thresholding method.

## 6.5 Conclusion

This chapter described the use of an ECG quality index for a telehealth application. Two ECG quality indices were explored: the recently-proposed MS-QI measure and the widely-used ECG kurtosis. Experimental results with synthetic and recorded ECG data and linear discriminant and support vector machine classifiers showed the MS-QI feature outperforming the benchmark as well as a fused feature set. Within a context-aware application, ECG storage requirement savings of 65% could be achieved with the MS-QI LDA classifier. A manual thresholding scheme using thresholds published in the literature was also explored and storage savings of 59% could be seen.



## Chapter 7

# Conclusions and Future Research

## Directions

This chapter highlights the conclusions of this thesis and proposes future research directions in the field of ECG signal processing.

### 7.1 Conclusions

Advances in ECG-based telehealth applications have imposed the use of efficient signal processing techniques for accurate diagnosis and user's health characterization. Moreover, portability and the wearable nature of emerging devices have opened doors for alternate applications beyond health diagnostics, including fitness, performance monitoring, quantified self, and athletic endurance, to name a few. As such, several challenges have emerged to guarantee accurate ECG quality needed for

reliable diagnoses, to reduce false alarms in automated systems, as well as reduce the transmission and/or storage of useless corrupted ECG data. To address these issues, this thesis has proposed the use of ECG spectro-temporal representation, termed “modulation spectrum”, which allows accurate separation of ECG modulation spectral components from noise spectral components. By making use of this separation capability, four innovations in the domain of noise-robust ECG processing and applications were developed.

First, a modulation domain quality index (MS-QI) was presented in Chapter 3. The index was tested on synthetic and realistic ECG signals where it outperformed two conventional benchmark quality metrics. It was observed experimentally that the MS-QI values lie between 0 and 1.5, where the index can be used to discriminate between bad (MS-QI close to 0) and good (MS-QI close to 1.5) quality signals as well as to discriminate among different activity levels such as sitting, walking, and running. Hence, MS-QI allows detecting bad quality ECG signals in order to avoid false alarms and erroneous diagnosis about user’s health.

Second, a spectro-temporal filtering method for improved ECG peak detection was proposed in Chapter 4. By utilizing invertible transforms to obtain the spectro-temporal signal representation, filtering can be performed in the modulation spectral domain and the enhanced signal can be reconstructed. Thus, the ECG signal was enhanced using adaptive bandpass FIR filters centred at the main lobe (it relies on the heart rate) and several of its harmonics. The proposed algorithm was tested on synthetic and realistic ECG signals. Experimental results showed the proposed algorithm outperforming a state-of-the-art wavelet-based enhancement algorithm in terms of SNR improvement, heart rate error percentage, kurtosis, and HRV measurement. The obtained findings suggest that the proposed technique is well suitable for lower-cost wearable ECG devices that can

be greatly contaminated by movement artifacts and can be used to enhance the quality of wearable ECG monitors even under extreme conditions, thus it can play a key role in athletic peak performance training/monitoring. However, for applications with limited processing power, having to perform enhancement prior to HRV analysis could be cumbersome, thus a more direct HRV measurement capability is needed as proposed in Chapter 5.

Third, a new HRV index named modulation domain HRV (MD-HRV) was proposed in Chapter 5. The index showed to be noise-robust even in extreme scenarios. The MD-HRV measures the standard deviation of the per-frame modulation spectral components corresponding to the heart rate. It was tested using both synthetic and recorded noisy ECG signals, and compared to six benchmark HRV metrics calculated in time domain, frequency domain, and non-linear methods from clean signals. The proposed metric outperformed benchmark metrics computed from the noisy signals, and enhanced signals using a state-of-the-art wavelet-based algorithm across different figures-of-merit. Therefore, the proposed MD-HRV metric can be computed from the noisy ECG signals without any a prior ECG enhancement, thus showing that it is suitable under extreme noisy conditions with portable ECG devices.

Finally, Chapter 6 presents an application for the MS-QI proposed in Chapter 3. An online ECG quality assessment for telehealth applications was proposed, where the MS-QI was used as a feature for three classifiers (LDA, SVM, and MT). The classifiers were tested to discriminate between “usable” and “unusable” data for quality-aware applications as well as to represent different activity states (e.g., sitting, walking, and running) for activity-aware applications. The MS-QI proposed feature was compared to the widely-used ECG kurtosis using synthetic and real ECG signals. Experimental results with machine learning classifiers showed the MS-QI outperforming the kurtosis

as well as a fused feature set. Gains of 65% could be seen in storage savings by discarding unusable segments of noise-corrupted ECG. These findings were compared to a manual thresholding scheme, which in turn, resulted in 59% storage savings.

## 7.2 Future Research Directions

- **Analysis of the harmonics in modulation domain:** The ECG spectro-temporal representation shows ECG spectral components represented by a main lobe (heart rate) and its harmonics. These spectral components were considered for the MS-QI calculation as well as for the ECG enhancement for peak detection. Also, the main lobe was considered for the proposed MD-HRV metric. However, further analysis can be conducted in studying the harmonics separately, as they may provide information about ECG waveform morphology to detect cardiac pathologies.
- **Complete reconstruction of the ECG signal:** Since ECG components around  $f_m = 0Hz$  are severely affected by noise, they were discarded completely in the spectro-temporal filtering algorithm proposed for improved peak detection at the cost of imperfect reconstruction of the ECG signal. This can lead to issues with diagnostics where perfect QRS complexes, QT segments, ST segments, T waves, and P waves are needed. Therefore, alternate strategies on how to handle the lowpass stationary modulation components are still needed for clinical diagnostic applications (e.g. atrial or ventricular arrhythmia detection, bradycardias, tachycardias, and malfunctions in the heart [15]).
- **Applicability of the MD-HRV metric in detecting diseases:** The proposed MD-HRV metric computed from the noisy signal showed to be highly correlated with time domain,

frequency domain, and nonlinear HRV metrics computed from the clean signal. However, further investigation is still needed to validate the metric in a strictly clinical setting involving e.g., abrupt changes in heart rate to detect cardiac diseases, sudden cardiac death risk, chronic heart failure, and arrhythmias.

- **Embedded algorithm implementation:** The algorithms presented in this thesis were all developed in Matlab. Algorithms were not developed with processing time optimizations in mind, thus further improvements in computational time may be achieved. Moreover, implementations in C and/or embedded systems may further reduce the computational burden. The trade-off between algorithm performance and computational time still needs to be carefully studied.
- **Test the energy efficiency of the proposed quality-aware method within a real-world application:** The proposed MS-QI metric was shown to accurately detect unusable ECG segments, thus reducing the required storage capacity. Similar gains in transmission bandwidth should be attained. Ultimately, however, in remote patient monitoring applications, energy-efficient systems are needed. Further studies are still needed to investigate the tradeoff between the energy consumption for MS-QI calculations vs the energy gains obtained by not transmitting noisy unusable data.
- **Explore proposed modulation frequency analysis tools for other signals:** Recently, multimodal wearable devices are emerging where electromyography (EMG), galvanic skin response, blood volume pulse, and accelerometry sensors are available. We believe that the proposed modulation spectral signal representation can also be useful for such signals. To this end, two exploratory experiments have been conducted. The first has validated the use of the modulation domain analysis of very noisy accelerometry data for gait analysis; more

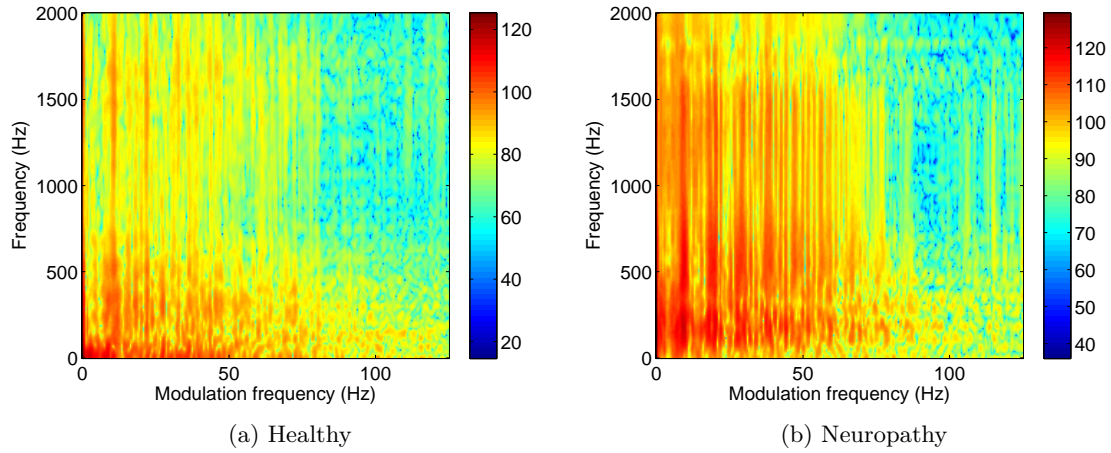


**Figure 7.1** – Modulation spectrograms for (a) a healthy person and (b) a patient with neuropathy.

specifically for gait speed measurement. A manuscript describing these findings is currently in preparation. Second, the modulation spectrogram has been explored for assessment of EMG signals. For illustration purposes, the modulation spectrograms in Fig. 7.1 (a) and (b) are for EMG signals of a healthy person and a patient with neuropathy, respectively. Further in-depth analyses are still needed to validated these initial findings.

# Bibliography

- [1] K. D. Kochanek, J. Xu, S. L. Murphy, A. M. Minino, and H.-C. Kung, “Deaths: final data for 2009,” Tech. Rep. 3, National Center for Health Statistics, December 2011.
- [2] World Health Organization, “Global status report on noncommunicable diseases: 2010,” tech. rep., World Health Organization, Geneva, 2011.
- [3] Heart and Stroke Foundation, “<http://www.heartandstroke.com>.”
- [4] G. Tan, T. K. Dao, L. Farmer, R. J. Sutherland, and R. Gevirtz, “Heart rate variability (HRV) and posttraumatic stress disorder (PTSD): A pilot study,” *Applied Psychophysiology and Biofeedback*, vol. 36, no. 1, pp. 27–35, 2011.
- [5] D. J. Plews, P. B. Laursen, J. Stanley, A. E. Kilding, and M. Buchheit, “Training adaptation and heart rate variability in elite endurance athletes: Opening the door to effective monitoring,” *Sports Medicine*, vol. 43, no. 9, pp. 773–781, 2013.
- [6] Research and Markets, “Cardiac Monitoring & Cardiac Rhythm Management Market ECG, Implantable Loop Recorder, Manual Event Monitor, Cardiac Output Monitoring, Defibrillator, Implantable Cardioverter Defibrillator, Dual Chamber Pacemaker, CRT-D, CRT-P - Global Forecast to 2020,” tech. rep., Research and Markets, 2015.
- [7] E. G. Wilmot, C. L. Edwardson, F. A. Achana, M. J. Davies, T. Gorely, L. J. Gray, K. Khunti, T. Yates, and S. J. Biddle, “Sedentary time in adults and the association with diabetes, cardiovascular disease and death: systematic review and meta-analysis,” *Diabetologia*, vol. 55, pp. 2895–2905, 2012.
- [8] A. S. M. Mosa, I. Yoo, and L. Sheets, “A systematic review of healthcare applications for smartphones,” *BMC medical informatics and decision making*, vol. 12, no. 1, p. 1, 2012.
- [9] G. D. Clifford and D. Clifton, “Wireless technology in disease management and medicine,” *Annual review of medicine*, vol. 63, pp. 479–492, 2012.
- [10] R. Fensli, T. Gundersen, T. Snaprud, and O. Hejlesen, “Clinical evaluation of a wireless ECG sensor system for arrhythmia diagnostic purposes,” *Medical Eng. & Physics*, vol. 35, no. 6, pp. 697–703, 2013.
- [11] H. J. Wellens and A. P. Gorgels, “How important is the electrocardiogram in protecting and guiding the athlete?,” *Circulation*, vol. 124, no. 6, pp. 669–671, 2011.

- [12] M. Swan, “Sensor mania! The Internet of Things, wearable computing, objective metrics, and the Quantified Self 2.0,” *Journal of Sensor and Actuator Networks*, vol. 1, no. 3, pp. 217–253, 2012.
- [13] F. Massé, M. V. Bussel, A. Serteyn, J. Arends, and J. Penders, “Miniaturized wireless ECG monitor for real-time detection of epileptic seizures,” *ACM Transactions on Embedded Computing Systems (TECS)*, vol. 12, no. 4, p. 102, 2013.
- [14] The statistics portal, “<https://www.statista.com/>.”
- [15] G. D. Clifford *et al.*, “ECG statistics, noise, artifacts, and missing data,” *Advanced Methods and Tools for ECG Data Analysis*, pp. 55–99, 2006.
- [16] J. E. Hall, *Guyton and Hall textbook of medical physiology*. Elsevier Health Sciences, 2015.
- [17] T. H. Falk, W.-Y. Chan, E. Sejdic, and T. Chau, “Spectro-temporal analysis of auscultatory sounds,” *In-Tech Publishing New Developments in Biomedical Engineering*, pp. 93–104, 2010.
- [18] T. H. Falk, S. Stadler, W. B. Kleijn, and W.-Y. Chan, “Noise suppression based on extending a speech-dominated modulation band.,” in *Proc. INTERSPEECH*, pp. 970–973, 2007.
- [19] L. Atlas, P. Clark, and S. Schimmel, “Modulation toolbox version 2.1 for matlab,” tech. rep., University of Washington, <http://isdl.ee.washington.edu/projects/modulationtoolbox/>, Sept. 2010.
- [20] G. Moody, W. Muldrow, and R. Mark, “A noise stress test for arrhythmia detectors,” *Computers in Cardiology*, vol. 11, pp. 381–384, 1984.
- [21] A. Goldberger *et al.*, “Physiobank, Physiokit, and Physionet components of a new research resource for complex physiologic signals,” *Circulation*, vol. 101, no. 23, pp. e215–e220, 2000.
- [22] T. Takalokastari, E. Alasaarela, M. Kinnunen, and T. Jamsa, “Quality of wireless electrocardiogram signal during physical exercise in different age groups,” *IEEE Journal of Biomedical and Health Informatics*, vol. 18, pp. 1058 – 1064, May 2014.
- [23] I. Silva, G. B. Moody, and L. Celi, “Improving the quality of ECGs collected using mobile phones: The Physionet/Computing in Cardiology Challenge 2011,” in *2011 Computing in Cardiology*, pp. 273–276, IEEE, 2011.
- [24] G. B. Moody and R. G. Mark, “The impact of the MIT-BIH arrhythmia database,” *IEEE Engineering in Medicine and Biology Magazine*, vol. 20, no. 3, pp. 45–50, 2001.
- [25] J. Behar, J. Oster, Q. Li, and G. D. Clifford, “ECG signal quality during arrhythmia and its application to false alarm reduction,” *IEEE Transactions on Biomedical Engineering*, vol. 60, no. 6, pp. 1660–1666, 2013.
- [26] T. He, G. Clifford, and L. Tarassenko, “Application of independent component analysis in removing artefacts from the electrocardiogram,” *Neural Computing & Applications*, vol. 15, no. 2, pp. 105–116, 2006.
- [27] B. Taji, S. Shirmohammadi, V. Groza, and I. Batkin, “Impact of skin–electrode interface on electrocardiogram measurements using conductive textile electrodes,” *IEEE Transactions on Instrumentation and Measurement*, vol. 63, no. 6, pp. 1412–1422, 2014.

- [28] Q. Li, R. G. Mark, and G. D. Clifford, "Robust heart rate estimation from multiple asynchronous noisy sources using signal quality indices and a Kalman filter," *Physiological measurement*, vol. 29, no. 1, pp. 15–32, 2008.
- [29] L. R. Rabiner and O. Herrmann, "The predictability of certain optimum finite-impulse-response digital filters," *IEEE Transactions on Circuit Theory*, vol. 20, no. 4, pp. 401–408, 1973.
- [30] J. T. Ramshur, "Design, evaluation, and application of heart rate variability analysis software (HRVAS)," Master's thesis, The University of Memphis, 2010.
- [31] G. Moody, B. Moody, and I. Silva, "Robust detection of heart beats in multimodal data: The physionet/computing in cardiology challenge 2014," in *Computing in Cardiology Conference (CinC), 2014*, pp. 549–552, IEEE, 2014.
- [32] N. E. Huang, Z. Shen, S. R. Long, M. C. Wu, H. H. Shih, Q. Zheng, N.-C. Yen, C. C. Tung, and H. H. Liu, "The empirical mode decomposition and the hilbert spectrum for nonlinear and non-stationary time series analysis," in *Proceedings of the Royal Society of London A: Mathematical, Physical and Engineering Sciences*, vol. 454, pp. 903–995, The Royal Society, 1998.
- [33] P. Karthikeyan, M. Murugappan, and S. Yaacob, "ECG signal denoising using wavelet thresholding technique in human stress assessment," *International Journal on Electrical Engineering and Informatics*, vol. 4, no. 2, pp. 306–319, 2012.
- [34] S. Pal and M. Mitra, "Detection of ECG characteristic points using multiresolution wavelet analysis based selective coefficient method," *Measurement*, vol. 43, no. 2, pp. 255–261, 2010.
- [35] J. Mietus, C. Peng, I. Henry, R. Goldsmith, and A. Goldberger, "The pNNx files: re-examining a widely used heart rate variability measure," *Heart*, vol. 88, no. 4, pp. 378–380, 2002.
- [36] J. Pan and W. J. Tompkins, "A real-time QRS detection algorithm," *IEEE transactions on biomedical engineering*, no. 3, pp. 230–236, 1985.
- [37] D. J. Plews, P. B. Laursen, A. E. Kilding, and M. Buchheit, "Heart rate variability in elite triathletes, is variation in variability the key to effective training? a case comparison," *European journal of applied physiology*, vol. 112, no. 11, pp. 3729–3741, 2012.
- [38] S. Laborde, A. Brüll, J. Weber, and L. S. Anders, "Trait emotional intelligence in sports: A protective role against stress through heart rate variability?," *Personality and Individual Differences*, vol. 51, no. 1, pp. 23–27, 2011.
- [39] X. Jing, P. Wu, F. Liu, B. Wu, and D. Miao, "Guided imagery, anxiety, heart rate, and heart rate variability during centrifuge training," *Aviation, space, and environmental medicine*, vol. 82, no. 2, pp. 92–96, 2011.
- [40] J. Tank, R. M. Baevsky, I. I. Funtova, A. Diedrich, I. N. Slepchenkova, and J. Jordan, "Orthostatic heart rate responses after prolonged space flights," *Clinical Autonomic Research*, vol. 21, no. 2, pp. 121–124, 2011.
- [41] M. Paul and K. Garg, "The effect of heart rate variability biofeedback on performance psychology of basketball players," *Applied Psychophysiology and Biofeedback*, vol. 37, no. 2, pp. 131–144, 2012.

- [42] G. Moody and R. Mark, "The impact of the MIT-BIH arrhythmia database," *IEEE Engineering in Medicine and Biology Magazine*, vol. 20, no. 3, pp. 45–50, 2001.
- [43] P. Kamen and A. Tonkin, "Application of the Poincaré plot to heart rate variability: a new measure of functional status in heart failure," *Australian and New Zealand journal of medicine*, vol. 25, no. 1, pp. 18–26, 1995.
- [44] P. Patil and M. Chavan, "A wavelet based method for denoising of biomedical signal," in *Pattern Recognition, Informatics and Medical Engineering (PRIME), 2012 International Conference on*, pp. 278–283, IEEE, 2012.
- [45] N. Lang, M. Brischwein, E. Ha, D. Tautinger, S. Feilner, A. Heinrich, H. Leutheuser, S. Gradl, C. Weigand, B. Eskofier, *et al.*, "Filter and processing method to improve R-peak detection for ECG data with motion artefacts from wearable systems," in *2015 Computing in Cardiology Conference (CinC)*, pp. 917–920, IEEE, 2015.
- [46] G. Georgieva-Tsaneva and K. Tcheshmedjiev, "Denoising of electrocardiogram data with methods of wavelet transform," in *International Conference on Computer Systems and Technologies*, pp. 9–16, 2013.
- [47] D. Giavarina, "Understanding bland altman analysis," *Biochemia medica*, vol. 25, no. 2, pp. 141–151, 2015.
- [48] J. Bland and D. Altman, "Statistical methods for assessing agreement between two methods of clinical measurement," *The lancet*, vol. 327, no. 8476, pp. 307–310, 1986.
- [49] P. Xanthopoulos, P. M. Pardalos, and T. B. Trafalis, "Linear discriminant analysis," in *Robust Data Mining*, pp. 27–33, Springer, 2013.
- [50] L. Wang, *Support vector machines: theory and applications*, vol. 177. Springer Science & Business Media, 2005.
- [51] S. Guillén, M. T. Arredondo, and E. Castellano, "A survey of commercial wearable systems for sport application," in *Wearable Monitoring Systems*, pp. 165–178, Springer, 2011.
- [52] M. Ammari, N. Gomes, W. Grosky, M. Jacques, B. Maxin, and D. Yoon, in *Wireless Sensor Networks: Current status and Future Trends*, ch. 1: Review of Applications of Wireless Sensor Networks, pp. 3–31. CRC Press, 2013.
- [53] L. Pecchia, P. Melillo, and M. Bracale, "Remote health monitoring of heart failure with data mining via CART method on HRV features," *IEEE Transactions on Biomedical Engineering*, vol. 58, no. 3, pp. 800–804, 2011.
- [54] M. Li, V. Rozgica, G. Thatte, S. Lee, A. Emken, M. Annavaram, U. Mitra, D. Spruijt-Metz, and S. Narayanan, "Multimodal physical activity recognition by fusing temporal and cepstral information," *IEEE Transactions on Neural Systems and Rehabilitation Engineering*, vol. 18, no. 4, pp. 369–380, 2010.
- [55] K. Yokoyama, J. Ushida, Y. Sugiura, M. Mizuno, Y. Mizuno, and K. Takata, "Heart rate indication using musical data," *IEEE Transactions on Biomedical Engineering*, vol. 49, pp. 729–733, July 2002.

- [56] M. M. Baig, H. Gholamhosseini, and M. J. Connolly, "A comprehensive survey of wearable and wireless ECG monitoring systems for older adults," *Medical & biological engineering & computing*, vol. 51, no. 5, pp. 485–495, 2013.
- [57] K. A. Sidek, I. Khalil, and H. F. Jelinek, "ECG biometric with abnormal cardiac conditions in remote monitoring system," *IEEE Transactions on Systems, Man, and Cybernetics: Systems*, vol. 44, no. 11, pp. 1498–1509, 2014.
- [58] L. Sornanathan and I. Khalil, "Fitness monitoring system based on heart rate and SpO<sub>2</sub> level," in *Proceedings of the 10th IEEE International Conference on Information Technology and Applications in Biomedicine*, pp. 1–5, IEEE, 2010.
- [59] G. D. Clifford and G. B. Moody, "Signal quality in cardiorespiratory monitoring," *Physiological Measurement*, vol. 33, no. 9, 2012.
- [60] S. Redmond, Y. Xie, D. Chang, J. Basilakis, and N. Lovell, "Electrocardiogram signal quality measures for unsupervised telehealth environments," *Physiological Measurement*, vol. 33, no. 9, pp. 1517–1533, 2012.
- [61] S. Nizami, J. R. Green, and C. McGregor, "Implementation of artifact detection in critical care: A methodological review," *IEEE Reviews in Biomedical Engineering*, vol. 6, pp. 127–142, 2013.
- [62] L. Johannesen and L. Galeotti, "Automatic ECG quality scoring methodology: mimicking human annotators," *Physiological measurement*, vol. 33, no. 9, pp. 1479–1489, 2012.
- [63] P. Melillo, M. Bracale, L. Pecchia, *et al.*, "Nonlinear heart rate variability features for real-life stress detection. case study: students under stress due to university examination," *Biomed Eng Online*, vol. 10, no. 1, p. 96, 2011.
- [64] P. K. Stein and Y. Pu, "Heart rate variability, sleep and sleep disorders," *Sleep medicine reviews*, vol. 16, no. 1, pp. 47–66, 2012.
- [65] C. Varon, *Mining the ECG: Algorithms and Applications*. PhD thesis, ARENBERG DOCTORAL SCHOOL, Faculty of Engineering Science, 2015.
- [66] J. Kuzilek, *Independent Component Analysis: Applications in ECG signal processing*. PhD thesis, Czech Technical University in Prague, 2013.
- [67] P. E. McSharry, G. D. Clifford, L. Tarassenko, and L. A. Smith, "A dynamical model for generating synthetic electrocardiogram signals," *IEEE Transactions on Biomedical Engineering*, vol. 50, no. 3, pp. 289–294, 2003.
- [68] W. T. Vetterling, S. A. Teukolsky, W. H. Press, and B. P. Flannery, *Numerical recipes example book (C)*. JSTOR, 1992.
- [69] K. T. Sweeney, T. E. Ward, and S. F. McLoone, "Artifact removal in physiological signals—practices and possibilities," *IEEE Trans Information Technology in Biomedicine*, vol. 16, no. 3, pp. 488–500, 2012.
- [70] B. Appelhans and L. Luecken, "Heart rate variability as an index of regulated emotional responding," *Review of general psychology*, vol. 10, pp. 229–240, 2006.

- [71] S. Akselrod, D. Gordon, F. Hubel, D. Shannon, A. Barger, and R. Cohen, "Power spectrum analysis of heart rate variability: a quantitative probe of beat-to-beat cardiovascular control," *Science*, vol. 2, pp. 213–220, 1981.
- [72] A. Malliani, M. Paganiand, F. Lombardi, and S. Cerutti, "Cardiovascular neuralregulation explored in the frequency domain," *Circulation*, vol. 84, p. 482?92, 1991.
- [73] A. Canim and L. Fei, "Clinical significance of heart rate variability. in moss aj and stem s and editors. noninvasive electrocardiology. clinical aspects of hotter monitoring," p. 225?48, London: WB Saunders Co Ltd, 1996.
- [74] A. Malliani, "The pattern of sympathovagal balance explored in the frequency domain," *News Physiol Sci*, vol. 14, p. 111?7, 1999.
- [75] S. Priori, E. Aliot, C. Blømstrom-Lundqvist, L. Bossaert, G. Breithardt, P. Brugada, J. Camm, R. Cappato, S. Cobbe, C. Di Mario, *et al.*, "Task force on sudden cardiac death, european society of cardiology," *Europace*, vol. 4, no. 1, pp. 3–18, 2002.
- [76] B. Ram, C. Germaine, W. Andi, S. Othild, K. George, O. Kuniaki, W. Yoshihiko, Y. Shoki, M. Hideki, I. Yuhei, M. Gen, P. Daniel, F. Lu, Z. Ziyang, S. Reema, G. Anna, and H. Franz, "Circadian heart rate and blood pressure variability considered for research and patient care," *International Journal of Cardiology*, vol. 87, no. 1, pp. 9 – 28, 2003.
- [77] A. Bilan, A. Witczak, R. Palusiński, W. Myśliński, and J. Hanzlik, "Circadian rhythm of spectral indices of heart rate variability in healthy subjects," *Journal of Electrocardiology*, vol. 38, no. 3, pp. 239 – 243, 2005.
- [78] B. Aysin, J. Colombo, and E. Aysin, "Comparison of HRV analysis methods during Orthostatic Challenge: HRV with respiration or without?," in *Engineering in Medicine and Biology Society, 2007. EMBS 2007. 29th Annual International Conference of the IEEE*, pp. 5047–5050, IEEE, 2007.
- [79] I. Gritti, S. Defendi, C. Mauri, G. Banfi, P. Duca, G. Roi, *et al.*, "Heart rate variability, standard of measurement, physiological interpretation and clinical use in mountain marathon runners during sleep and after acclimatization at 3480 m," *Journal of Behavioral and Brain Science*, vol. 3, no. 01, p. 26, 2013.
- [80] T. N. A. S. o. P. E. Task Force of The European Society of Cardiology and, "Heart rate variability: standards of measurement, physiological interpretation and clinical use.," *Circulation*, vol. 93, no. 5, pp. 1043–65, 1996.
- [81] K. Park and H. YiS, "Accessing Physiological Complexity of HRV by Using Threshold-Dependent Symbolic Entropy," *Journal of the Korean Physical Society*, vol. 44, no. 3, p. pp. 569?576, March 2004.
- [82] C. Karmakar, A. Khandoker, H. Jelinek, and M. Palaniswami, "Risk stratification of cardiac autonomic neuropathy based on multi-lag tone-entropy," *Med. Biol. Eng. Comput.*, vol. 51, p. 537?546, 2013.
- [83] K. Nasim, A. Jahan, and S. Syed, "Heart rate variability : a review," *J. Basic Appl. Sci.*, pp. 71–77, 2011.

- [84] C. Liu, K. Li, L. Zhao, F. Liu, D. Zheng, C. Liu, and S. Liu, "Analysis of heart rate variability using fuzzy measure entropy," *Computers in biology and Medicine*, vol. 43, no. 2, pp. 100–108, 2013.
- [85] J. Tapanainen, P. Thomsen, L. Køber, C. Torp-Pedersen, T. Mäkikallio, A. Still, K. Lindgren, and H. Huikuri, "Fractal analysis of heart rate variability and mortality after an acute myocardial infarction," *The American Journal of Cardiology*, vol. 90, no. 4, pp. 347 – 352, 2002.
- [86] T. Mäkikallio, H. Huikuri, U. Hintze, J. Videbæk, R. Mitrani, A. Castellanos, R. Myerburg, and M. Møller, "Fractal analysis and time- and frequency-domain measures of heart rate variability as predictors of mortality in patients with heart failure," *The American Journal of Cardiology*, vol. 87, no. 2, pp. 178 – 182, 2001.
- [87] R. Acharya, B. Subbanna, N. Kannathal, A. Rao, and C. Lim, "Analysis of cardiac health using fractal dimension and wavelet transformation," *ITBM-RBM*, vol. 26, no. 2, pp. 133 – 139, 2005.
- [88] G. Clifford, *Signal Processing Methods for Heart Rate Variability*. PhD thesis, University of Oxford, 2002.
- [89] K. Shafqat, S. Pal, and P. Kyriacou, "Evaluation of two detrending techniques for application in heart rate variability," in *2007 29th Annual International Conference of the IEEE Engineering in Medicine and Biology Society*, pp. 267–270, IEEE, 2007.
- [90] K. Chang, "Arrhythmia ECG noise reduction by ensemble empirical mode decomposition," *Sensors*, vol. 10, no. 6, pp. 6063–6080, 2010.
- [91] J. Lee, D. D. McManus, S. Merchant, and K. H. Chon, "Automatic motion and noise artifact detection in holter ECG data using empirical mode decomposition and statistical approaches," *IEEE Transactions on Biomedical Engineering*, vol. 59, no. 6, pp. 1499–1506, 2012.
- [92] M. A. Kabir and C. Shahnaz, "Denoising of ECG signals based on noise reduction algorithms in EMD and wavelet domains," *Biomedical Signal Processing and Control*, vol. 7, no. 5, pp. 481–489, 2012.
- [93] D. Donoho and J. Johnstone, "Ideal spatial adaptation by wavelet shrinkage," *Biometrika*, vol. 81, no. 3, pp. 425–455, 1994.
- [94] L. Smital, M. Vitek, J. Kozumplík, and I. Provazník, "Adaptive wavelet wiener filtering of ECG signals," *IEEE Transactions on Biomedical Engineering*, vol. 60, no. 2, pp. 437–445, 2013.
- [95] S. Pongponsri and X.-H. Yu, "An adaptive filtering approach for electrocardiogram (ECG) signal noise reduction using neural networks," *Neurocomputing*, vol. 117, pp. 206–213, 2013.
- [96] E.-S. A. El-Dahshan, "Genetic algorithm and wavelet hybrid scheme for ECG signal denoising," *Telecommunication Systems*, vol. 46, no. 3, pp. 209–215, 2011.
- [97] M. Üstündağ, M. Gökbulut, A. Şengür, and F. Ata, "Denoising of weak ECG signals by using wavelet analysis and fuzzy thresholding," *Network Modeling Analysis in Health Informatics and Bioinformatics*, vol. 1, no. 4, pp. 135–140, 2012.

- [98] Y. Tu, X. Fu, D. Li, C. Huang, Y. Tang, S. Ye, and H. Chen, "A novel method for automatic identification of motion artifact beats in ECG recordings," *Annals of biomedical engineering*, vol. 40, no. 9, pp. 1917–1928, 2012.
- [99] S. K. Salih, S. Aljunid, S. M. Aljunid, and O. Maskon, "Adaptive filtering approach for denoising electrocardiogram signal using moving average filter," *Journal of Medical Imaging and Health Informatics*, vol. 5, no. 5, pp. 1065–1069, 2015.
- [100] R. Sameni, M. B. Shamsollahi, C. Jutten, and G. D. Clifford, "A nonlinear Bayesian filtering framework for ECG denoising," *IEEE Transactions on Biomedical Engineering*, vol. 54, no. 12, pp. 2172–2185, 2007.
- [101] B. N. Singh and A. K. Tiwari, "Optimal selection of wavelet basis function applied to ECG signal denoising," *Digital Signal Processing*, vol. 16, no. 3, pp. 275–287, 2006.
- [102] P. Agante and J. M. De Sá, "ECG noise filtering using wavelets with soft-thresholding methods," in *Computers in Cardiology, 1999*, pp. 535–538, IEEE, 1999.
- [103] J. Behar, J. Oster, Q. Li, and G. Clifford, "A single channel ECG quality metric," in *Computing in Cardiology*, pp. 381–384, IEEE, 2012.
- [104] B. Aldecoa Sanchez del Rio, T. Lopetegi, and I. Romero, "Assessment of different methods to estimate electrocardiogram signal quality," in *Computing in Cardiology*, pp. 609–612, IEEE, 2011.
- [105] L. Di Marco, W. Duan, M. Bojarnejad, D. Zheng, S. King, A. Murray, and P. Langley, "Evaluation of an algorithm based on single-condition decision rules for binary classification of 12-lead ambulatory ECG recording quality," *Physiological Measurement*, vol. 33, no. 9, p. 1435, 2012.
- [106] I. Silva, J. Lee, and R. G. Mark, "Signal quality estimation with multichannel adaptive filtering in intensive care settings," *IEEE Transactions Biomedical Eng*, vol. 59, no. 9, pp. 2476–2485, 2012.
- [107] D. Hayn, B. Jammerbund, and G. Schreier, "QRS detection based ECG quality assessment," *Physiological measurement*, vol. 33, no. 9, p. 1449, 2012.
- [108] A. Fedotchev *et al.*, "Concerning the amplitude modulation of the human eeg," *Human Physiology*, vol. 26, no. 4, pp. 393–399, 2000.
- [109] J.-w. Hung, W.-h. Tu, and C.-c. Lai, "Improved modulation spectrum enhancement methods for robust speech recognition," *Signal Processing*, vol. 92, no. 11, pp. 2791–2814, 2012.
- [110] M. Viitasalo, R. Kala, and A. Eisalo, "Ambulatory electrocardiographic recording in endurance athletes.," *British heart journal*, vol. 47, no. 3, pp. 213–220, 1982.
- [111] A. Y. Mal'tsev, A. Mel'nikov, A. Vikulov, and K. Gromova, "Central hemodynamic and heart rate variability parameters in athletes during different training programs," *Human physiology*, vol. 36, no. 1, pp. 96–101, 2010.
- [112] W. Kindermann, G. Simon, and J. Keul, "The significance of the aerobic-anaerobic transition for the determination of work load intensities during endurance training," *European Journal of Applied Physiology and Occupational Physiology*, vol. 42, no. 1, pp. 25–34, 1979.

- [113] S. Seiler, O. Haugen, and E. Kuffel, "Autonomic recovery after exercise in trained athletes: intensity and duration effects," *Medicine and science in sports and exercise*, vol. 39, no. 8, p. 1366, 2007.
- [114] M. Malik, R. Xia, J. Poloniecki, O. Odemuyiwa, T. Farrell, A. Staunton, and A. Camm, "Influence of the noise and artefact in automatically analysed long term electrocardiograms on different methods for time-domain measurement of heart rate variability," in *Computers in Cardiology 1991, Proceedings.*, pp. 269–272, IEEE, 1991.
- [115] B. Oke, B. Dietmar, M. Lutz, S. Jens, and H. Robert, "Impact of artefacts during routine ECG recording for analysis of heart rate variability: 3AP1-6," *European Journal of Anaesthesiology (EJA)*, vol. 25, p. 26, 2008.
- [116] M. Singh, B. Singh, and A. Rajput, "Impact of Missing RR-interval on Non-Linear HRV Parameters," *International Journal of Computer Applications*, vol. 124, no. 11, 2015.
- [117] C. Tsimenidis and A. Murray, "False alarms during patient monitoring in clinical intensive care units are highly related to poor quality of the monitored electrocardiogram signals," *Physiological Measurement*, vol. 37, no. 8, p. 1383, 2016.
- [118] P. Karthikeyan, M. Murugappan, and S. Yaacob, "ECG signal denoising using wavelet thresholding techniques in human stress assessment," *International Journal on Electrical Engineering and Informatics*, vol. 4, no. 2, p. 306, 2012.